九州大学学術情報リポジトリ
Kyushu University Institutional Repository

Theoretical and Experimental Approach to Hydrogenolysis and Hydrogenation of Lignin and Catalyst Design

亓, 士超

https://doi.org/10.15017/1866326

出版情報：九州大学, 2017, 博士（工学）, 課程博士
バージョン：
権利関係：

KYUSHU UNIVERSITY

Theoretical and Experimental Approach to Hydrogenolysis and Hydrogenation of Lignin and Catalyst Design

by

Shi-Chao Qi

Department of Applied Science for Electronics and Materials

Interdisciplinary Graduate School of Engineering Sciences

Kyushu University

2017

CONTENT

Chapter 1
General introduction

1.1. Background

Lignin accounts for almost 30% of organic carbon within the biosphere, and has an intriguing biosynthesis. In view of the predicted depletion of fossil resources and the growing threat of global warming, the utilization of lignin has become a center of interest for worldwide scientists and industries, as the lignin, of which more than half of that carbon is aromatic, provides alternative and attractive new sustainable platforms of fuels, chemicals, and materials [1-3]. However, it is still difficult to translate the longstanding interest in lignin valorization into commercial processes because of lacking of effective approaches to upgrading it. The most frequently discussed approach to the lignin depolymerization in recent years is hydroprocessing, including hydrogenolysis, hydrogenation, and hydrodeoxygenation. The best catalytic species for all the three reactions are transition metals, in particular Ni that have been the most popular metallic catalyst used in integrated hydrogen-processing of lignin [4-9]. Preparation of highly active catalysts is thus critical to lignin utilization. Density functional theory (DFT) has become a popular computation tool in most chemistry fields [10-12]. For deep insight into the mechanisms of catalyst preparation and lignin hydroprocessing, DFT is widely applied in this thesis.

1.2. Depolymerization of lignin

There are generally three main approaches for lignin depolymerization, i.e., pyrolysis, oxidation, and hydroprocessing (hydrogenolysis, deoxygenation). In some cases, enzymatic depolymerization methods have also been described. However, depolymerisation processes are often not too well understood in terms of mechanism.

1.2.1. Pyrolysis of lignin

Pyrolysis is one of the primary thermochemical methods for producing bio-oil directly from lignocellulosic biomass [13]. It is the rapid heating of biomass at temperatures between 450 and 600 ℃ often in the absence of oxygen to generate a mixture of noncondensable gases, liquid oil, and solid, with or without any catalyst [14]. It represents a straightforward strategy to break down lignin into smaller fragments. However, thermal depolymerization of lignin follows a series of random and complicated reactions that produce low yields of a complex product mixture. Wet lignin from an aqueous-based biorefinery or from most pulping processes must be dried before entering a pyrolysis process decreasing the viability of this process because the evaporation of a large amount of water present in lignin feedstock requires a lot of energy. Jones and Zhu conclude that lignin pyrolysis at present is not economically attractive [15]. Fast pyrolysis oil, or bio-oil, is a potential feedstock to make liquid transportation fuels. The pyrolysis oil consists of up to 50 wt% of pyrolytic lignin, which is thought to derive from pyrolysis of the lignin structure of biomass [16]. This suggests that the hemicellulose and cellulose somehow play

a role in stabilizing the lignin pyrolysis intermediates during pyrolysis of the entire biomass species. The bio-oil is a low quality liquid fuel, that is an emulsion of several phases that has many undesired characteristics, including low pH, high viscosity, low energy density (high oxygen content), and stability problems, and it cannot be blended with conventional fuels [17,18].

1.2.2. Oxidation of lignin

Oxidative depolymerization of lignin is a valorization strategy that focuses on producing polyfunctional aromatic compounds. The oxidative cracking reaction includes the cleavage of the aryl ether bonds, carbon−carbon bonds, aromatic rings, or other linkages within the lignin. Nitrobenzene, metal oxides, molecular oxygen, and hydrogen peroxide are the most popular oxidants for lignin. The oxidation products of lignin are mainly polyfunctional monomeric compounds, ranging from aromatic aldehydes to carboxylic acids, such as vanillin, syringaldehyde, and 4-hydroxybenzaldehyde, which are alternative to fossil fuels derived chemicals. The catalytic systems that have been used for lignin oxidation can be divided into six types: organometallic catalysis, metal-free organic catalysis, acid or base catalysis, metal salts catalysis, photocatalytic oxidation, and electrocatalytic oxidative cleavage of lignin. It should be noted that, in most of the strategies for lignin oxidation, the rearrangement and oligomerization of intermediate products of lignin fragmentation are inevitable side reactions. Di Renzo and co-workers have extensively studied vanillin oligomerization as a model of side reactions in lignin fragmentation [19]. It was found that hydrothermal treatment of vanillin under oxidative conditions can produce a wide variety of by-products. The nature of the catalyst and solvent significantly affect the products formed. For most developed lignin oxidation catalytic systems, the yields of the products, as yet, are too low to make the overall process economically viable. This is, to some extent, attributable to the complex lignin structure. Therefore, design of robust catalysts that fit with the complex structure and increase the product selectivity are promising directions for the development of lignin oxidation technology.

1.2.3. Hydroprocessing of lignin

Hydroprocessing is one of the most popular and efficient strategies applied in deconstruction of lignin into components such as low depolymerized lignin, phenols, and other valuable chemicals, and upgrading of the small compounds to hydrocarbon fuels. In fact, hydroprocessing includes several reaction types, such as hydrogenolysis, hydrogenation, and hydrodeoxygenation. Ni-based catalysts used for lignin hydrogenation/hydrogenolysis can be dated back to the 1940s [20]. Since then, various Ni-based catalysts have been developed and applied generally to the hrdroprocessing lignin and its model compounds. For example, Zhao and co-workers [21] reported a novel SiO_2 supported Ni catalyst to selectively cleave aromatic C−O bonds of aryl ethers in the aqueous phase. This catalyst is not water sensitive, unlike the homogeneous catalysts. The C−O bonds of α-O-4 and β-O-4 are cleaved by hydrogenolysis, while the 4-O-5 linkage is cleaved through parallel hydrogenolysis and hydrolysis, due to the employment of aqueous solvent. In their report, however, hydrogenation of phenol proceeded over Ni catalysts along with the hydrogenolysis under the investigated conditions. It was well documented that the introduction of a

second metal to a monometallic catalyst can enhance the catalytic performance in many reactions [22]. Zhang and co-workers [23] disclosed that carbon supported Ni−W_2C catalyzes not only the direct conversion of cellulose into ethylene glycol, but also the hydrogenolysis of the lignin component in various woody biomass into monophenols with the yield of 46.5%. The catalysts of hydrodeoxygenation of lignin include mono- and bimetallic types as well. Molybdenum oxide, sulfide, nitride, and carbide were studied as catalysts for the hydrodeoxygenation of lignin and model compounds as early as in the 1980s [24]. Transition metal phosphides Ni_2P, Fe_2P, Co_2P, and WP have been applied in the hydrodeoxygenation of lignin-derived feedstock recently [25]. Mixed sulfides of Co, Ni, Mo, and W, as well as other bimetallic catalyst systems, such as PtSn [26], PtRh [27], NiRe [28], PtRe [29], and ZnPd [30], are used most frequently in lignin hydrodeoxygenation.

Due to the extremely complicated multifunctional groups of the lignin substrate, it is hard to obtain only one product from hydroprocessing lignin. Integrated hydrogen-processing that includes deconstruction of lignin and upgrading of small components to expected products is favorable. The catalyst systems which directly convert lignin to bio-oils and chemicals, or catalyze several reactions in a batch subsequently, will not only reduce the complexity of the lignin transformation and benefit the economy of the conversion process, but also increase the possibility to scale up the lignin biorefinery process.

1.3. Catalyst preparation

As above-mentioned, the catalysts play critical roles in the upgrading lignin, in particular the supported metallic catalysts for hydroprocessing lignin. The activity of a supported metallic catalyst is largely attributed to the size and the dispersion of loaded metal particles, which mainly depend on the preparation method of catalysts. The preparation of highly active catalysts is thus an attractive subject. Traditional impregnation-reduction method has been extensively investigated, while there are many other methods different with traditional process (**Table 1-1**) [31-38]. Highly dispersive supported metals, even metal nanoparticles, can be prepared through such methods.

1.4. Density functional theory

Density functional theory (DFT) was established until the introduction of the Hohenberg–Kohn (H–K) theorem [39,40]. Subsequently, the Kohn–Sham (K–S) theory made DFT calculations a reality [41]. According to the K–S theory, the energy of the electrons in an *N*-electron system is disassembled as Eq. 1.1, in which the functionals $T_s[\rho]$, $V_{ne}[\rho]$, and $E_{coul}[\rho]$ are explicitly known and represent the kinetic energy of the noninteracting reference electrons, the nucleus–electrons potential energy and the classical electron−electron repulsion energy, respectively. A key remaining term $E_{xc}[\rho]$, the exchange-correlation energy, is the very study core of DFT and generates different DFT methods.

$$E[\rho] = T_s[\rho] + V_{ne}[\rho] + E_{coul}[\rho] + E_{xc}[\rho]$$

$$= -\frac{1}{2}\sum_{i=1}^{N}\int \phi_i^*(\boldsymbol{r})\,\nabla_i^2\,\phi_i(\boldsymbol{r})d\boldsymbol{r} + \int V(\boldsymbol{r})\rho(\boldsymbol{r})d\boldsymbol{r} + \frac{1}{2}\iint \frac{\rho(\boldsymbol{r})\rho(\boldsymbol{r}')}{|\boldsymbol{r}-\boldsymbol{r}'|}d\boldsymbol{r}d\boldsymbol{r}' + E_{xc}[\rho]$$

$$\rho(\boldsymbol{r}) = \sum_{i=1}^{N}\phi_i^*(\boldsymbol{r})\phi_i(\boldsymbol{r})$$

(1.1)

To classify the $E_{xc}[\rho]$ functionals, Perdew proposed *Jacob's ladder*, which was based on the descriptions of the Hartree world without any exchange-correlation and led to extremely high chemical accuracy. The first rung of *Jacob's ladder* is local density approximation (LDA), followed by generalized gradient approximation (GGA), meta-GGA, and finally, hybrid functionals. Each rung on the ladder should contain functionals that are based on and perform better than the previous rungs. The LDA is the first stage of E_{xc} evolution [42]. Simulating the free electron gas, the mathematical form of E_x was proposed. With regard to E_c, the functionals VMN and PW92 were proposed based on LDA [43]. LDA is accurate to describe free electron gas, but unfortunately, the electron systems of molecules are not as uniform as the free state. The GGA dramatically developed LDA via introducing the electron density gradient into E_{xc}. There are many famous and popular GGA-E_x or -E_c functionals such as B88, PW86, PW91, PBE, and LYP [44-50]. Subsequently, functionals referred to as meta-GGA were derived from the variable of kinetic energy density in E_{xc}. The hybrid functionals greatly enhanced the precision of DFT through including a certain proportion of E_x^{HF} into $E_{xc}[\rho]$, such as B3LYP, which represented or even dominated the DFT calculation to some extent.

Different E_{xc} forms dictate the scope of the applications and the accuracy of different functionals. First, although hybrid functionals greatly improve the precision of the DFT calculation, GGA or meta-GGA pure functionals such as PW91 and PBE are still very appropriate for the calculation of metal systems since both E_c and E_x of metal systems are delocalized. It is interesting that once the proportion of E_x^{HF} in hybrid functional decreases, the performance of the hybrid functional on the transition metals is improved. For instance, Siegbahn showed that the general accuracy of calculations involving transition metals may be improved when the proportion of E_x^{HF} in B3LYP decreased from 20% to 15% [51]. Second, with regard to the systems involving several metal atoms, the selection of functionals largely depends on the chemical surroundings of the metal centers. It is difficult to define which is the best functional for specific system, since the functionals for the calculation of metal complexes are too flexible to delimit their range of applicability. As shown in **Table 1-2**, satisfying all calculation terms of a functional with high accuracy is impossible. Thus, the selection of functionals depends on the terms that can be calculated.

1.5. Objective of this study

Lignin has become a center of interest for worldwide scientists and industries. More than half of that carbon in lignin is aromatic, so it provides alternative and attractive new sustainable platforms of fuels, chemicals, and materials. Depolymerization is a prerequisite for efficient utilization of lignin because it has a randomly polymerized material forming a complex three-dimensional macromolecular structure. Catalytic hydroprocessing is a major approach to upgrading of lignin. Designing highly active catalyst is thus a critical subject to the efficient hydroprocessing of lignin. In this study, a highly dispersive nickel catalyst supported by ZSM-5 zeolite is designed through chemical reduction of a nickel-pyridine complex and is applied to hydrogenation of a series of lignin monomers. The mechanism of the catalyst formation and the reactivities of the lignin monomers are calculated by DFT (**Chapter 2**). The hydrogenolytic reactivities of five typical lignin linakages in the presence of hydrogen free-radicals are calculated by DFT (**Chapter 3**). The nickel catalyst is then applied to the hydrogenolysis of kraft lignin dissolved in alkaline water. A pretreatment of stretching lignin macromolecules is carried out to increase the hydrogenolytic yield of the kraft lignin largely (**Chapter 4**).

1.6. Outline of this study

In **Chapter 1**, the current situations of lignin utilization are first introduced. Various approaches to prepare heterogeneous catalysts are then summarized and compared. In order to have a deep insight into the mechanism of catalyst formation, and that of hydroprocessing of lignin, DFT is widely used in this study. The developments and performances of DFT are summarized in **Chapter 1** as well.

Chapter 2 first reports complete arene hydrogenation of phenolic compounds as lignin monomers over a non-noble metal catalyst supported by a general material. A type of nano-sized Ni catalyst was prepared in ethanol and *in-situ* supported by a ZSM-5 zeolite through general borohydride reduction of Ni^{2+} to Ni^{0}, but with application of a simple ligand, pyridine. This catalyst showed an activity so high as to completely or near completely hydrogenate the aromatic rings of phenol and its twelve derivatives as potential lignin monomers at 180 ℃. The activity was clearly higher than that of another type of conventional Ni catalyst prepared in the absence of pyridine. Analyses of the catalysts by TEM/EDS, XPS, XAFS and others demonstrated that pyridine had crucial roles for selective formation of nano-sized Ni and maintenance of its activity by appropriate interaction with the support. This chapter also shows our theoretical approach to the mechanism of the borohydride reduction. First-principles calculations on the basis of DFT revealed the reaction pathway from Ni^{2+} to Ni^{0} and the role of pyridine, which was validated by some experimental facts. The DFT calculations also explain the variety of reactivities of the lignin monomers, which are strongly influenced by their molecular electrostatic and steric natures.

In **Chapter 3**, DFT is employed to investigate the initial hydrogenolytic cleavages of recognized five different types of inter-aromatic unit linkages of lignin, with assuming the presence of hydrogen free radicals. The relative free energies of reactant complexes, reaction free energy changes, and rate constants for candidate reactions are calculated comprehensively at 298−538 K. Based on the results of calculation and a rapid equilibrium hypothesis, the major reaction channel is decided for each linkage, and its kinetics is assessed. It is concluded that the hydrogenolysis occurs at β-O-4 ether, diphenylether 4-O-5', and β-1' diphenylmethane linkages instantaneously if these are accessible to hydrogen free radicals, while β-5 phenylcoumaran and β-β' pinoresinol linkages are virtually inert to hydrogenolysis.

In **Chapter 4**, inspired by results of calculation on the basis of DFT and a semi-empirical method, the author found an easy, robust, and efficient approach to solve the problem of folded lignin macromolecules, which is a key factor for impeding their breakdown into monomers by hydrogenolysis. Oxidation and hydrogenolysis, which appear to be independent and contradictory of each other in many past studies, were combined and successively performed in this study. Hydrogen peroxide was used to damage the strong intramolecular hydrogen bonds of Kraft lignin efficiently, transforming the folded three-dimensional geometries of the lignin macromolecules into stretched ones in an alkaline aqueous medium. Following the pretreatment of stretching lignin molecules, catalytic hydrogenolysis was performed in the presence of a Ni catalyst supported by ZSM-5 zeolite, reported by the authors. Because of more chemisorption sites of the stretched lignin macromolecules onto the catalyst surface and the remission of lignin re-polymerization/self-condensation, conversion of the kraft lignin into oil reached 83 wt%-lignin, 91 wt% which was accounted for by nine types of monomers. This chapter has thus demonstrated high yield monomer production from lignin dissolved in aqueous media.

In **Chapter 5**, general conclusions of this study are summarized.

1.7. References

1 J. Zakzeski, P. C. A. Bruijnincx, A. L. Jongerius and B. M. Weckhuysen, *Chem. Rev.*, 2010, **110**, 3552−3599.

2 C. P. Xu, R. A. D. Arancon, J. Labidi and R. Luque, *Chem. Soc. Rev.*, 2014, **43**, 7485−7500.

3 C. Z. Li, X. C. Zhao, A. Q. Wang, G. W. Huber and T. Zhang, *Chem. Rev.*, 2015, **115**, 11559−11624.

4 K. Barta, G. R.Warner, E. S. Beach and P. T. Anastas, *Green Chem.*, 2014, **16**, 191−196.

5 Y. Y. Wang, L. L. Ling and H. Jiang, *Green Chem.*, 2016, **18**, 4032−4041.

6 M. Wang, L. H. Li, J. M. Lu, H. J. Li, X. C. Zhang, H. F. Liu, N. C. Luo and F. Wang, *Green Chem.*, 2017, **19**, 702−706.

7 C. F. Zhang, J. M. Lu, X. C. Zhang, K. MacArthur, M. Heggen, H. J. Li and F. Wang, *Green Chem.*, 2016, **18**, 6545−6555.

8 Z. Li, M. Garedew, C. H. Lam, J. E. Jackson, D. J. Miller and C. M. Saffron, *Green Chem.*, 2012, **14**, 2540−2549.

9 C. H. Lam, C. B. Lowe, Z. Li, K. N. Longe, J. T. Rayburn, M. A. Caldwell, C. E. Houdek, J. B. Maguire, C. M. Saffron, D. J. Miller and J. E. Jackson, *Green Chem.*, 2015, **17**, 601−609.

10 C. D. Sherrill, *J. Chem. Phys.*, 2010, **132**, 110902.

11 F. Neese, *Coord. Chem. Rev.*, 2009, **253**, 526-563.

12 H. Hu and W. T. Yang, *Annu. Rev. Phys. Chem.*, 2008, **59**, 573-601.

13 D. Mohan, C. U. Pittman and P. H. Steele, *Energy Fuels*, 2006, **20**, 848−889.

14 H. B. Goyal, D. Seal and R. C. Saxena, *Renewable Sustainable Energy Rev.*, 2008, **12**, 504−517.

15 S. Jones and Y. Zhu, in Preliminary economics for the production of pyrolysis oil from lignin in a cellulosic ethanol biorefinery, Pacific Northwest National Laboratory: Richland, 2009, pp. 1−32.

16 T. P. Vispute, H. Zhang, A. Sanna, R. Xiao and G. W. Huber, *Science*, 2010, **330**, 1222−1227.

17 A. S. Pollard, M. R. Rover and R. C. J. Brown, *Anal. Appl. Pyrolysis*, 2012, **93**, 129−138.

18 D. Meier, B. van de Beld, A. V. Bridgwater, D. C. Elliott, A. Oasmaa and F. Preto, *Renewable Sustainable Energy Rev.*, 2013, **20**, 619−641.

19 S. Constant, M. Robitzer, F. Quignard and F. Di Renzo, *Catal. Today*, 2012, **189**, 123−128.

20 J. M. Pepper and H. Hibbert, *J. Am. Chem. Soc.*, 1948, **70**, 67−71.

21 J. He, C. Zhao and J. A. Lercher, *J. Am. Chem. Soc.*, 2012, **134**, 20768−20775.

22 D. Tilly, F. Chevallier, F. Mongin and P. C. Gros, *Chem. Rev.*, 2014, **114**, 1207−1257.

23 N. Ji, T. Zhang, M. Y. Zheng, A. Q. Wang, H. Wang, X. D. Wang and J. G. G. Chen, *Angew. Chem. Int. Ed.*, 2008, **47**, 8510−8513.

24 H. L. Chum and D. K. Johnson, Liquid fuels from lignins: Annual Report; National Renewable Energy Laboratory (NREL): Golden, CO, 1986.

25 L. N. Ding, A. Q. Wang, M. Y. Zheng and T. Zhang, *ChemSusChem*, 2010, **3**, 818−821.

26 M. A. Gonzalez-Borja and D. E. Resasco, *Energy Fuels*, 2011, **25**, 4155−4162.

27 Y. C. Lin, C. L. Li, H. P. Wan, H. T. Lee and C. F. Liu, *Energy Fuels*, 2011, **25**, 890−896.

28 B. Feng, H. Kobayashi, H. Ohta, A. Fukuoka, *J. Mol. Catal. A: Chem.*, 2014, **388**, 41−46.

29 H. Ohta, B. Feng, H. Kobayashi, K. Hara and A. Fukuoka, *Catal. Today*, 2014, **234**, 139−144.

30 T. H. Parsell, B. C. Owen, I. Klein, T. M. Jarrell, C. L. Marcum, L. J. Haupert, L. M. Amundson, H. I. Kenttamaa, F. Ribeiro, J. T. Miller and M. M. Abu-Omar, *Chem. Sci.*, 2013, **4**, 806−813.

31 A. G. Boudjahem, W. Bouderbala and M. Bettahar, *Fuel Process. Technol.*, 2011, **92**, 500-506.

32 S. B. Ren, P. Zhang, H. F. Shui, Z. P. Lei, Z. C. Wang and S. G. Kang, *Catal. Commun*., 2010, **12**, 132-136.

33 P. G. Savva, K. Goundani, J. Vakros, and K. Bourikas, *Appl. Catal. B: Environ.*, 2008, **79**, 199-207.

34 M. A. Ermakova and D. Y. Ermakov, *Appl. Catal. A: Gen.*, 2003, **245**, 277-288.

35 Z. W. Guo, W. T. Huo and M. J. Jia, *J. Mol. Catal. A: Chem.*, 2010, **326**, 82-87.

36 R. Molina and G. Poncelet, *J. Catal.*, 2001, **199**, 162-170.

37 E. Redel, J. Krämer, R. Thomann and C. Janiak, *J. Organomet. Chem.*, 2009, **694**, 1069-1075.

38 S. Rojas, P. Terreros, M. A. Peña and M. Ojeda, *J. Mol. Catal. A: Chem.*, 2003, **206**, 299-311.

39 X. Y. Pan and V. Sahni, *J. Chem. Phys.*, 2015, **143**, 174105.

40 A. Laestadius and M. Benedicks, *Int. J. Quantum Chem.*, 2014, **114**, 782-795.

41 W. Kohn and L. J. Sham, *Phys. Rev.*, 1965, **140**, 1133-1138.

42 J. Nemeth and D. Vautherin, *Phys. Lett. B*, 1970, **32**, 561-564.

43 D. M. Ceperley, *Phys. Rev. Lett.*, 1980, **45**, 566-569.

44 A. D. Becke, *Phys. Rev. A*, 1988, **38**, 3098-3100.

45 J. P. Perdew and Y. Wang, *Phys. Rev. B*, 1986, **33**, 8800-8802.

46 J. P. Perdew, J. A. Chevary and S. H. Vosko, *Phys. Rev. B*, 1992, **46**, 6671-6687.

47 J. P. Perdew, K. Burke and M. Ernzerhof, *Phys. Rev. Lett.*, 1996, **77,** 3865-3868.

48 J. P. Perdew, *Phys. Rev. B*, 1986, **33**, 8822-8824.

49 C. Lee, W. Yang and R. G. Parr, *Phys. Rev. B*, 1988, **37**, 785-789.

50 B. Miehlich, A. Savin, H. Stoll and H. Preuss, *Chem. Phys. Lett.*, 1989, **157**, 200-206.

51 P. E. M. Siegbahn, *J. Biol. Inorg. Chem.*, 2006, **11**, 695-701.

Table 1-1 Preparation methods of supported metallic catalysts.

Catalyst	Method	Material	Concise process	Ref.
Ni-Cu/SiO_2	AH reduction	Silica, NA, $Cu(NO_3)_2$ and hydrazine	Impregnation was carried out using NA and $Cu(NO_3)_2$ as precursors. Silica was added to the solution to obtain suspension followed by the addition of excess AH at pH = 10.	31
Ni/SBA-15	Pretreatment with NH_3/H_2O vapor	$Ni(NO_3)_2$, SBA-15 and NH_3/H_2O	SBA-15 was impregnated with $Ni(NO_3)_2$ aqueous solution then dried at 100 ^oC. The dried sample was pretreated by NH_3/H_2O vapor followed by dessication, calcination and reduction in H_2 flow.	32
Ni/Al_2O_3	Sol-gel	ATB, AA and $Ni(NO_3)_2$	ATB was dissolved in isopropanol. AA was added as a chelating agent. $Ni(NO_3)_2$ aqueous solution was added to obtain gel followed by dessication, calcination and reduction in H_2 flow.	33
Ni/SiO_2	Heterophase sol-gel	$Ni(NO_3)_2$, ES-32, ethanol and NH_3 aqueous solution	Precipitation of $Ni(NO_3)_2$ with NH_3 aqueous solution afforded $Ni(OH)_2$, which was calcinated to get NiO. Ni/SiO_2 with desired Ni to SiO_2 ratio was obtained by impregnating NiO with a proper concentration of ES-32 in ethanol followed by dessication and reduction in H_2 flow.	34
Ni-Al	Co-precipitation	$Ni(NO_3)_2$, $Al(NO_3)_3$ and NH_3 aqueous solution	$Ni(NO_3)_2$ was mixed with $Al(NO_3)_3$ and then NH_3 aqueous solution was added until pH = 8. The mixture was aged, dried, calcined and in situ reduced under H_2 atmosphere	35
Ni/Al_2O_3	Using NAA as the precursor	NA, benzene and Al_2O_3	NAA was dissolved in benzene and added into Al_2O_3 followed by filtration, washing with benzene, dessication, calcination and reduction in H_2 flow at 400 ^oC.	36
Nano-Co, Rh and Ir	Using MC as the precursor	MC and an ionic liquid	MC was dissolved in the dried and deoxygenated ionic liquid under argon atmosphere, the solution was heated up to 230 ^oC to decompose MC into nanoparticles.	37
Pd/SiO_2	Using $PdCl_2(PhCN)_2$ as the precursor	$PdCl_2(PhCN)_2$, CH_2Cl_2 and SiO_2	A solution of $PdCl_2(PhCN)_2$ in CH_2Cl_2 was mixed with modified SiO_2 in a degassed reactor at 48 ^oC. Then the mixture was cooled, filtered, washed with CH_2Cl_2 and dried in a vacuum.	38

AH: aqueous hydrazine; NA: nickel acetate; ATB: aluminum tri-*sec*-butoxide; AA: acetylacetone; ES-32: ethyl silicate-32; NAA: nickel acetylacetonate; MC: metal carbonyl

Table 1-2 Suggested focus items of some functionals.

Focus item	Functional
Thermodynamics of main group atoms, organometallics	B3LYP, B3PW91 and M06
Reaction dynamics of main group atoms	B3LYP, B3PW91 M06-2X, and M06
Reaction dynamics of inorganic/organometallics	TPSS, M06-L, and M06
Binuclear metals	PBE, BP86, TPSS, M06-L, and M06
Nuclear magnetic resonance	M06-L, VSXC, OPBE, and PBE1PBE
Electronic circular dichroism spectroscopy	B3LYP, and PBE1PBE
Two-photon adsorption	CAM-B3LYP
Excitation of valence shell	PBE1PBE, and M06-2X
Charge transfer, Rydberg excitation, adiabatic excitation	wB97XD, CAM-B3LYP, and M06-2X
Polarizability, hyperpolarizability	PBE1PBE, CAM-B3LYP, and HCTC
Gap of HOMO/LUMO	HSE, and B3PW91
Weak interaction	wB97XD, and M06

Chapter 2

Nano-sized nickel catalyst for deep hydrogenation of lignin monomers and first-principles insight into the catalyst preparation

2.1. Introduction

Nano-sized metal catalysts play crucial roles in many chemical processes, such as olefins/aromatics hydrogenation, cross-coupling, and stereoselective, electrochemical, photochemical or biochemical synthesis [1-5]. There are diverse methods for preparation of metal nanoparticles, such as chemical reduction of metal ions, thermolysis (including photolytic, radiolytic, and sonochemical pathways), and controlled decomposition of preformed metastable organometallics [6-9]. Chemical reduction in liquid phase has been the most widely accepted method, and borohydride is one of the universal reducing agents due to its highly efficient, non-toxic, and economically feasible features [10-14]. Moreover, in order to enhance the dispersion of metal particles, the metal ions are often pre-coordinated with sophisticated organic ligands such as polyvinyl pyrrolidone, polyethylenimine, and dendrimers [15-19]. Some previous studies made great efforts to develop or find new organic ligands [20-25]. Most of previous studies successfully chose the borohydride reduction to prepare metal nanomaterials, but unfortunately, with insufficient or poor understanding of apparently simple mechanism of the reduction and the true roles of the ligands. Some studies tried to clarify the mechanism by applying various experimental methods, but drawing inconsistent conclusions [26-28]. Such inconsistency was due to weak theory foundation or incorrect perceptions. For example, some studies had to employ excess borohydride for fully reducing the metal ions due to an inconclusive reaction mechanism, while others assumed that excess borohydride would cause rapid growth in size of the metal nanoparticles [10].

Hydrogenation of phenolic compounds, in particular, that of lignin monomers or oligomers, has been drawing much attention because of its importance in upgrading of pyrolytic bio-oils, lignin conversion into naphthenic or oxygenate fuel additives [29-31], bulk and fine chemicals [32], and polymers such as lignin-based phenol/epoxy resins and other types [33,34]. Although not developed yet, hydrogenation of aromatic rings of lignin, even if it is partial, or even without depolymerization, can potentially lead to new technologies for controlling chemical, mechanical, and thermal properties of such resins over broad ranges, and expressing new functions such as hydrogen storage. The hydrogenation introduces alicyclic hydrogens (i.e., those of hydroaromatic rings), which play a crucial role of capping free radicals from C−C or C−O bond breaking in pyrolysis, enhancing depolymerization [35,36]. The pyrolysis is a practical method for producing various phenolic compounds but at low yield and productivity, which is attributed primarily to insufficient net decrease in the inter-aromatic linkages that results in low liquid yield and high charcoal yield. It is expected that the

hydrogenation greatly enhances the release of lignin monomers in the subsequent pyrolysis. Many of the above require full or near-full hydrogenation of the aromatic rings, and therefore highly active and stable catalysts.

A wide variety of catalysts, based either on noble or on non-noble metals, have been applied to the hydrogenation of phenol and its derivatives as potential lignin monomers. Noble metal catalysts based on Ru, Rh, Pd, or Pt with various supports have been proposed [37,38]. Non-noble metal catalysts are normally based on Cu, Fe, and in particular, Ni [39-41]. Ni is a most widely used metal as catalyst for hydrogenation of aromatics due to its low cost and moderate activity. However, despite the long-standing practice of metal-catalyzed hydrogenation of lignin monomers, the catalyst-designing strategy still remains limited. In fact, there have so far been no reports of complete arene hydrogenation of alkyl-, hydroxyl-, methoxy- and/or aldehyde-substituted phenols. This situation is also arisen from limited understanding the mechanism of hydrogenation of phenolic substances, in particular, effects of hydroxyl and other functional groups on their reactivities.

The present authors prepared two different types of Ni nanoparticles through borohydride reduction, employing a Ni(II)-pyridine (Py) complex or a conventional salt $Ni(NO_3)_2$ as the Ni precursors. ZSM-5 zeolite was chosen as the support of Ni nanoparticles due to its practical feasibility, relatively high surface area, sufficient mechanical strength, and ability to maintain the activity of loaded metals [42]. Detailed analyses of the two catalysts successfully distinguished their properties from each other. The two catalysts were applied to hydrogenation of 14 phenolic compounds as lignin monomers with gaseous hydrogen, and their performances were compared. First-principles based on density functional theory (DFT) has been applied to many chemistry fields due to its strictness and accuracy [43-46], so in this work, DFT was employed to discuss the effects of electrostatic and steric properties of the 14 lignin monomers on their different conversion characteristics during hydrogenation. Moreover, DFT calculations were performed to understand the entire reaction process of the borohydride reduction of Ni^{2+} to Ni^0 and the possible roles of the pyridine in the nanoparticles formation.

2.2. Experimental section

Nickel(II) nitrate hexahydrate ($Ni(NO_3)_2{\cdot}6H_2O$, purity > 98.0%), sodium borohydride ($NaBH_4$, > 90.0%), ethanol (> 99.5%), and Py (> 99.0%) of reagent grades were used without further purification. ZSM-5 zeolite (ZEOLYST Int. Inc., CBV 3024E) was employed as the support. It had a SiO_2/Al_2O_3 molar ratio of 30.

The conventional Ni catalyst, hereafter referred to as Ni-N, was prepared according to the following procedure. $Ni(NO_3)_2{\cdot}6H_2O$ (3.26 mmol and corresponding to 0.191 g Ni) was dissolved in 100 mL ethanol. The ZSM-5 (3.00 g) was suspended in the solution. After stirring of the suspension at 300 rpm for 1 h, the stirring rate was increased to 600 rpm, and then powder of $NaBH_4$ (6.52 mmol) was added gradually to the suspension, while the suspension was processed at ambient temperature and under the protect cover of N_2. The suspension was continuously stirred for 0.5 h after completion of the $NaBH_4$ addition. The suspension was then subjected to evaporative removal of ethanol at 50 ℃. The resulting black-colored solid was vacuum-dried at 60 ℃, and washed

with ethanol repeatedly. The other type of Ni catalyst, which will be termed Ni-P, was prepared in the same way as the Ni-N except the addition of 11.1 mmol Py to ethanol together with $Ni(NO_3)_2 \cdot 6H_2O$. It was confirmed that the precipitation of Ni onto the ZSM-5 was complete for both of the catalysts from the absence of Ni^{2+} in the filtrates.

The catalysts were characterized by optical microscopy (OM, microscope; KEYENCE VHX-S550), transmission electron microscopy (TEM, microscope; JEOL JEM-2100F) that was combined energy dispersive spectrometry (EDS), X-ray diffraction (XRD, diffractometer; Rigaku TTR-III), N_2 adsorption/desorption (analyzer; BELSORP-mini II), X-ray photoelectron spectroscopy (XPS, spectroscope; JEOL JPS-9010), and X-ray absorption fine structure spectroscopy (XAFS). The XAFS measurements were performed at a Beamline (SAGA-LS/BL-06) of Kyushu Synchrotron Light Research Center, Japan.

Phenol (purity > 99.0%), *p*-cresol (> 99.0%), 2,4-dimethylphenol (> 99.0%), 2,3,5-trimethylphenol (> 98.0%), *p*-propylphenol (> 99.0%), *o*-methoxyphenol (> 98.0%), *o*-ethoxyphenol (> 98.0%), syringol (> 99.0%), *p*-hydroxybenzaldehyde (> 98.0%), vanillin (> 98.0%), catechol (> 99.0%), orcinol (> 97.0%), pyrogallol (> 99.0%), and syringaldehyde (> 98.0%) of reagent grades were used as lignin monomers without further purification. A single monomer (1.00 mmol) was dissolved in 20.0 mL of isopropanol (reagent grade with purity > 99.7%), which had been suspended with 0.40 g Ni-P or Ni-N. The suspension was transferred to a 100 mL SUS-made autoclave. After it was closed, the air in the headspace was replaced by H_2 at pressure of 2.0 MPa (at 25 ℃). The autoclave was then heated up to a prescribed temperature within a range of 150–180 ℃ and further heated at the temperature, while the suspension was stirred at an impeller rotation rate of 500 rpm. After the isothermal heating for a prescribed period of time, the autoclave was cooled down to ambient temperature, and opened. The suspension was recovered and filtrated immediately. The filtrate was analyzed by gas-chromatography mass-spectrometry (GC-MS, PerkinElmer Clarus 680/SQ-8S). After washed repeatedly with isopropanol and vacuum-dried at 60 ℃, the spent catalyst was characterized in the same way as the fresh one. For the hydrogenation of phenol, both Ni-N and Ni-P were used repeatedly for examining their stabilities.

All DFT calculations were performed by employing a hybrid functional, Minnesota 06 (M06), which had been implemented in the Gaussian 09 package [47]. The M06 functional is recommended for application to thermodynamics of organometallic and inorganometallic molecules, kinetics and non-covalent bonds [48]. The scalar relativistic effective core potential with double-zeta basis set (LanL2DZ) was adopted for the Ni atoms, while the 6-31++G(d,p) basis set was applied to the H, B, C, N, and O atoms for all of the reaction systems considered [49]. Fully relaxed geometry optimizations and energetic calculations were performed for all intermediates (INT) and transition states (TS) under tight optimization convergence criteria [50]. The vibrational frequencies were calculated at the same basis set levels to identify a local energy minimum (no imaginary frequency) or a TS (unique imaginary frequency) and to perform zero-point vibrational to energy corrections for thermodynamic data at 298 K [51]. To check the energy profiles, intrinsic reaction coordinates were traced. In

addition, ultrafine numerical integration grids were used for all calculations. Self-consistent field procedures of full accuracy were performed with tight convergence and without any orbital symmetry constraints [52]. In consideration of the reaction field of ethanol, self-consistent reaction field based on the polarizable continuum model of Tomasi's group is employed for the simulation of solvent molecules in the vicinity [53].

2.3. Results and discussion

2.3.1. Catalyst characterizations

Figure 2-1 displays photographs and optical micrographs of Ni-N, Ni-P, and the support ZSM-5. The figure also shows Ni particles precipitated in the same ways as those for Ni-N and Ni-P but without ZSM-5 support. The Ni loadings of Ni-N and Ni-P were equivalent to each other at 6 wt%, which was determined by a sequence of complete dissolution of Ni into HNO_3–HF mixed acids and analysis of the solution by inductively coupled plasma optical emission spectrometry (ICP-OES). As seen in the photos a1 and a2, the appearances of Ni-N and Ni-P are clearly different from each other. It was suspected that such difference was due to the presence or abundance of coarse Ni particles in Ni-N while no or very few in Ni-P. In other words, the visible light scattering on the surface of coarse Ni particles resulted in a black color of Ni-N. It was also suggested that the sizes of Ni particles in Ni-P were well below visible light wavelengths, and therefore colorless [54]. In fact, the optical microscopy detected coarse Ni particles as black colored dots (Photo c1), whose sizes were even more than 1 μm. In contrast to this, there were no such coarse Ni particles on Ni-P (Photo c2). The difference in appearance between Ni-N and Ni-P also occurred for Ni particles prepared without the ZSM-5 support (Photos b1 and b2). It was thus speculated that the presence of Py effectively prevented the formation of coarse Ni particles.

Ni-N and Ni-P were also observed by TEM. **Figure 2-2** exhibits that nano-sized Ni particles have been loaded on the surface of ZSM-5 for both Ni-N and Ni-P, while a large amount of coarse Ni particles are observed only on Ni-N. The TEM images show well-dispersed Ni particles of Ni-P with a mean size of 4 nm and with a relatively narrow size distribution, while a greater mean size (7 nm) and wider size distribution for Ni-N. As shown in the EDS maps for Ni (**Figure 2-3**), coarse Ni particles are detected on Ni-N, but no such particles on Ni-P. This fact verifies the effectiveness of Py for selective formation of the nano-sized Ni.

Figure 2-4 presents the XRD patterns of Ni-N, Ni-P, and the ZSM-5 without Ni loading. The figure also shows the reference XRD patterns of pure crystalline Ni, NiO, and Ni_2B. The patterns of Ni-N and Ni-P are very similar to that of ZSM-5. Moreover, none of the peaks for Ni, NiO, and Ni_2B match to those for Ni-N and Ni-P. The same result was obtained for the Ni particles prepared in the same way as Ni-N and Ni-P but without ZSM-5 support. **Figures 2-5** and **2-6** indicate that the Ni prepared through our method are amorphous or consists of sufficiently small crystals. This analytical result is consistent with that shown in **Figure 2-2**.

Figure 2-7 compares N_2 adsorption/desorption isotherms for ZSM-5, Ni-N, and Ni-P, of which specific BET surface areas were 400, 331, and 311 m^2/g, respectively. The micropore surface areas of ZSM-5 and Ni-N,

estimated by applying a *t*-plot method, were 260 and 258 m^2/g, respectively. This indicated no significant incorporation of Ni species into the support micropores for Ni-N. On the other hand, Ni-P had a micropore surface area of 243 m^2/g, slightly smaller than the others. It was implied that a portion of Ni had been deposited at the micropore mouths of ZSM-5 closing the pores. The corresponding external surface areas of ZSM-5, Ni-N, and Ni-P were thus 140, 73, and 68 m^2/g, respectively. Deposition of Ni particles at mesopore surface and nano-sized interfacial spaces among ZSM-5 crystals seemed to be responsible for the decrease in the total specific surface area of ZSM-5.

The XPS did not detect any boron species on the surface of either Ni-N or Ni-P (see **Figure 2-8**). This result was in agreement with that of XRD. Some previous studies reported that metal-boron species were always present when the borohydride reduction was employed [10-14]. This inconsistency will be explained theoretically in the following part of this chapter. The XPS spectra of **Figure 2-9** indicate the presence of NiO, metallic Ni, and Ni-Si species [55-59]. Ni-P contains less metallic Ni but more NiO and Ni-Si species than Ni-N. The presence of the Ni-Si species is a strong indication of occurrence of chemical bonding between Ni and Si of ZSM-5. More abundant Ni-Si species on Ni-P probably means more abundant nano-sized Ni particles. In other words, there were fewer coarse Ni particles on the surface of Ni-P than that of Ni-N.

Figure 2-10 shows the EXAFS and XANES spectra of Ni from fresh and spent Ni-N and Ni-P. **Figure 2-10** also shows the spectra of reference materials, i.e., Ni foil and crystalline NiO. Each spent catalyst was recovered from a single run of catalytic hydrogenation of phenol. The XAFS spectra show that both the fresh Ni-N and Ni-P consist mainly of Ni-O species. Compared with the reference crystalline NiO, the Ni-O species of the fresh catalysts seem to be highly unordered. The comparison of the EXAFS spectra between the fresh and spent catalysts is more important. It is clear that metallic Ni is a major species for the spent Ni-N. The original NiO particles of Ni-N had undergone reduction and growth in size (caused by coalescence) during the run of hydrogenation. The resultant coarse metallic Ni particles might have been oxidized slightly by exposure to air after recovery. TEM observation of the spent Ni-N has demonstrated the coalescence of Ni particles (see **Figure 2-11**). Most of the Ni particles left on the spent Ni-N surface had sizes greater than 10 nm. In contrast to this, it is hard to distinguish the EXAFS spectrum of the spent Ni-P from that of the fresh one. It was believed that the original NiO particles of Ni-P underwent the reduction during catalytic hydrogenation probably in the same way as that of Ni-N, but without particles growth in size. Sufficiently small sizes of metallic Ni particles (5 nm or smaller size according to TEM observation) on the spent Ni-P allowed them to experience oxidation in air easily and to return rapidly to a state very similar to that of the fresh Ni-P. The higher stability of Ni-P than that of Ni-N was thus demonstrated. As reported later, the activity of Ni-P was stable in repeated use for the hydrogenation, while that of Ni-N was lost gradually.

2.3.2. Hydrogenation of lignin monomers

To fully evaluate the catalytic performances of Ni-N and Ni-P in the hydrogenation, we chose phenol (compound No. 1) and its 13 derivatives (No. 2 to 14) as lignin monomers. These lignin monomers are classified into four groups in terms of substituents, i.e., alkyl (No. 2 to 5), alkoxy (No. 6 to 8), poly-hydroxyl (No. 9 to 11), and aldehyde (No. 12 to 14) groups. **Table 2-1** summarizes the results of hydrogenation, showing the different catalytic activities between Ni-N and Ni-P. All of the monomers were completely converted at 180 ℃ and within 3 h in the presence of Ni-P. The products were cyclohexanol or its derivatives except the cases of vanillin (total yield of cyclohexanols; 98%) and syringaldehyde (total yield of cyclohexanols; 61%). Ni-N was clearly less active than Ni-P. Under the catalysis of Ni-N, only 70% of 2,4-dimethylphenol (No. 3) and 19% of 2,3,5-trimethylphenol (No. 4) were converted into the cyclohexanols. The cyclohexanols yields from No. 6 and No. 8 with methoxy substituents remained 32–59%. The hydrogenation of vanillin (No.13) and that of syringaldehyde (No. 14) were even more difficult, and it resulted in the cyclohexanols yields as low as 26% and 0.7%, respectively. The result shown in **Table 2-1** is the first demonstration of complete hydrogenation of lignin monomers (except No. 13 and 14) over Ni catalyst supported by a general material (i.e., ZSM-5). It should be stated that Ni-P is clearly more active than Ni-N.

A number of previous studies proposed mechanisms for the hydrogenation of phenolic compounds over supported metal catalysts [29-31, 60-62]. These mechanisms were more or less similar to one another regardless of the support materials (alumina, SiO_2, activated carbon, or zeolites) and loaded metals (Ni, Ru, Pt, or Pd). A typical mechanism, in brief, consists of the following sequence. The phenolic molecule is chemisorbed on the metal surface, forming a π-complex between the aromatic ring and several abreast metal atoms. The aromatic ring gradually accepts hydrogen atoms that are supplied from adjacent metal atoms. The hydrogenated aromatic ring is then desorbed from the metal surface. The formation of the π-complex is a crucial step and its rate largely depends on the electrostatic and steric properties of the molecule.

Table 2-2 illustrates the electrostatic potentials of the monomers, which were calculated by applying DFT. The negative potential concentrated area of phenol is generated by a super π-bond of the aromatic ring hyperconjugated with the O atom of the hydroxyl group. This hydroxyl group locates on the same plane as that of the aromatic ring, causing no steric hindrance. The chemisorption of phenol (a Lewis base) will thus be easy and fast on either Ni surface (a Lewis acid). The methyl group of cresol (No. 2) does not significantly influence the electrostatic potential of the aromatic ring, and its steric hindrance effect is very limited because the rotation of the σ Ph−CH_3 bond causes no significant change of the molecular shape. Cresol is thus hydrogenated completely over both Ni-N and Ni-P. With increasing number of methyl groups (No. 3 and 4), the steric hindrance becomes prominent. Note that the positive potential concentrates at the H atoms of methyl groups, which repulse the acidic metal surface. This behavior makes the chemisorption of the monomers No. 3 and 4 on the catalyst metal surface difficult. The conversions of No. 3 and 4 are therefore as low as 70.1% and 18.8% over Ni-N, respectively. Their

complete conversion was, however, realized over Ni-P. This was attributed to the higher catalytic activity of Ni-P than Ni-N, which was mainly arisen from a much higher dispersion of the loaded nano-sized Ni. These highly-dispersed Ni particles served abundant chemisorption sites for the aromatic rings, thereby increasing the rate of reactions leading to the hydrogenation.

As for alkylphenols, the steric effect depends largely on the number of alkyl substituents, rather than the substituent size. In the presence of Ni-N, the conversion of propylphenol (No. 5) is 96.4%, which is much higher than those of No. 3 and 4. This is because the propyl group locates at only one side of the aromatic ring plane, and the chemisorption by the other side of the aromatic ring is not strongly inhibited.

Once an aromatic H atom of phenol is substituted by an alkoxy group (see No. 6 and 7), the negative potential concentrated area on the aromatic ring will be somewhat offset by a negative inductive effect of the alkoxy group. Meanwhile, the negative potential extends to the O atom of the alkoxy group due to the hyperconjugation. The cumulative result is that the monomers No. 6 and 7 can be hydrogenated deeply to cyclohexanols with high yields over both Ni-N and Ni-P, but a portion of the product is generated through the hydrogenolysis of the alkoxy group, which is significant for Ni-N. The hyperconjugation for syringol (No. 8) is more remarkable than those for No. 6 and 7. The conversion of No. 8 over Ni-N is, however, clearly lower than those of No. 6 and 7. This is attributed to that the two methoxy groups induce a more severe steric effect than that of a methoxy or ethoxy group for the chemisorption of No. 8 onto Ni-N. A complete conversion of No. 8 is, however, obtained over Ni-P. The main reason of this seemed to be the same as or similar to that for No. 3 and 4, as mentioned above.

The hydrogenation of polyphenols (No. 9 to 11) seems to be ideal over both Ni-N and Ni-P. This is mainly because the electrostatic natures of the monomers No. 9 to 11 are conducive to the chemisorption of the aromatic rings on the metal surface. Although the negative inductive effect of extra phenolic hydroxyl groups slightly increases the electrostatic potential nearby the hydroxyl-substituted aromatic C atoms, the hyperconjugation almost extends the negative potential to the entire molecular plane. Moreover, the extra phenolic hydroxyl groups provide little steric hindrance due to the same reasons as that for phenol. The polyphenols are chemisorbed thus easily onto the metal surface and then hydrogenated.

Even in the presence of Ni-P, the hydrogenation of the monomers No. 12 to 14 that carry aldehyde groups left products without hydrogenation at substantial yields. Over both Ni-N and Ni-P, the hydrogenation of aldehyde to methyl group seemed to be easy and at the highest priority. **Table 2-2** explains this clearly. The aldehyde group of No. 12 attracts the electrons of entire molecule so strongly that the electrostatic potential on the aromatic ring turns near neutral. As for No. 13 and 14, the hyperconjugation between the aromatic ring and the O atom of methoxy group is little helpful to lowering the electrostatic potential. Thus, the aldehyde groups of No. 12 to 14 are converted primarily to the methyl groups, leaving their aromatic rings with much lower reactivities.

Figure 2-12 compares the kinetics of phenol hydrogenation at 150−180°C. Under assumptions of a constant pressure of H_2 and no catalyst deactivation, the linear relationship between the natural logarithm of unconverted fraction, $ln(1–X)$, and the reaction time indicates that the hydrogenation of phenol obeys first-order kinetics with respect to the phenol concentration. It was difficult to determine the overall activation energies for Ni-N and Ni-P because of scattering of $–lnk$ *vs* $1/T$ data points, but it also seemed that those energies were more or less similar to each other within a range of 130–140 kJ/mol. On the other hand, the rate constant for Ni-P is clearly greater than that for Ni-N. For example, the former is greater than the latter by a factor of 13.9. The difference in the activity between Ni-P and Ni-N is attributed mainly to that in the frequency of reaction, and then, active surface area of Ni particles. The stabilities of Ni-N and Ni-P were investigated by subjecting them to five-time repetition of the phenol hydrogenation at 180 ℃ for 3 h. As shown in **Figure 2-13**, the activity of Ni-N decreases monotonously by the repeated use while Ni-P seems to maintain the initial activity. The higher stability of Ni-P is explained reasonably by the result of the XPS as well as XAFS analyses. The chemical interaction occurring between Ni and Si played a role to fix Ni nanoparticles onto the surface of the support inhibiting their motion toward coalescence.

2.3.3. Mechanism of borohydride reduction of Ni^{2+} to Ni^0

In this section are discussed the mechanism of the borohydride reduction of Ni^{2+} to Ni^0 and the role of pyridine. The results of the DFT calculations reveal some unexpected features of the reduction, but these are supported by the experimental facts.

A concise mechanism of the entire reduction process is shown in **Scheme 2-1**. In consideration of the spontaneous, fast and thorough reaction between BH_4^- and Ni^{2+} at ambient temperature, it is reasonable to assume that the free energy (E_G) of an intermediate (INT) on the most probable reaction pathway is lower than its antecedents. Along with such pathway, the energy barrier for each step should be lower than 30 kcal/mol. Once BH_4^- is formed in the solution, it will immediately bond with Ni^{2+} through electrostatic attraction and coordination, and forms $Ni(BH_4)_2$. As shown in **Table 2-3**, the energy of $Ni(BH_4)_2$ at the triplet state is lower than that of the singlet one. This means that the triplet state is more stable, and that the configuration of the 3*d* orbital electrons of Ni^{2+} center does not change at the coordination with BH_4^-. To retain redundant electrons available in the Ni^{2+} reduction, the Ni^{2+}–BH_4^- coordination system must lose neutral H atoms by releasing H_2. $Ni(BH_4)_2$ is, however, so stable that any operations rearranging its atoms would sharply enhance the energy. In other words, none of the intramolecular reactions of $Ni(BH_4)_2$ is spontaneous. Then the dehydrogenation occurs probably between two $Ni(BH_4)_2$ molecules, of which total spin state is quintet. A series of bimolecular $Ni(BH_4)_2$ systems were calculated according to the collision theory (see **Table 2-4**). E_Gs of all the bimolecular systems are much higher than twice that of $Ni(BH_4)_2$. Moreover, a shorter distance between two $Ni(BH_4)_2$ molecules results in a higher E_G. It is implied that stable $Ni(BH_4)_2$ molecules tend to depart from rather than react with each other.

An initial step proposed for the bimolecular reaction is the coordination of $Ni(BH_4)_2$ with BH_4^- to form $[Ni(BH_4)_3]^-$, which combines with Ni^{2+} to form $[Ni_2(BH_4)_3]^+$. This reaction is followed by further coordination

with BH_4^- to form $Ni_2(BH_4)_4$. The $Ni_2(BH_4)_4$ molecule with a compact geometry can finally undergo the dehydrogenation. As shown in **Table 2-5**, E_G of $[Ni(BH_4)_3]^-$ is much lower than the sum of E_Gs of BH_4^- and $Ni(BH_4)_2$. The negative potential concentrated area of $[Ni(BH_4)_3]^-$ provides strong electrostatic attraction and sufficient coordination sites for incorporating $^2Ni^{2+}$ to form $[Ni_2(BH_4)_3]^+$. A positive potential concentrates near the ^2Ni atom of the $[Ni_2(BH_4)_3]^+$, and this atom has not fully been coordinated yet. $[Ni_2(BH_4)_3]^+$ attracts and bonds with BH_4^- to form $Ni_2(BH_4)_4$. There are five possible types of $[Ni_2(BH_4)_3]^+$ with optimized geometries. These can transform one another over very small energy barriers (see **Figure 2-14**). Note that all of the $[Ni_2(BH_4)_3]^+$ can spontaneously bond with BH_4^-, but not all of the newly formed $Ni_2(BH_4)_4$ molecules can be dehydrogenated. The geometries of $Ni_2(BH_4)_4$ generated from Case 1 to Case 4 $[Ni_2(BH_4)_3]^+$ do not allow dehydrogenation because H atoms belonging to different BH_4^- groups are far apart from each other. Even though such $Ni_2(BH_4)_4$ molecules were formed, they would decompose into two $Ni(BH_4)_2$ molecules rather than undergo dehydrogenation.

Among the five cases, only Case 5 $[Ni_2(BH_4)_3]^+$ can be converted to an active $Ni_2(BH_4)_4$. As seen in **Table 2-6**, the $^4BH_4^-$ coordinates with the ^2Ni atom to form the $Ni_2(BH_4)_4$ (INT-1Q), in which the distance between ^4H_I and ^2H_I atoms is as short as 1.106 Å. These two H atoms are prone to combine to H_2. INT-1Q can transform into INT-2Q through TS-1Q-2Q. The energy barrier for this transformation is as small as 2.8 kcal/mol. In the H_2 removal process, the reaction system holds two electrons from antecedent $^2BH_4^-$ and $^4BH_4^-$. Meanwhile, $^4BH_3$ and $^3BH_4^-$ access mutually, and INT-2Q is converted spontaneously to INT-3Q. Following INT-3Q, none of the INTs with quintet spin state has lower energy than INT-3Q or leads to the final products. It was eventually found that the system changed its spin state to evolve into a series of desirable INTs after INT-3Q.

Table 2-7 shows the transformation of INT-3Q to INT-4T, which is associated with a quintet-to-triplet spin state change. There may be TS-3Q-4T between the INT-3Q and INT-4T, but without energy barrier. The *p* orbital of ^2B atom makes considerable contributions to the formation of the two α orbitals in INT-3Q, and at last, only a *d* single electron remains at each Ni atom of the INT-4T. This indicates that π backdonation from the Ni to the BH_3 occurs after the dehydrogenation. There are no vacant B_p orbitals to accommodate the abundant *d* single electrons from the Ni atoms of $Ni_2(BH_4)_4$, so its spin state remains quintet until the H_2 formation. As shown in **Table 2-8**, changing the spin state from quintet to triplet, INT-2Q also transforms into INT-2T. The prerequisite for this transformation is the vacant ^2B_p orbital, which allows two *d* single electrons from the Ni atoms to pair up. The dehydrogenation of INT-2T gives INT-3T (see **Table 2-9**). INT-3T then transforms into INT-4T via TS-3T-4T without energy barrier. It is difficult to exactly predict the more preferred pathway to the dehydrogenation, but it can at least be said that INT-1Q finally transforms into INT-4T.

Further dehydrogenation may not be responsible for the conversion of the INT-4T. There are two hydrogen bridge bonds among ^2B, ^3B, and ^4B of INT-4T. Meanwhile, $^1BH_4^-$ strongly coordinates with ^1Ni atom, and there are no H atoms active enough to form another H_2. It is hence proposed that the reaction will continue removing B_2H_6. As shown in **Table 2-10**, INT-4T generates INT-5T through TS-4T-5T. Leaving $^3H_{III}$ at ^2B to newly form

the $^{2}BH_4^-$, $^{3}H_I$-^{3}B-$^{3}H_{II}$ moves to the middle of $^{3}H_{IV}$ and $^{4}H_I$ to form the B_2H_6. Under the action of ethanol, INT-5T decomposes into three molecules, i.e., two $NiBH_4$ molecules (INT-1D) that will coordinate with ethanol molecules, and a B_2H_6 molecule. The spin state of the neutral INT-1D is doublet because there is only one unpaired *d* electron of the Ni atom (see **Table 2-11**).

As seen in **Table 2-11**, Ni^{2+} has been reduced to Ni^{+} until INT-1D formation. It is expected that INT-1D reacts with ethanol to continue the reduction. In **Figure 2-15** (a), an ethanol molecule is extracted from the surrounding solvent. Ni^{+} of INT-1D then coordinates with the O atom of the ethanol spontaneously, forming INT-$1D_{1ET}$. Only ^{3}H of the BH_4^- reacts with the ethanol since the ^{1}H and ^{2}H are strongly coordinated with the Ni^{+}. The ethanol moves from the equatorial coordination site to the axial locus approaching the ^{3}H. Meanwhile, the ^{O}H departs from the O atom to bond with the synchronously dissociated ^{3}H to form TS-$1D_{1ET}$-$2D_{1ET}$. Then, it undergoes dehydrogenation to form INT-$2D_{1ET}$. However, E_G of INT-$2D_{1ET}$ is much greater than that of INT-$1D_{1ET}$, and the energy barrier of this elementary reaction is as high as 45.0 kcal/mol. This means that the reaction is not spontaneous at ambient temperature. Such high energy barrier is contributed partly by the significant translocation of the ethanol during the dehydrogenation. Therefore, as shown in **Figure 2-15** (b), another reaction of INT-$1D_{2ET}$, which contains two ethanol molecules (^{1}ET and ^{2}ET), is considered.

In **Figure 2-15** (b), the Ni atom is coordinated with the ^{1}ET and ^{2}ET at the axial locus due to a steric effect. This allows the ^{1}ET to react with the ^{3}H but without translocation. Although the core mechanism of the INT-$1D_{2ET}$ dehydrogenation is the same as that of the INT-$1D_{1ET}$, the energy barrier for the former, 32.4 kcal/mol, is clearly lower than that for the latter, 45.0 kcal/mol. Moreover, the product INT-$2D_{2ET}$ is more stable than INT-$2D_{1ET}$. Further reaction of INT-1D with ethanol is possible by assuming INT-$1D_{3ET}$ that is coordinated by three ethanol molecules (^{1}ET, ^{2}ET, and ^{3}ET). As seen in **Figure 2-15** (c), although ^{3}ET interacts with ^{1}ET via a hydrogen bond, instead of bonds with the Ni atom, the relative energy of the product INT-$2D_{3ET}$ and the energy barrier are further reduced to –3.7 and 27.2 kcal/mol, respectively. This calculation result rationalizes the reaction between INT-1D and ethanol.

INT-$2D_{2ET}$ is chosen for the calculation of the next reaction step. Its dehydrogenation forms INT-3D, as shown in **Figure 2-16**. In INT-3D, ^{1}O and B atoms have much less ability to coordinate with the Ni center than BH_4^-, so that the H_2B-O- and ^{1}H-Ni groups can move away from each other to generate INT-4D through TS-3D-4D. While INT-4D is converted to INT-5D through TS-4D-5D, the ^{O}H moving away from the O atom of the ethanol comes close to the active ^{1}H, and finally forms H_2. Then, INT-5D is transformed into INT-6D through TS-5D-6D, while the Ni-^{2}O approaches the $^{2}H^{3}H$-B-^{1}O groups inducing a B-O bond (^{1}O-B-^{2}O). The ^{O}H-^{1}H (i.e., H_2) moves from the equatorial site of the Ni center to its axial locus, getting ready for dehydrogenation. The product INT-6D is more stable than any other INTs ranging from INT-3D to INT-5D. The highest energy barrier on the pathway from INT-3D to INT-6D is only 14.9 kcal/mol even without supply of other ethanol molecules.

INT-7D is formed by the dehydrogenation of INT-6D. The coordination ability of the $H_2B(OEt)_2$ group of the INT-7D is so weak that the Ni atom is released from the chelating site. This clearly explains why no Ni-B species are produced. As seen in **Figure 2-17**, the positive potential concentrated at the Ni atom of INT-7D moves toward the ^{2}O atom and then accesses to the negative potential concentrated ^{1}H atom. This results in the formation of INT-8D. The Ni atom of INT-8D bonds with the ^{1}H so strongly that INT-8D can split into two neutral molecules, i.e., NiH and $HB(OEt)_2$. On this reaction step, $H_2B(OEt)_2$ donates the $[H:]^-$ to the Ni^+ to accomplish the final reduction. $HB(OEt)_2$ may further react with an ethanol molecule to form $B(OEt)_3$ and H_2.

The neutral NiH is recognized as a Ni^0 chemisorbing a H atom (see **Table 2-12**). The dehydrogenation of NiH to Ni is examined by assuming two molecules of NiH. When the two molecules interact with each other, each NiH still holds one unpaired electron. As shown in **Figure 2-18** (a), the two NiHs form INT-10D spontaneously. The ^{1}H approaches the ^{2}H through rotation of the ^{1}H-^{1}Ni bond, and then the newly formed ^{1}H-^{2}H dissociates from the two Ni atoms. Since E_G of INT-11D is much greater than that of INT-10D, the pathway from INT-10D to INT-11D is implausible. The inverse process is, however, consistent with a well-known fact that the bare Ni atoms are active enough to chemisorb and cleave H_2 molecules spontaneously. This result suggests participation of ethanol molecules in the final stage of dehydrogenation.

As shown in **Figure 2-18** (b), the interaction between the INT-10D and an ethanol molecule does not change the core mechanism of dehydrogenation shown in the reaction of alone INT-10D, but it causes both E_Gs of the INTs and the energy barrier decrease significantly. In other words, the dehydrogenation of the two NiHs is facilitated. Besides INT-11D and INT-11D$_{1ET}$, other two possible products INT-11D' and INT-11D'$_{1ET}$ were found in the calculation. However, the interaction between the H_2 and the ^{1}Ni atom of INT-11D'/INT-11D'$_{1ET}$ is arisen only from Van der Waals force. Moreover, there is no TS between INT-11D' and INT-10D, as well as between INT-11D'$_{1ET}$ and INT-10D$_{1ET}$. It is implied that the axial chemisorption of the H_2 molecule onto the two Ni atoms cannot lead to H_2 dissociation. Dehydrogenation of NiH gives Ni^0s. This reaction step will be followed by the deposition of Ni atoms onto the surface of the support, and formation of Ni clusters/particles.

The authors found another potential reaction pathway after the INT-5T. Besides its decomposition into two $NiBH_4$ molecules and one B_2H_6, the INT-5T can also decompose into one B_2H_6 and one $Ni_2(BH_4)_2$, even though this reaction is not favored thermodynamically. The $Ni_2(BH_4)_2$ first loses a H_2 to form a $Ni_2(BH_3)_2$. Strongly coordinated with the two BH_3 groups, the two Ni atoms have already been reduced to zero valent. The six H atoms of the $Ni_2(BH_3)_2$ successively react with six ethanol molecules to form a $Ni_2[B(OEt)_3]_2$ and six H_2 molecules. Finally, two Ni atoms of zero valent and two $B(OEt)_3$ molecules are obtained. The authors have deduced the entire possible mechanism of BH_4^- reducing Ni^{2+} in ethanol. According to all the above-mentioned possibilities and calculations, the conclusive overall stoichiometry is:

$$2Ni^{2+} + 4BH_4^- + 6EtOH = 2Ni + 8H_2 + B_2H_6 + 2B(OEt)_3$$

In order to examine this mechanism experimentally, the filtrates from the catalyst preparation were analyzed. As shown in **Figure 2-19**, GC-MS detected $B(OEt)_3$ in the filtrates for both Ni-N and Ni-P. It was also found that the evaporative removal of ethanol from the filtrates left only crystalline $NaNO_3$ but no $Ni(NO_3)_2$.

2.3.4 Role of pyridine

The proposed mechanism is further examined. Even when the Ni^{2+} salt precursor is replaced by a type of complex of Ni^{2+} and an organic ligand, the reduction mechanism probably remains unchanged, as far as the BH_4^- coordinates with Ni^{2+} strongly, and reduces it very rapidly. The formation of highly dispersive Ni particles is attributed primarily to that the ligands markedly inhibit the growth, coalescence and aggregation of Ni particles, rather than reduce the rate of reduction.

Herein, we evaluate the impacts of the presence of Py before, during, and after the Ni^{2+} reduction. It is believed that a major portion of Ni^{2+} coordinates with Py forming $[NiPy_2]^{2+}$ in the ethanol solution. The maximal energy of 'bond-antibond' interactions (ΔE_{max}) between the Py and the Ni center (ΔE_{max}-NiPy) of $[NiPy_2]^{2+}$ is 20.6 kcal/mol greater than that between the NO_3^- and the Ni center (ΔE_{max}-$NiNO_3$) of $Ni(NO_3)_2$. At the moment of the first BH_4^- coordination with the Ni^{2+} center, the difference between ΔE_{max}-NiPy and ΔE_{max}-$NiNO_3$ decreases to 10.7 kcal/mol. By the second BH_4^- coordination with the Ni center, the $Ni(BH_4)_2$ is formed. Neither the NO_3^- nor the Py is dissociated from the complexes for the moment. It is recognized that the ΔE_{max}-NiPy and the ΔE_{max}-$NiNO_3$ are almost equivalent to each other. It is thus inferred that the dissociation of the Py is as easy as that of the NO_3^- at this moment. In other words, the presence of Py does not markedly change the initial rate of Ni^{2+} reduction.

Py can also coordinate with $NiBH_4$. In **Table 2-13**, two Py molecules instead of ethanol coordinate with the Ni center of $NiBH_4$. The most probable products from the decomposition of H_4BNiPy_2 are HNiPy and H_3BPy. This decomposition is not spontaneous. It is therefore concluded reasonably that the reaction between the $NiBH_4$ and ethanol is still preferable even in the presence of Py. In other words, the influence of Py, if any, is slight on the overall rate of Ni^{2+} reduction. After the reduction, the newly formed Ni^0 atoms must interact with ethanol or Py molecules in the vicinity. The dissociation of Ni-ethanol or Ni-Py species is required for the formation of Ni-Ni bonds to initiate the generation of Ni particles or clusters. ΔE_{max}-NiPy is 23.4 kcal/mol, while ΔE_{max} of Ni-ethanol is only 9.9 kcal/mol. Such difference should cause marked difference in the rates of growth, coalescence and aggregation of Ni particles before their deposition onto the support. It is therefore predicted that the presence of Py leads to a higher dispersion of Ni particles on the support. The more intensified interaction between Ni and the support due to greater specific surface area of smaller particles can be deemed as the secondary effect of Py.

2.4. Conclusions

This chapter has proposed a simple method for preparation of a type of ZSM-5-supported Ni catalyst (Ni-P). The addition of Py to the ethanol solution of $Ni(NO_3)_2$ prior to the Ni^{2+} to Ni^0 reduction with BH_4^- realizes

selective formation and deposition of Ni particles with sizes around 4 nm without coarser particles. Such selectivity cannot be achieved by a conventional catalyst Ni-N prepared through the reduction of $Ni(NO_3)_2$ without Py, which inevitably allows formation of much coarser Ni particles. The Py addition is also effective for enhancing the chemical and therefore stable bonding of Ni nanoparticles to the surface of the support.

Ni-P has a sufficiently high activity as to completely or near completely hydrogenate phenol and its twelve derivatives with one or more alkyl, alkoxy or hydroxyl substituents at 180 ℃, while the activity is not necessarily enough for complete hydrogenation of vanillin and syringaldehyde that have both aldehyde and methoxy substituents. Not only the activity but also stability of Ni-P is much higher than those of Ni-N. These are arisen from that Ni-P has the higher effective surface area of Ni and its stronger interaction with the surface of the support than Ni-N. The variety of molecular electrostatic and steric natures of the fourteen phenolic substances reasonably explains that of their reactivities toward the hydrogenation.

The borohydride reduction is summarized by the stoichiometry of $2Ni^{2+} + 4BH_4^- + 6EtOH = 2Ni + 8H_2 + B_2H_6 + 2B(OEt)_3$. Each BH_4^- anion only serves one electron to Ni^{2+} reducing it to Ni^+ but, not to Ni^0. The Ni^+ is further reduced to Ni^0 through reactions with ethanol while BH_4^- loses the ability to coordinate with Ni^+. The clearly higher activity and stability of Ni-P than Ni-N are arisen from a particular role of Py. It hardly influences the overall rate of reduction, but coordinates with Ni^0, decelerating the subsequent formation of Ni clusters and particles that requires the formation of Ni-Ni bonds, and thereby the following processes of deposition onto the support surface of Ni nanoparticles and their growth.

2.5. Nomenclatures

DFT	density functional theory
Py	pyridine
Ni-P	Ni/ZSM-5 catalyst employing Ni(II)-pyridine complexes as Ni precursor
Ni-N	Ni/ZSM-5 catalyst employing $Ni(NO_3)_2 \cdot 6H_2O$ as Ni precursor
OM	optical microscopy
TEM	transmission electron microscopy
EDS	energy dispersive spectrometry
XRD	X-ray diffraction
XPS	X-ray photoelectron spectroscopy
XAFS	X-ray absorption fine structure spectroscopy
EXAFS	extended X-ray absorption fine structure
XANES	X-ray absorption near edge structure
INT	intermediate
TS	transition state

INT-nM	an intermediate encoded as 'nM' (n, serial number; M, spin multiplicity, M = D, doublet; T, triplet; or Q, quintet)
INT-nM$_{x\mathrm{ET}}$	an intermediate formed by INT-nM coordinating or reacting with *x* ethanol molecules
TS-nM-n'M'	a transition state bridging INT-nM and INT-n'M'
TS-nM$_{x\mathrm{ET}}$-n'M'$_{x\mathrm{ET}}$	a transition state bridging INT-nM$_{x\mathrm{ET}}$ and INT-n'M'$_{x\mathrm{ET}}$
E_a	activation energy
E_G	free energy
ΔE_max	maximal energy of 'bond-antibond' interactions

2.6. References

1 A. Stanislaus and B. H. Cooper, *Catal. Rev.*, 1994, **36**, 75-123.

2 K. Tamao, *J. Organomet. Chem.*, 2002, **653**, 23-26.

3 M. Takimoto, Y. Hiraga, Y. Sato and M. Mori, *Tetrahedron Lett.*, 1998, **39**, 4543-4546.

4 K. Urgin, R. Barhdadi, S. Condon, E. Léonel, M. Pipelier, V. Blot, C. Thobie-Gautier and D. Dubreuil, *Electrochim. Acta*, 2010, **55**, 4495-4500.

5 K. Saravanakumar, D. MubarakAli and K. Kathiresan, *Mater. Sci. Eng. B*, 2016, **203**, 27-34.

6 X. Fu, Y. Wang and N. Wu, *Langmuir*, 2002, **18**, 4619-4624.

7 A. Henglein, A. Holzwarth and P. Mulvaney, *J. Phys. Chem.*, 1992, **96**, 8700-8702.

8 B. G. Ershov, E. Janata, M. Michaelis and A. Henglein, *J. Phys. Chem.*, 1991, **95**, 8996-8999.

9 K. S. Suslick and J. Prince, *Annu. Rev. Mater. Sci.*, 1999, **29**, 295-326.

10 N. Toshima, H. Yan and Y. Shiraishi, *Metal Nanoclusters in Catalysis and Materials Science, the Issue of Size Control*, Elsevier, Amsterdam, 2008.

11 A. Roucoux, J. Schulz and H. Patin, *Chem. Rev.*, 2002, **102**, 3757-3778.

12 N. M. Deraz, *Int. J. Electrochem. Sci.*, 2012, **7**, 4608-4616.

13 H. Hirai, H. Aizawa and H. Shiozaki, *Chem. Lett.*, 1992, **8**, 1527-1530.

14 S. Chen, H. Yao and K. Kimura, *Langmuir*, 2001, **17**, 733-739.

15 Z. Yang, M. R. Berber and N. Nakashima, *J. Mater. Chem. A*, 2014, **2**, 18875-18880.

16 Z. Yang, T. Fujigaya and N. Nakashima, *J. Mater. Chem. A*, 2015, **3**, 14318-14324.

17 Z. Yang, I. Moriguchi and N. Nakashima, *ACS Appl. Mater. Interfaces*, 2016, **8**, 9030-9036.

18 Z. Yang and N. Nakashima, *ChemCatChem*, 2016, **8**, 600-606.

19 L. J. Grove, J. M. Rennekamp, H. Jude and W. B. Connick, *J. Am. Chem. Soc.*, 2004, **126**, 1594-1595.

20 A. B. R. Mayer, J. E. Mark and S. H. Hausner, *Angew. Makromol. Chem.*, 1998, **259**, 45-53.

21 J. H. Youk, J. Locklin, C. Xia, M. K. Park and R. Advincula, *Langmuir*, 2001, **17**, 4681-4683.

22 L. Balogh and D. A. Tomalia, *J. Am. Chem. Soc.*, 1998, **120**, 7355-7356.

23 M. Zhao, L. Sun and R. M. Crooks, *J. Am. Chem. Soc.*, 1998, **120**, 4877-4878.

24 V. Chechik and R. M. Crooks, *J. Am. Chem. Soc.*, 2000, **122**, 1243-1244.

25 Z. K. Cui, Y. P. Guo and J. T. Ma, *Int. J. Hydrogen Energy*, 2016, **41**, 1592-1599.

26 I. D. Dragieva, M. SL. Slavcheva and D. T. Buchkov, *J. Less Common Met.*, 1986, **117**, 311-317.

27 J. Y. Shen, Z. Y. Li, Q. J. Yan and Y. Chen, *J. Phys. Chem.*, 1993, **97**, 8504-8511.

28 G. N. Glavee, K. J. Klabunde, C. M. Sorensen and G. C. Hadjipanayis, *Langmuir*, 1994, **10**, 4726-4730.

29 J. E. Holladay, J. F. White, J. J. Bozell and D. Johnson, *Top Value Added Chemicals from Biomass, Volume II: Results of Screening for Potential Candidates from Biorefinery Lignin*, Pacific Northwest National Laboratory (PNNL), Richland, 2007.

30 Y. Wang, J. Yao, H. R. Li, D. S. Su and M. Antonietti, *J. Am. Chem. Soc.*, 2011, **133**, 2362-2365.

31 L. Cheng, Q. G. Dai, H. Li and X. Y. Wang, *Catal. Commun.*, 2014, **57**, 23-28.

32 X. Cui, A. E. Surkus, K. Junge, C. Topf, J. Radnik, C. Kreyenschulte and M. Beller, *Nat. Commun.*, 2016, **7**, DOI: 10.1038/ncomms11326.

33 S. Laurichesse and L. Avérous, *Prog. Polym. Sci.*, 2014, **39**, 1266-1290.

34 V. K. Thakur and M. K. Thakur, *Int. J. Biol. Macromol.*, 2015, **72**, 834-847.

35 M. A. Serio, D. G. Hamblen, J. R. Markham and P. R. Solomon, *Energy Fuels*, 1987, **1**, 138-152.

36 K. R. Squir, P. R. Solomon, R. M. Carangelo and M. B. DiTaranto, *Fuel*, 1986, **65**, 833-843.

37 N. Yan, C. Zhao, P. J. Dyson, C. Wang, L. T. Liu and Y. Kou, *ChemSusChem*, 2008, **1**, 626-629.

38 Y. Ye, Y. Zhang, J. Fan and J. Chang, *Bioresour. Technol.*, 2012, **118**, 648-651.

39 K. Barta, G. R. Warner, E. S. Beach and P. T. Anastas, *Green Chem.*, 2014, **15**, 191-196.

40 D. J. Rensel, S. Rouvimov, M. E. Gin and J. C. Hicks, *J. Catal.*, 2013, **305**, 256-263.

41 J. Zhang, J. Teo, X. Chen, H. Asakura, T. Tanaka, K. Teramura and N. Yan, *ACS Catal.*, 2014, **4**, 1574-1583.

42 A. B. Stiles, *Catalyst Supports and Supported Catalysts: Theoretical and Applied Concepts*, Butterworth, Stoneham, 1987.

43 S. C. Qi, J. I. Hayashi and L. Zhang, *RSC Adv.*, 2016, **6**, 77375-77395.

44 E. J. Baerends and O. V. J. Gritsenko, *Phys. Chem. A*, 1997, **101**, 5383-5403.

45 A. D. Becke, *J. Chem. Phys.*, 2014, **140**, 18A301.

46 A. J. Cohen, P. Mori-Sánchez and W. Yang, *Chem. Rev.*, 2012, **112**, 289-320.

47 M. J. Frisch, G. W. Trucks, H. B. Schlegel, G. E. Scuseria, M. A. Robb, J. R. Cheeseman, et al., *Gaussian 09 Revision E.01.*, Gaussian, Inc., Wallingford, 2013.

48 Y. Zhao and D. G. Truhlar, *Theor. Chem. Account*, 2008, **120**, 215-241.

49 P. J. Hay and W. R. Wadt, *J. Chem. Phys.*, 1985, **82**, 299-310.

50 X. Li and M. J. Frisch, *J. Chem. Theory Comput.*, 2006, **2**, 835-839.

51 J. B. Foresman and Æ. Frisch, *Exploring Chemistry with Electronic Structure Methods, 2nd ed.*, Gaussian, Inc., Pittsburgh, 1996.

52 K. N. Kudin, G. E. Scuseria and E. Cancès, *J. Chem. Phys.*, 2002, **116**, 8255-8261.

53 J. Tomasi, B. Mennucci and R. Cammi, *Chem. Rev.*, 2005, **105**, 2999-3093.

54 J. R. Krenn, *Nature Mater.*, 2003, **2**, 210-211.

55 P. J. Grunthaner, F. J. Grunthaner and A. Madhukar, *J. Vac. Sci. Technol.*, 1982, **20**, 680-683.

56 S. Kasztelan, J. Grimblot, J. P. Bonnelle, E. Payen, H. Toulhoat and Y. Jacquin, *Appl. Catal.*, 1983, **7**, 91-112.

57 M. G. Thube, S. K. Kulkarni, D. Huerta and A. S. Nigavekar, *Phys. Rev. B*, 1986, **34**, 6874-6874.

58 P. Selvam, B. Viswanathan and V. Srinivasan, *J. Electron Spectrosc. Relat. Phemon.*, 1989, **49**, 203-211.

59 A. N. Mansour, *Surf. Sci. Spectra*, 1994, **3**, 231-238.

60 Y. Yoon, R. Rousseau, R. S. Weber, D. Mei and J. A. Lercher, *J. Am. Chem. Soc.*, 2014, **136**, 10287-10298.

61 X. Yang, L. Du, S. Liao, Y. Li and H. Song, *Catal. Commun.*, 2012, **17**, 29-33.

62 J. Tobičík and L. Červeny, *J. Mol. Catal. A: Chemical*, 2003, **194**, 249-254.

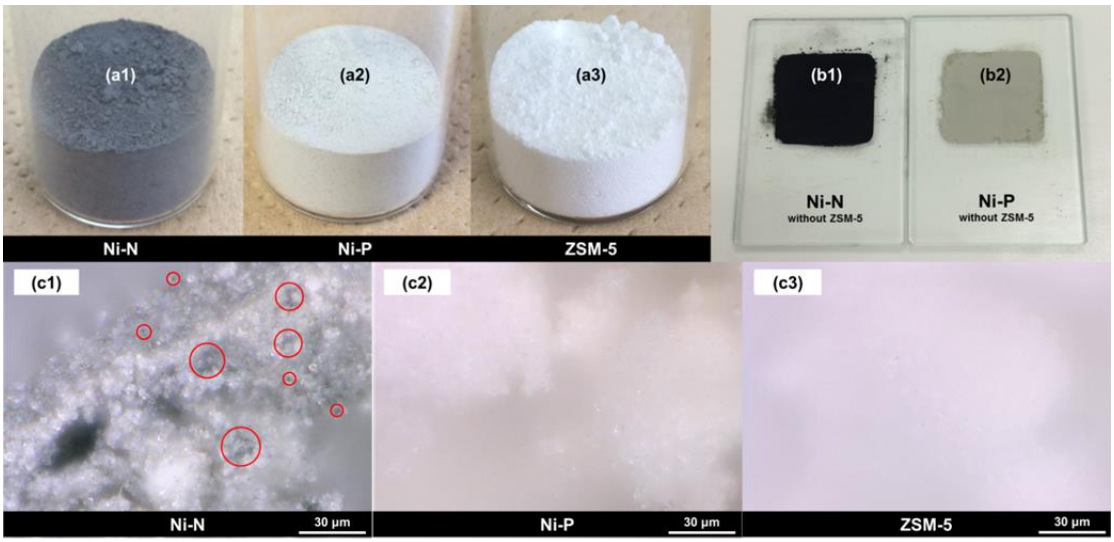

Figure 2-1. Photographs and optical micrographs of the catalysts and support. a1 and c1; Ni-N, a2 and c2; Ni-P, a3 and c3; ZSM-5, b1; Ni prepared by the same procedure as Ni-N but without ZSM-5, b2; Ni prepared by the same procedure as Ni-P but without ZSM-5.

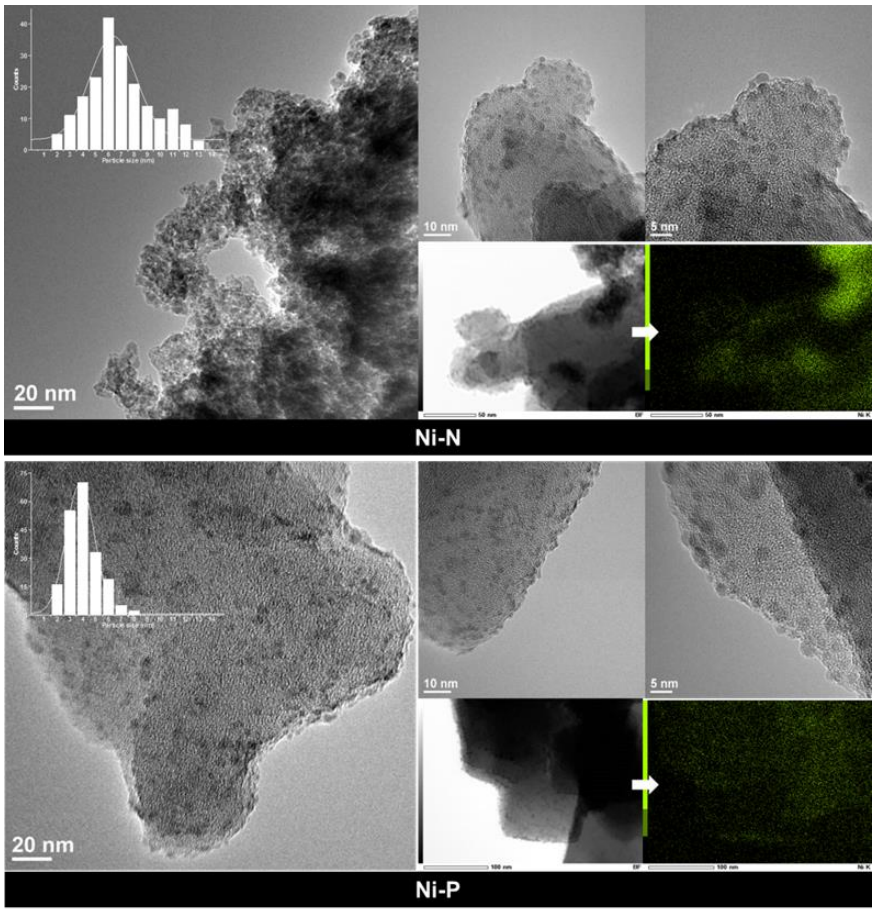

Figure 2-2. TEM images and Ni elemental maps for Ni-N and Ni-P.

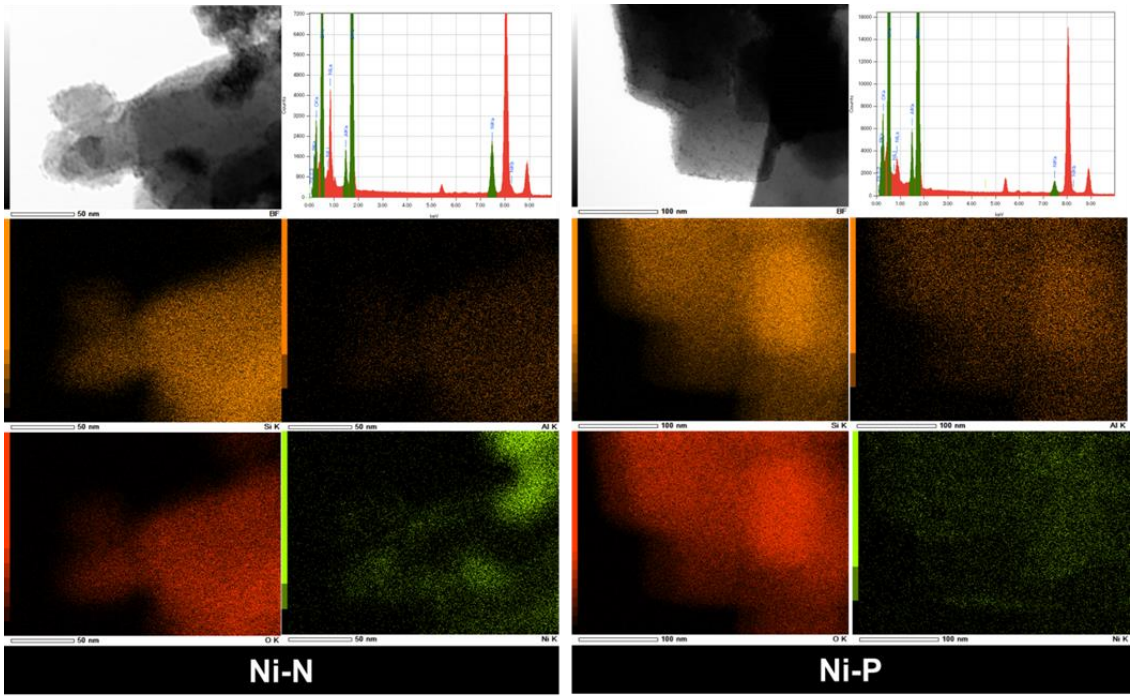

Figure 2-3. EDS spectra for Si, Al, O, and Ni of Ni-N and Ni-P.

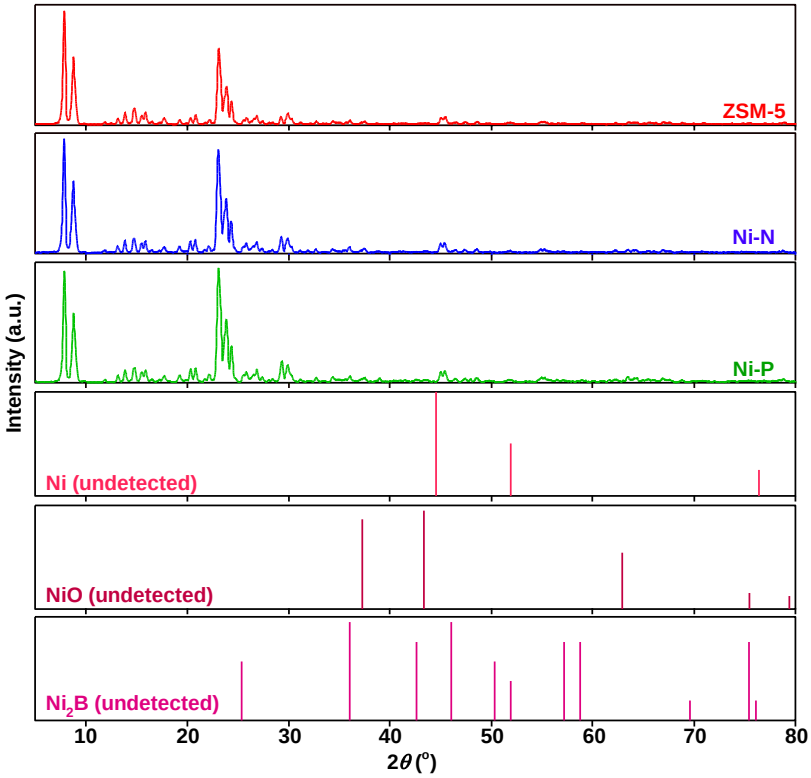

Figure 2-4. X-ray diffraction patterns from ZSM-5, Ni-N, and Ni-P in comparison with those of crystalline Ni, NiO, and Ni_2B.

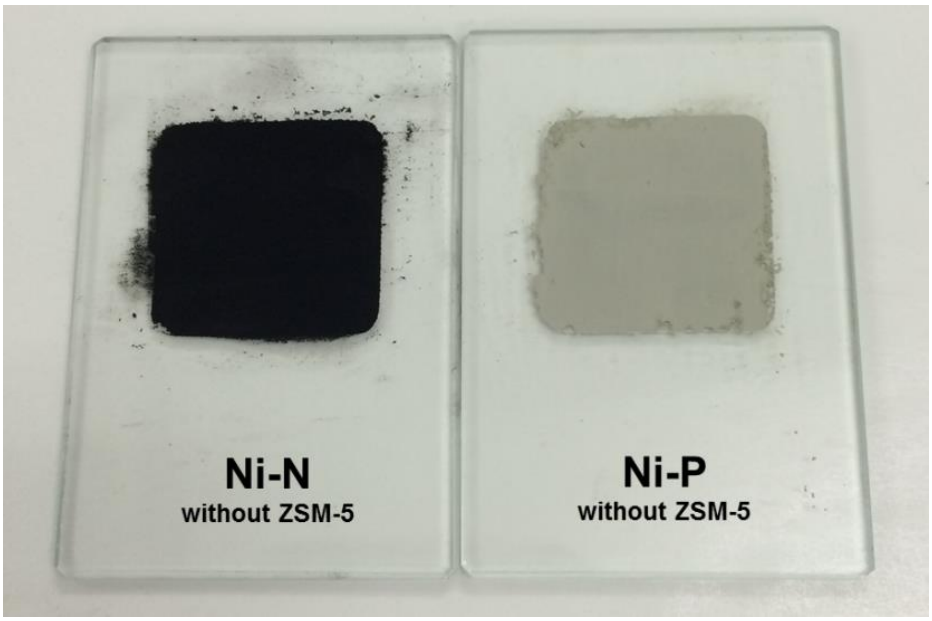

Figure 2-5. Unsupported Ni-N and Ni-P samples for XRD test.

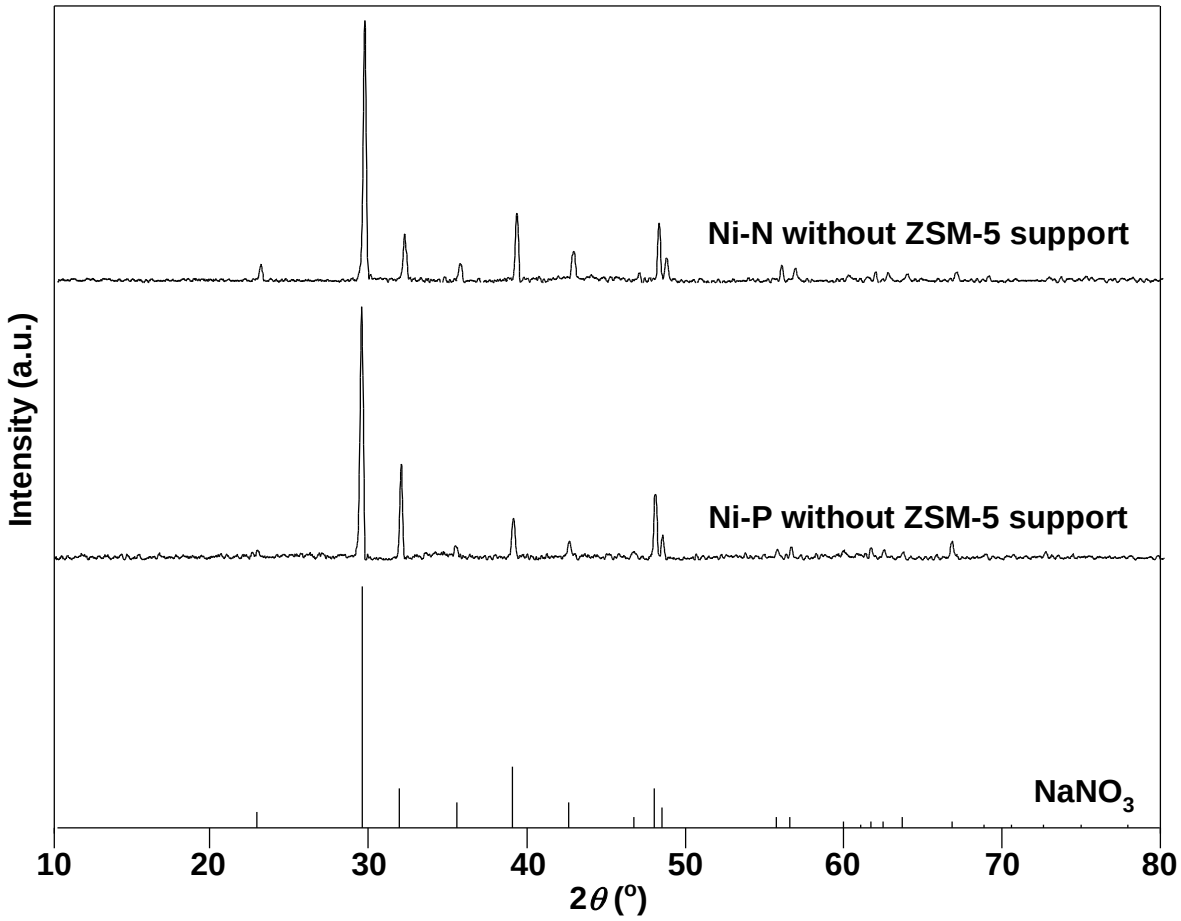

Figure 2-6. XRD patterns of Ni-N and Ni-P without ZSM-5 support (these peaks only indicate the presence of sodium nitrate crystal as the by-product).

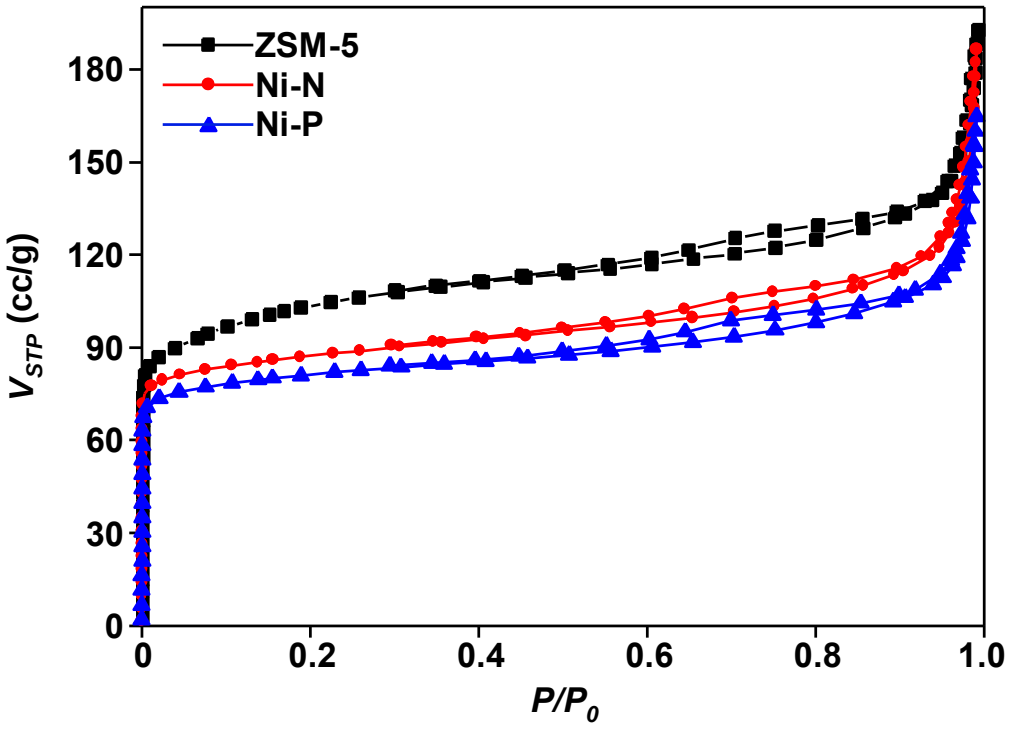

Figure 2-7. N_2 adsorption/desorption isotherms for ZSM-5, Ni-N, and Ni-P.

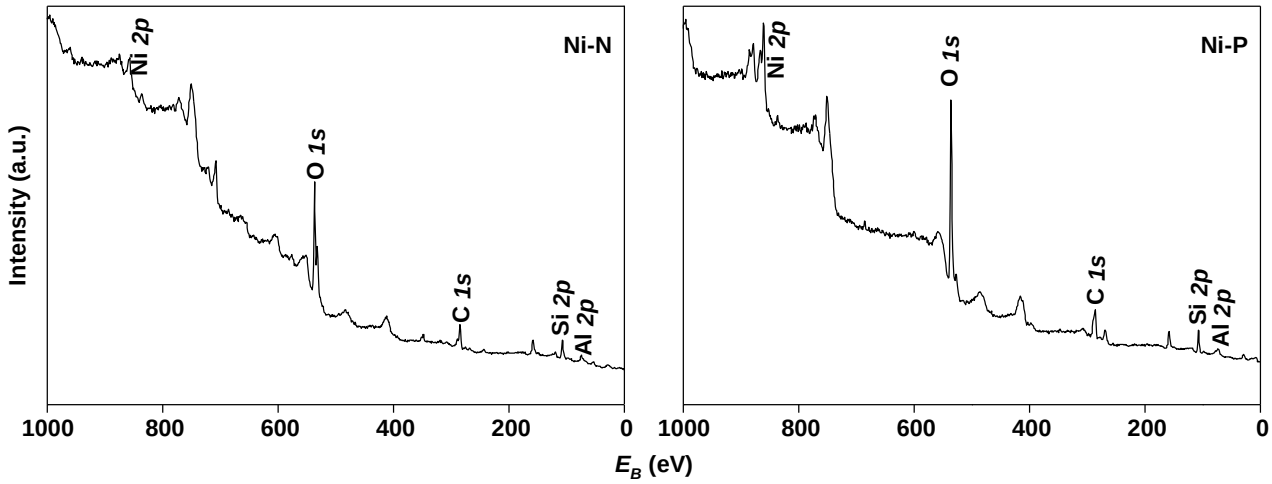

Figure 2-8. XPS spectra of Ni-N and Ni-P (B species are undetected at the E_B range of 186−196 eV).

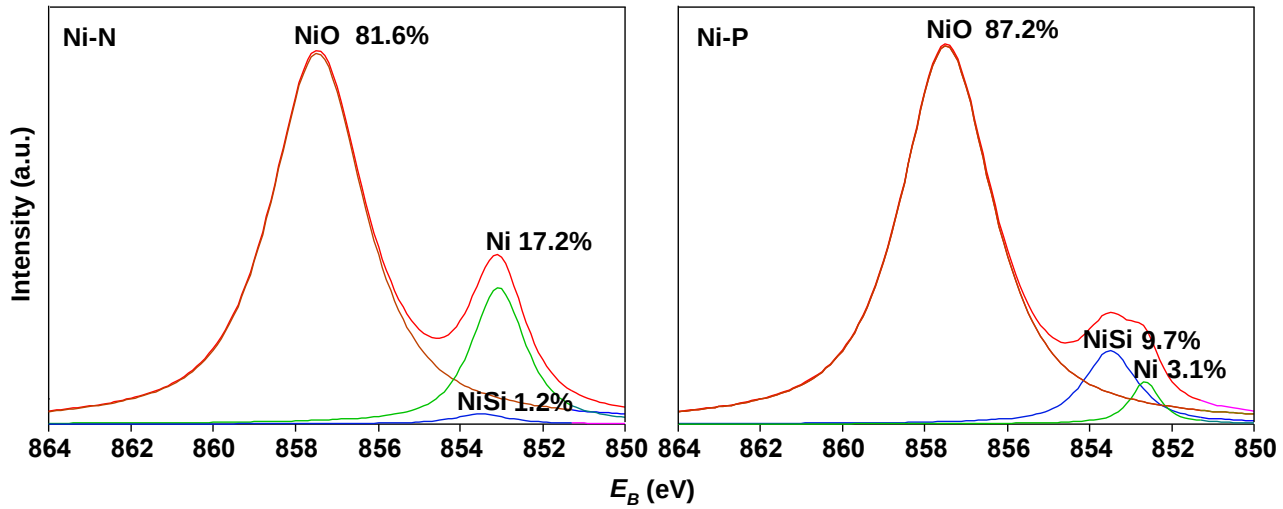

Figure 2-9. XPS spectra of Ni-N and Ni-P in Ni $2p_{3/2}$ regions (red lines). Each spectrum has been deconvoluted into three peaks assigned to NiO (brown line), Ni (green line), and NiSi (blue line).

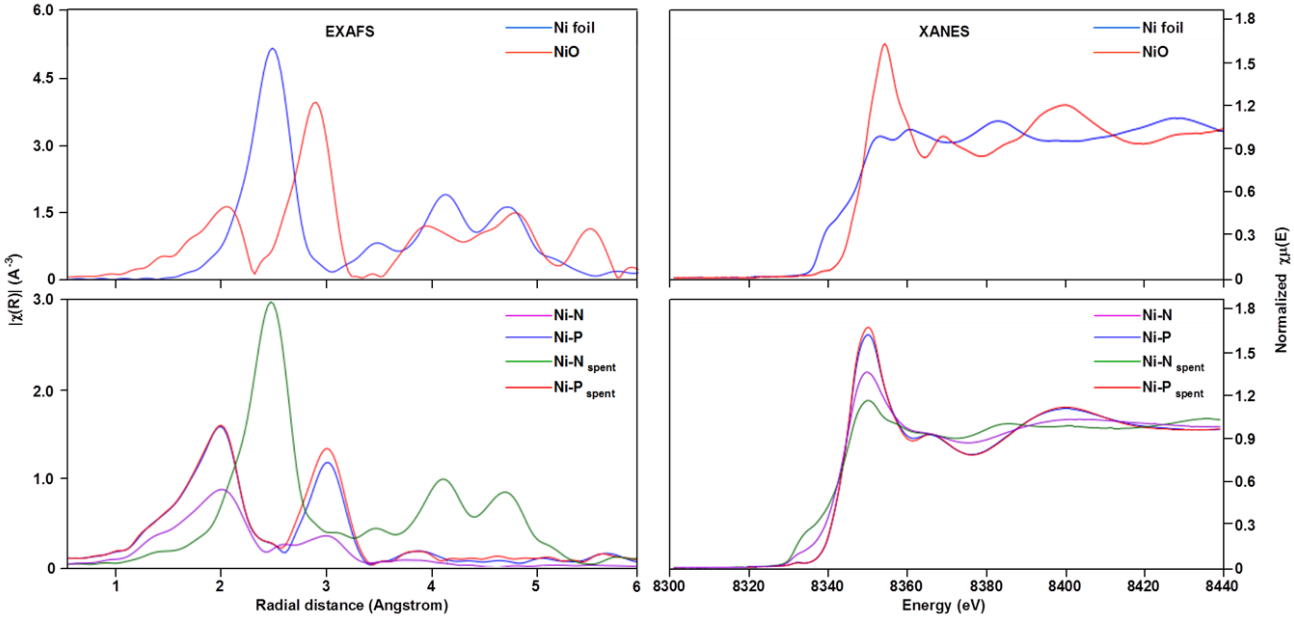

Figure 2-10. EXAFS and XANES spectra of fresh/spent Ni-N and Ni-P. Ni-N; fresh Ni-N, Ni-P; fresh Ni-P, Ni-N_{spent}; spent Ni-N, Ni-P_{spent}; spent Ni-P.

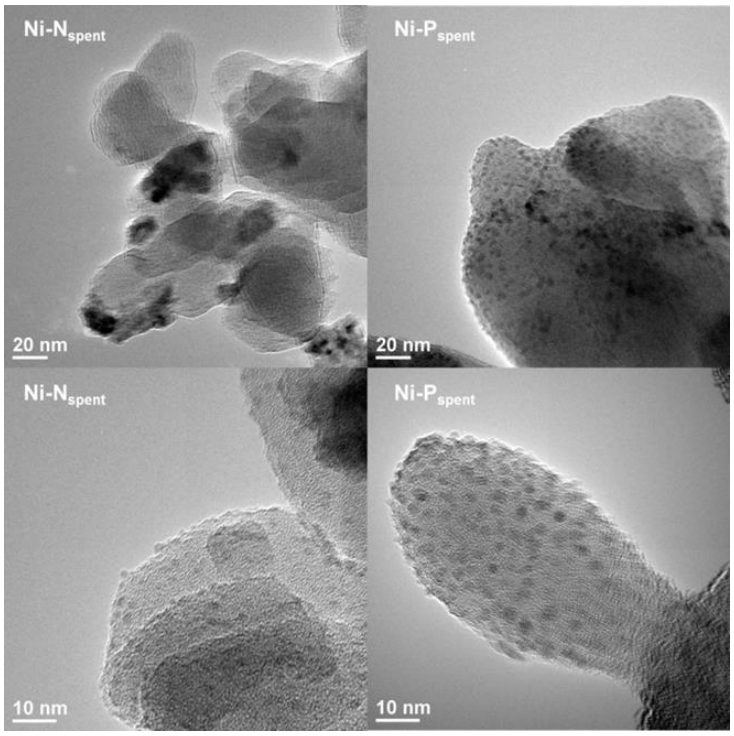

Figure 2-11. TEM images for Ni-N$_{spent}$ and Ni-P$_{spent}$.

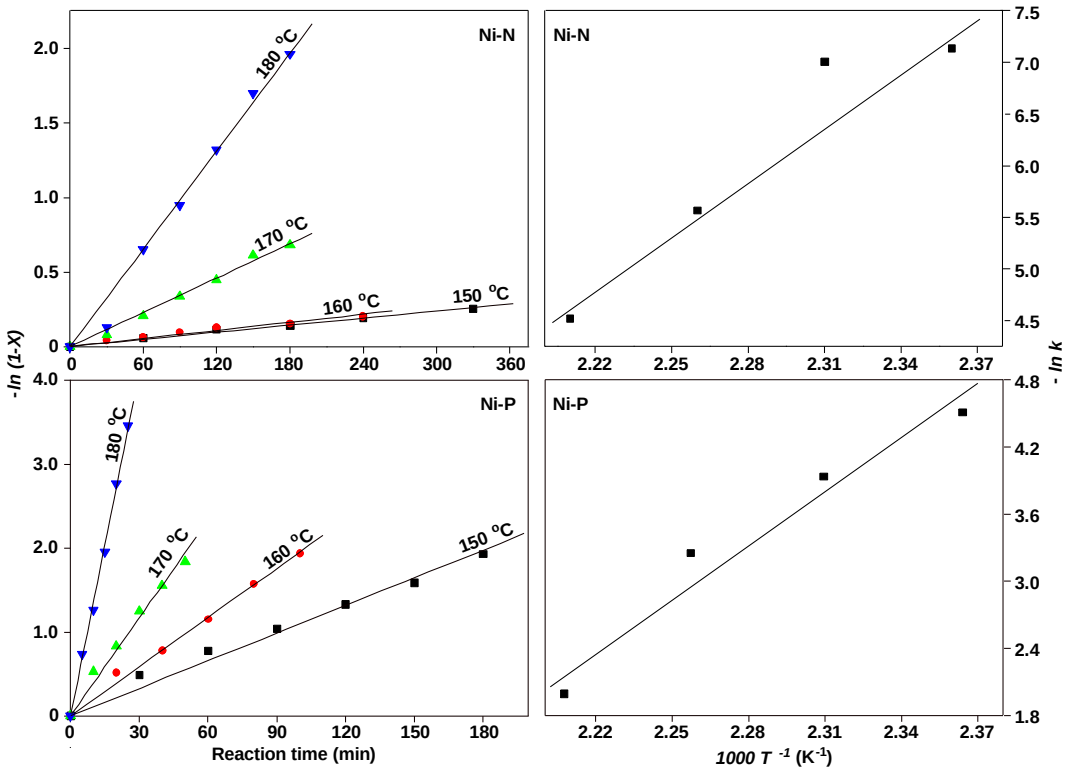

Figure 2-12. Time dependent changes of $ln(1 - X)$ for hydrogenation of phenol over Ni-N and that over Ni-P at 150–180 ℃, and Arrhenius plots of the first-order rate constants.

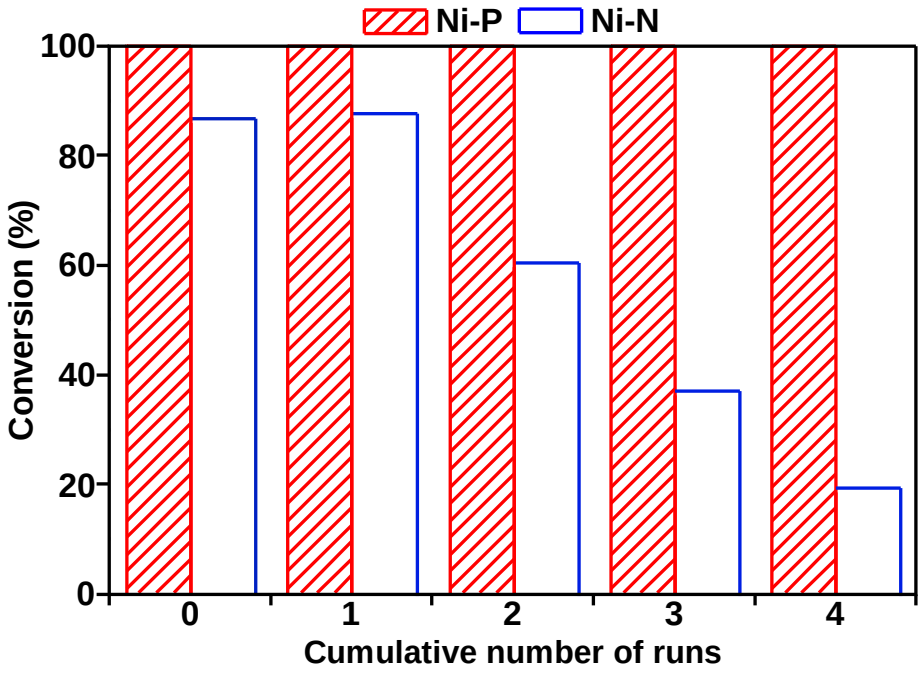

Figure 2-13. Conversions of phenol in repeated runs of hydrogenation of phenol over Ni-N and Ni-P. Temperature and time for each run; 180 ℃ and 3 h, respectively.

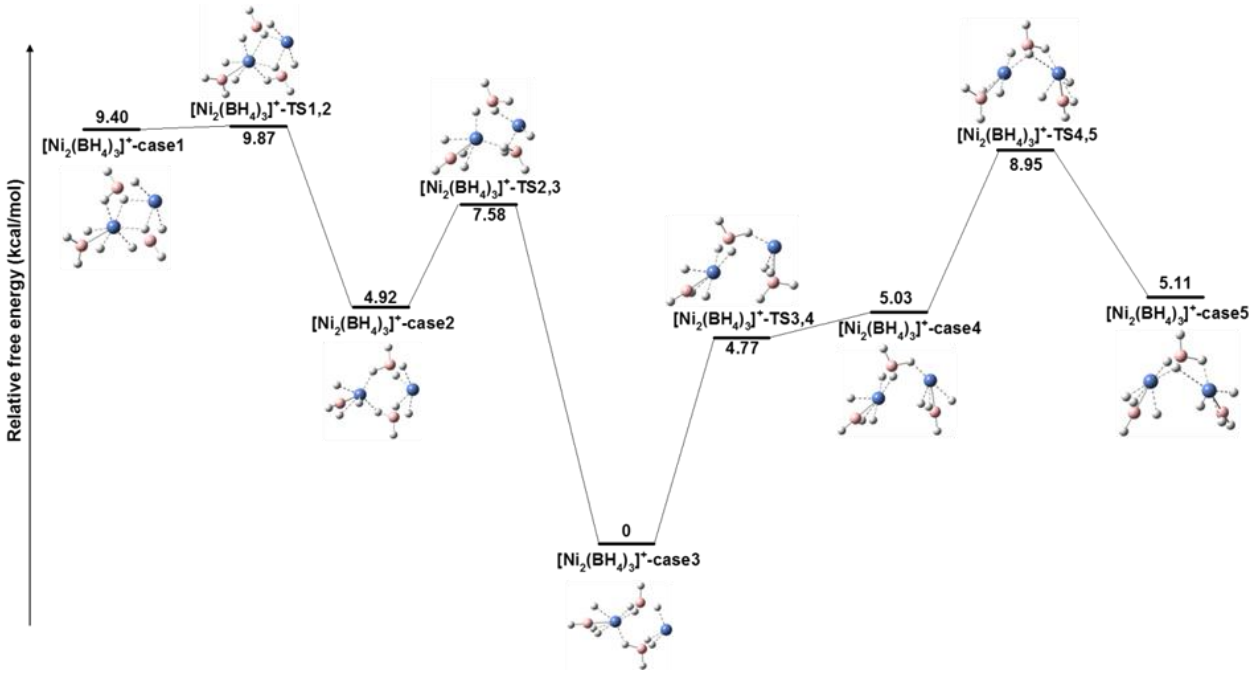

Figure 2-14. Energy and geometry profiles for the transformation from $[Ni_2(BH_4)_3]^+$-Case1 to -Case5.

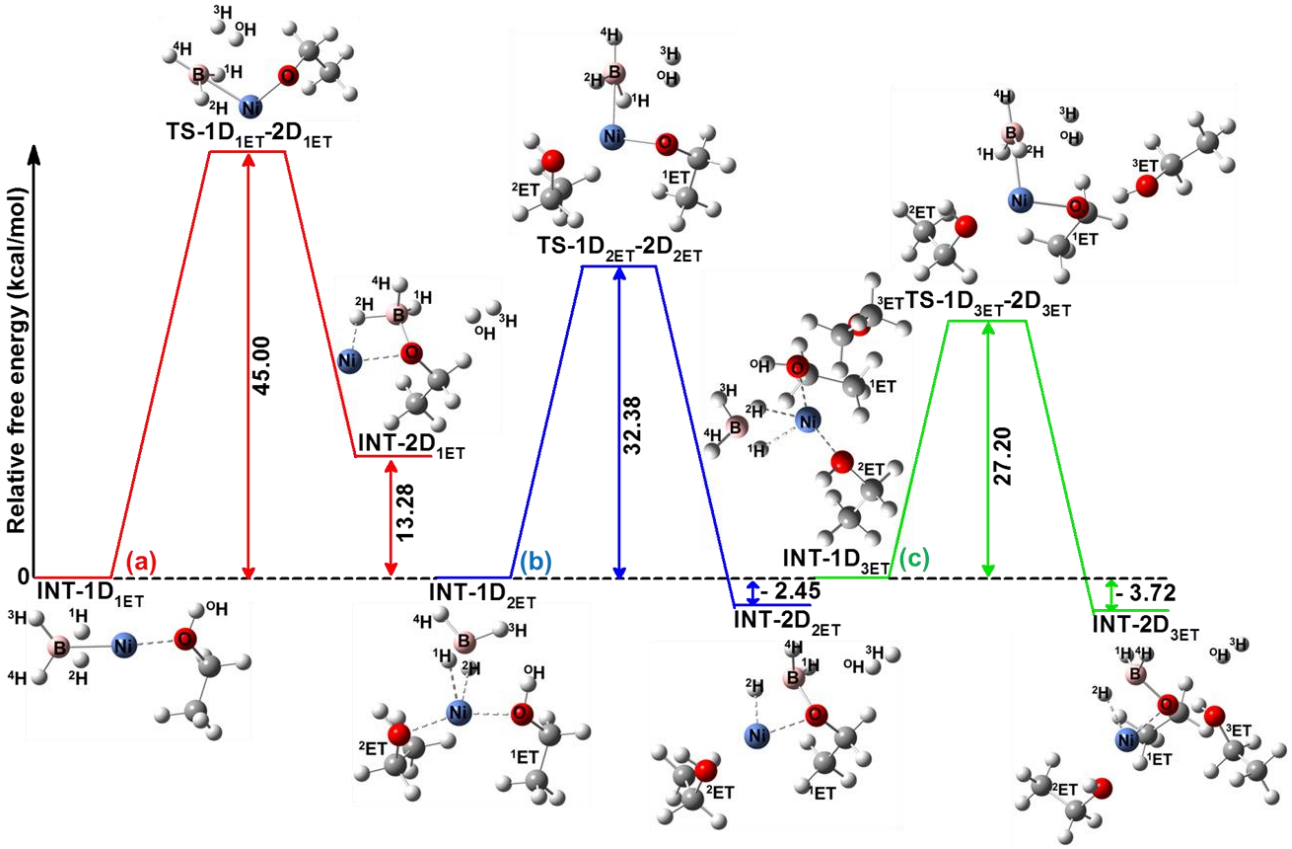

Figure 2-15. Energy and geometry profiles for reaction of $NiBH_4$ with ethanol.

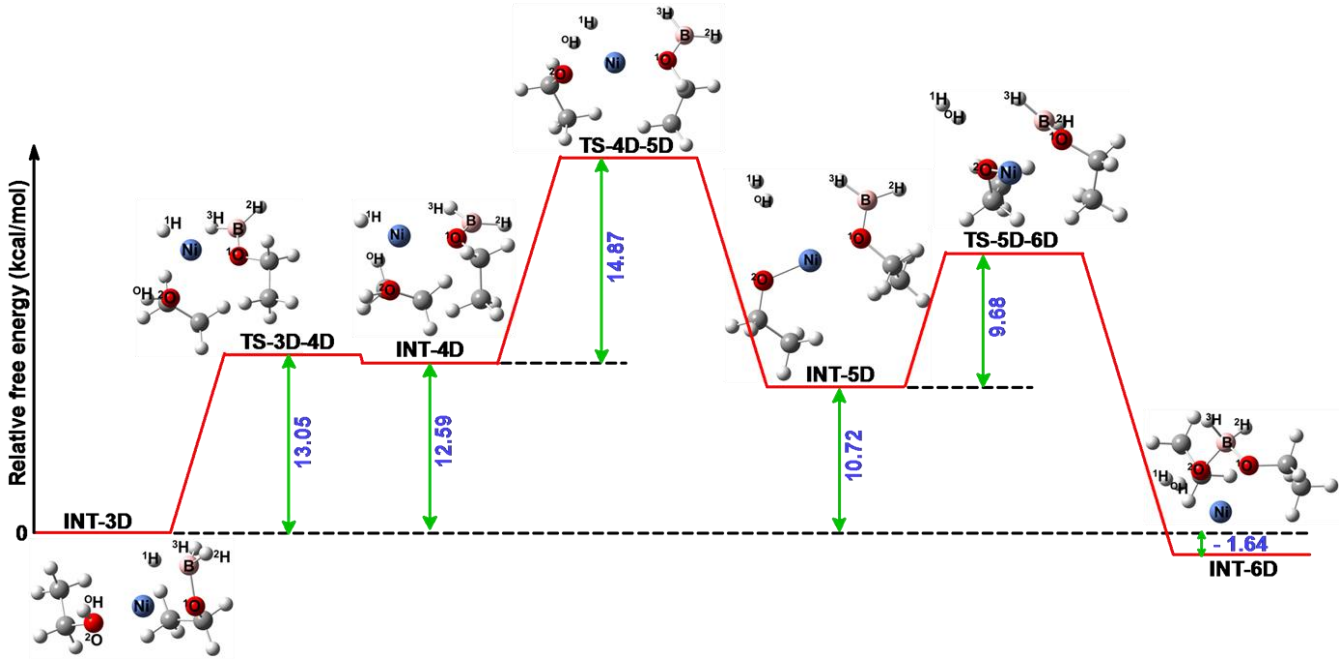

Figure 2-16. Energy and geometry profiles for reaction of $NiBH_3OEt$ with ethanol.

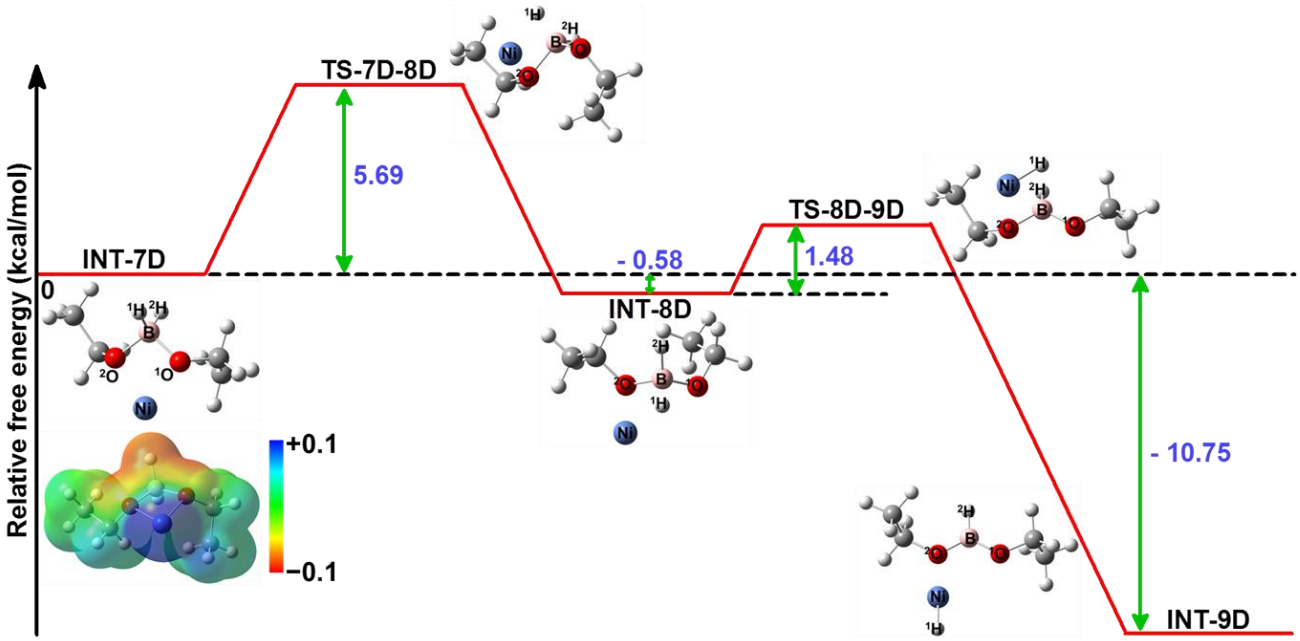

Figure 2-17. Energy and geometry profiles for the decomposition of $NiBH_2(OEt)_2$. The electrostatic potential (a.u.) of $NiBH_2(OEt)_2$ is indicated.

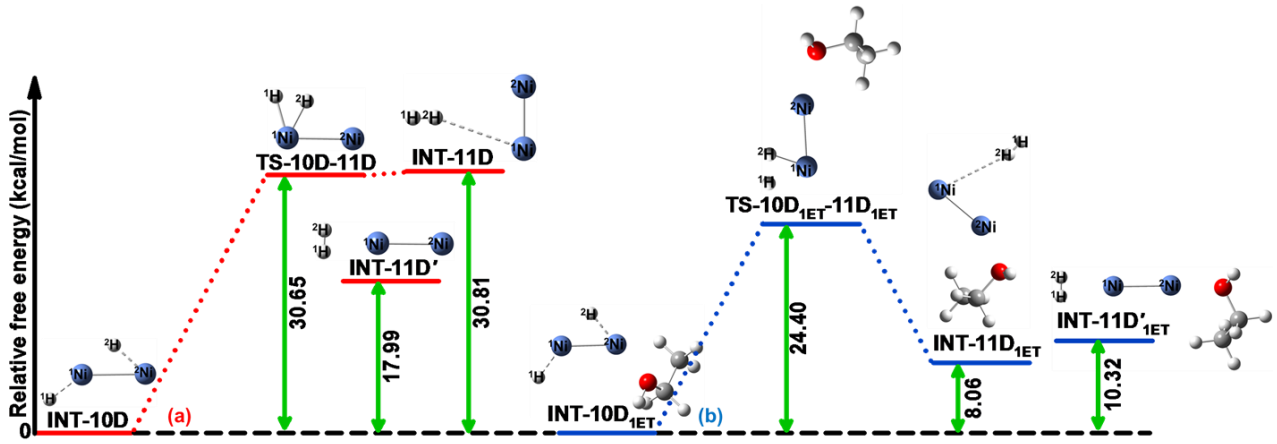

Figure 2-18. Energy and geometry profiles for the dehydrogenation of two NiH molecules.

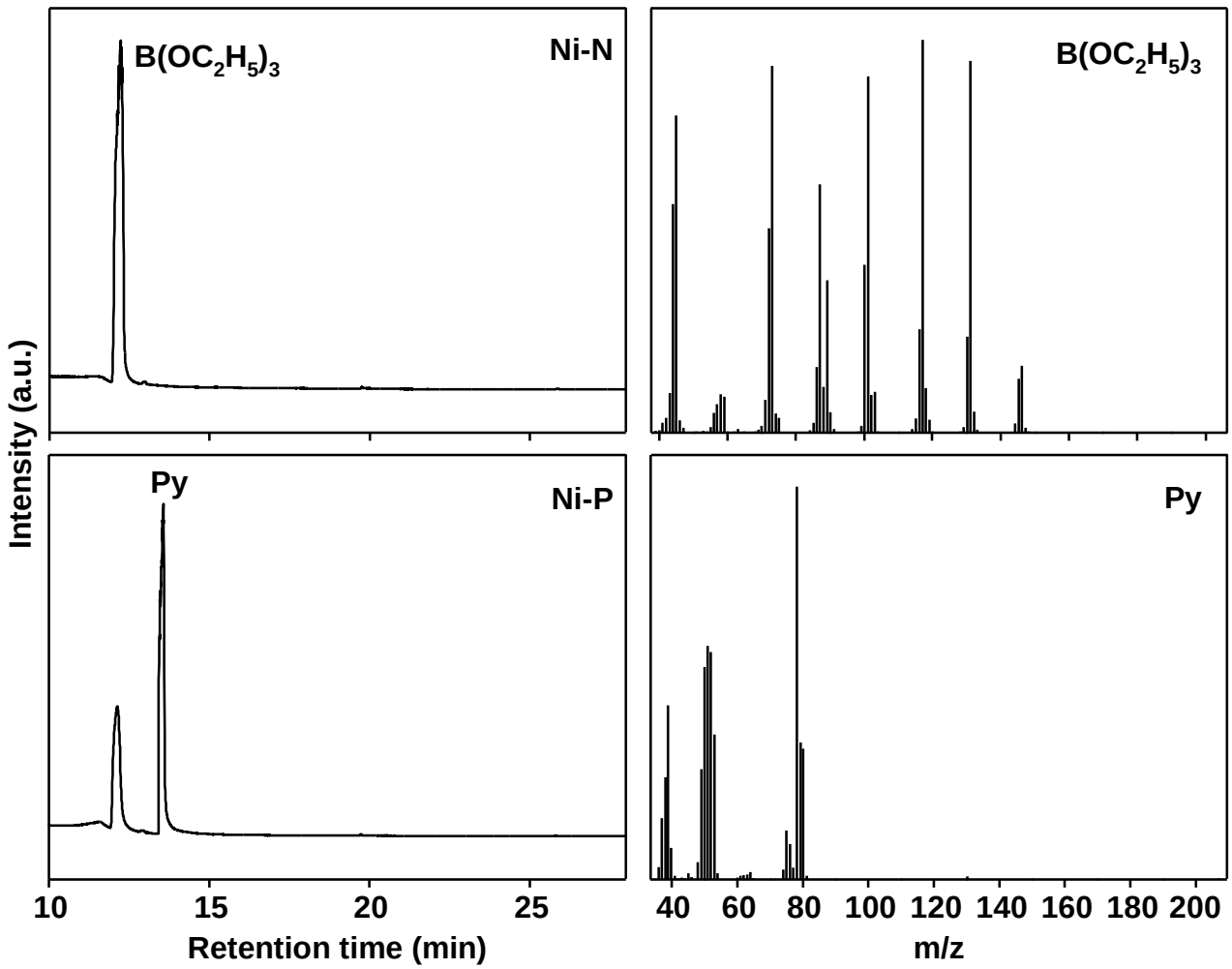

Figure 2-19. The total chromatograms of the filtrates from Ni-N and Ni-P preparation and the mass spectra of $B(OEt)_3$ and Py.

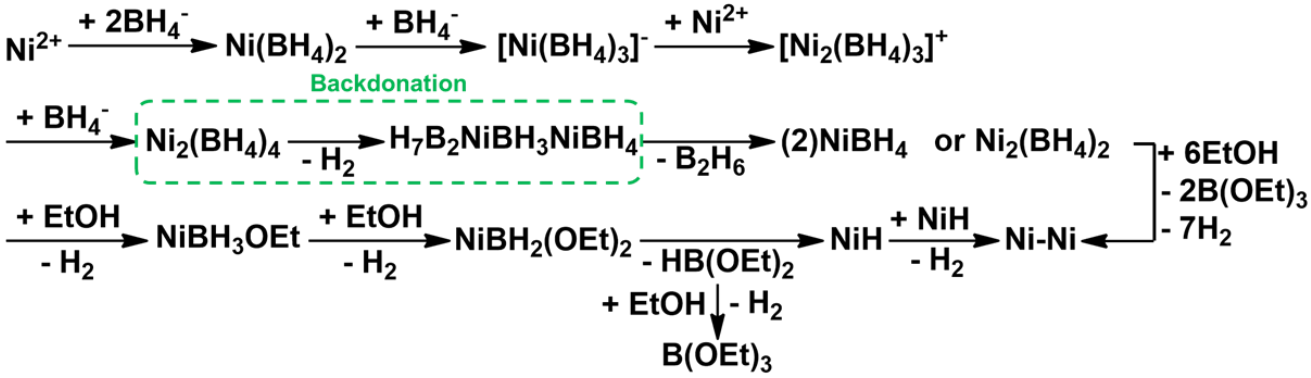

Scheme 2-1. Concise summary of the concluded mechanism for the entire process of Ni^{2+} to Ni^0 reduction by BH_4^- in ethanol.

Table 2-1. Conversion of lignin monomer and product yield by hydrogenation over Ni-N or Ni-P at 180 ℃ for 3 h.

No.	Substrate	Conversion/%		Product	Yield/%	
		Ni-N	Ni-P		Ni-N	Ni-P
1	Phenol	100	100	Cyclohexanol	100	100
2	*p*-Cresol	100	100	*p*-Hexahydrocresol	100	100
3	2,4-Dimethylphenol	70.1	100	2,4-Dimethylcyclohexanol	70.1	100
4	2,3,5-Trimethylphenol	18.8	100	2,3,5-Trimethylcyclohexanol	18.8	100
5	*p*-Propylphenol	96.4	100	*p*-Propylcyclohexanol	96.4	100
6	*o*-Methoxyphenol	59.5	100	*o*-Methoxycyclohexanol	41.4	71.4
				Cyclohexanol	17.1	28.6
				Phenol	1.00	0
7	*o*-Ethoxyphenol	96.7	100	*o*-Ethoxycyclohexanol	93.9	98.4
				Cyclohexanol	2.75	1.63
8	Syringol	46.9	100	2,6-Dimethoxycyclohexanol	16.1	46.7
				2-Methoxycyclohexanol	10.4	33.8
				Cyclohexanol	5.85	19.5
				o-Methoxyphenol	14.6	0
9	Catechol	100	100	Cyclohexane-1,2-diol	100	100
10	Orcinol	100	100	5-Methylcyclohexane-1,3-diol	51.6	66.2
				3-Methylcyclohexanol	48.4	33.8
11	Pyrogallol	100	100	Cyclohexane-1,2,3-triol	53.7	67.8
				Cyclohexane-1,2-diol	46.3	32.2
12	*p*-Hydroxybenzaldehyde	100	100	4-(Hydroxymethyl)cyclohexanol	29.2	36.4
				p-Hexahydrocresol	69.0	62.7
				Cyclohexanol	0.27	0.88
				p-Cresol	1.58	0
13	Vanillin	100	100	2-Methoxy-4-methylcyclohexanol	15.9	51.9
				4-Methylcyclohexanol	9.70	46.4
				2-Methoxy-4-methylphenol	72.1	1.77
				p-Cresol	2.27	0
14	Syringaldehyde	100	100	2,6-Dimethoxy-4-methylcyclohexanol	0.70	26.9
				2-Methoxy-4-methylcyclohexanol	0	21.7
				Cyclohexanol	0	12.8
				Creosol	4.10	8.09
				Syringol	1.11	0
				4-Methylsyringol	94.1	30.5

Table 2-2. Electrostatic potentials of lignin monomers.

No.	Molecular formula	Electrostatic potential	No.	Molecular formula	Electrostatic potential
1	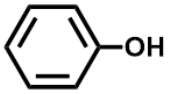	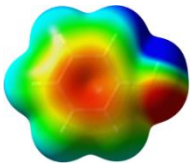	8	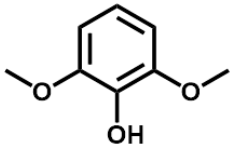	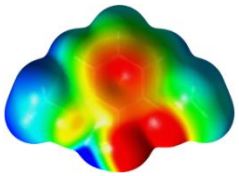
2	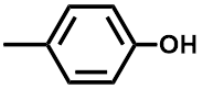	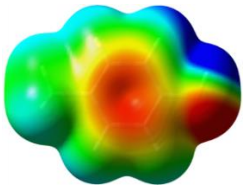	9	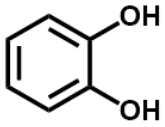	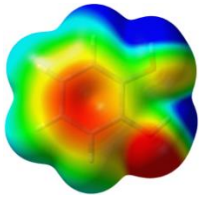
3	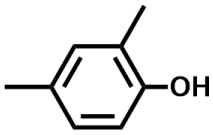	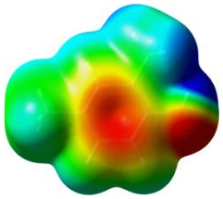	10	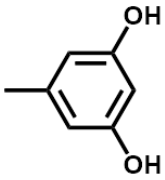	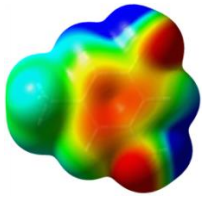
4	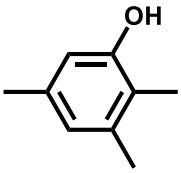	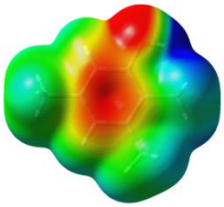	11	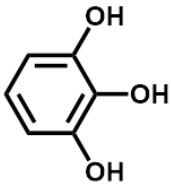	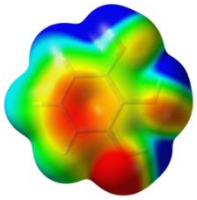
5	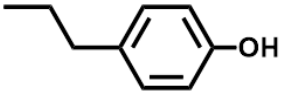	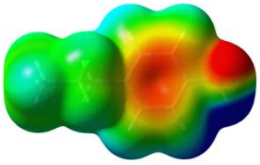	12	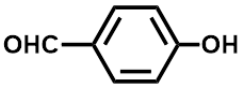	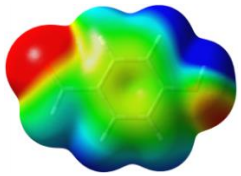
6	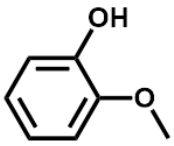	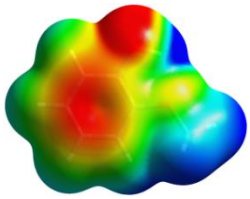	13	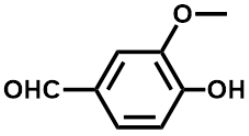	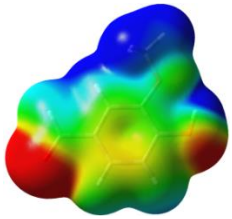
7	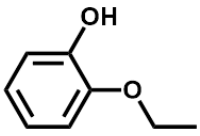	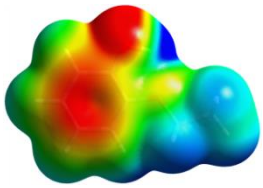	14	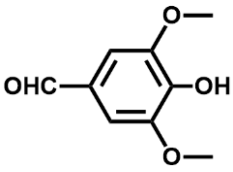	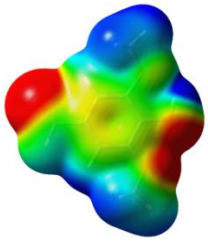

−0.03 (a.u.)  0.03 (a.u.)

Table 2-3. Zero-point energy (E0), EG, and bond lengths of Ni2+, BH4−, and Ni(BH4)2 at different spin states.

Charge	Spin state	Geom.	E_0 (a.u.)	E_G (a.u.)	Bond length (Å)
2	Triplet		−168.942405	−168.959180	--
−1	Singlet	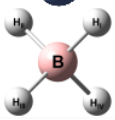	−27.294718	−27.312317	$B\text{-}H_I = B\text{-}H_{II} = B\text{-}H_{III} = B\text{-}H_{IV} = 1.238$
0	Singlet	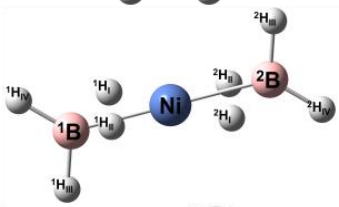	−223.659909	−223.688264	$Ni\text{-}^1B = Ni\text{-}^2B = 2.000$ $Ni\text{-}^1H_I = Ni\text{-}^2H_I = 1.553$ $Ni\text{-}^1H_{II} = Ni\text{-}^2H_{II} = 1.554$ $Ni\text{-}^1H_{III} = Ni\text{-}^2H_{III} = 2.636$
0	Triplet	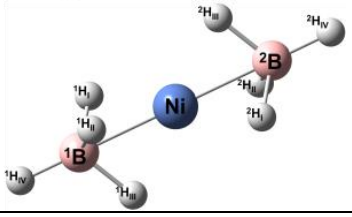	−223.671511	−223.700290	$Ni\text{-}^1B = Ni\text{-}^2B = 1.942$ $Ni\text{-}^1H_I = Ni\text{-}^2H_I = 1.845$ $Ni\text{-}^1H_{II} = Ni\text{-}^2H_{II} = 1.835$ $Ni\text{-}^1H_{III} = Ni\text{-}^2H_{III} = 1.838$

Table 2-4. Examples of geometry-optimized bimolecular $Ni(BH_4)_2$ systems based on collision theory model.

Geom.	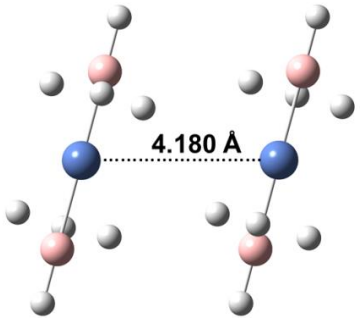	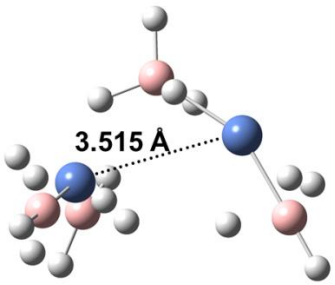	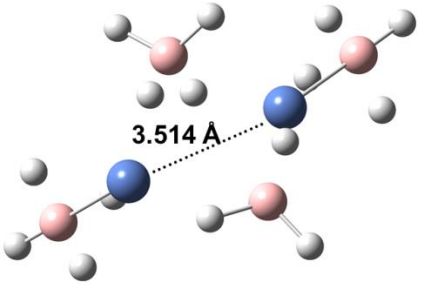
E_G (a.u.)	−447.383666	−447.381584	−447.380782

Table 2-5. Electrostatic potentials, E_0, and E_G of $[Ni(BH_4)_3]^-$ and $[Ni_2(BH_4)_3]^+$s.

Ion	[a] Geom.	Electrostatic potential (a.u.)	Energy (a.u.)
$[Ni(BH_4)_3]^-$	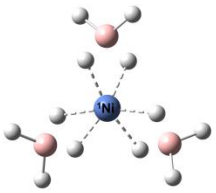	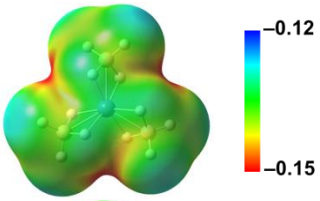	$E_0 = -251.003401$ $E_G = -251.036607$
$[Ni_2(BH_4)_3]^+$-Case1	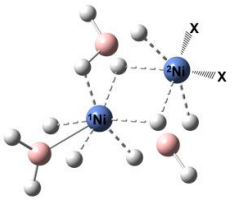	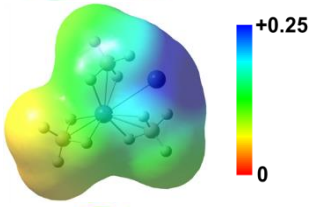	$E_0 = -419.971564$ $E_G = -420.008868$
$[Ni_2(BH_4)_3]^+$-Case2	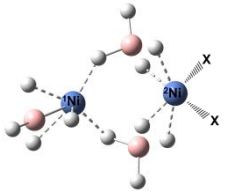	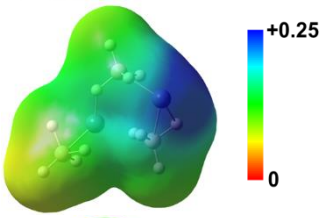	$E_0 = -419.980063$ $E_G = -420.016010$
$[Ni_2(BH_4)_3]^+$-Case3	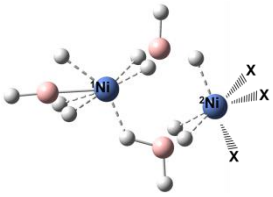	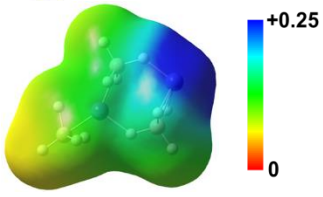	$E_0 = -419.988126$ $E_G = -420.023847$
$[Ni_2(BH_4)_3]^+$-Case4	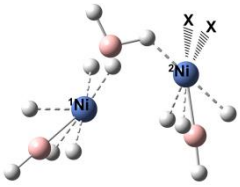	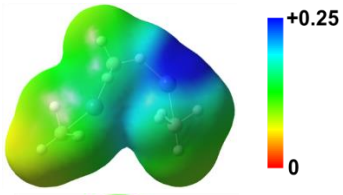	$E_0 = -419.979859$ $E_G = -420.015827$
$[Ni_2(BH_4)_3]^+$-Case5	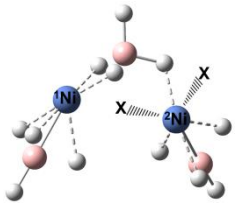	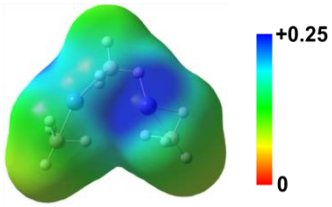	$E_0 = -419.979671$ $E_G = -420.015699$

[a] **X**, the unoccupied coordination site of ^{2}Ni atom.

Table 2-6. INTs and TSs involved in the dehydrogenation process of $Ni_2(BH4)_4$ at quintet spin state.

Acronym	INT-1Q	TS-1Q-2Q	INT-2Q	INT-3Q	H_2
Geom.	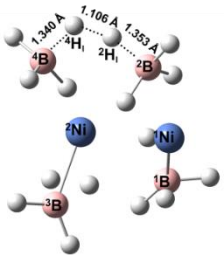	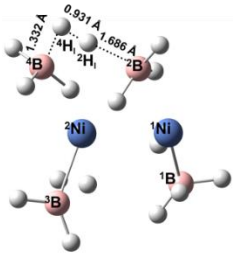	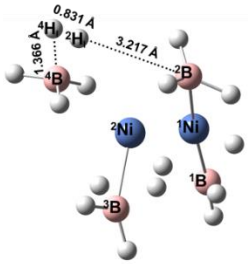	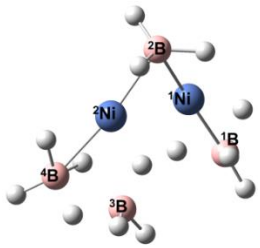	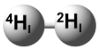
E_0 (a.u.)	−447.285961	−447.282078	−447.311354	−446.170754	−1.159742
E_G (a.u.)	−447.325732	−447.321231	−447.354246	−446.210829	−1.171230

Table 2-7. Population analysis by matching up the α and β orbitals for INT-3Q, TS-3Q-4T, and INT-4T.

Acronym	Geom.	Energy (a.u.)	Occ.	Contributions of atoms
INT-3Q	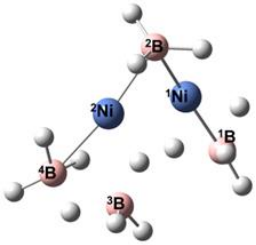	E_0 = −446.170754	$\alpha\beta$	^2Ni_d = 0.66, and ^1Ni_d = 0.24
		E_G = −446.210829	$\alpha\beta$	^2Ni_d = 0.75, and ^1Ni_d = 0.15
			$\alpha\beta$	^1Ni_d = 0.71, ^2Ni_d = 0.13, and ^2B_s = 0.10
			$\alpha\beta$	^2Ni_d = 0.39, and ^1Ni_d = 0.35
			α	^1Ni_d = 0.49, and ^2Ni_d = 0.31
			α	^1Ni_d = 0.77
			α	^2Ni_d = 0.41, ^2B_p = 0.17, and ^2Ni_s = 0.10
			α	^2Ni_d = 0.52, and ^2B_p = 0.19
TS-3Q-4T	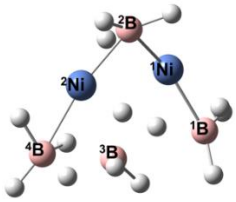	E_0 = −446.197638	$\alpha\beta$	^2Ni_d = 0.67, and ^1Ni_d = 0.25
		E_G = −446.236581	$\alpha\beta$	^2Ni_d = 0.83, and ^1Ni_d = 0.13
			$\alpha\beta$	^1Ni_d = 0.71, and ^2Ni_d = 0.22
			$\alpha\beta$	^1Ni_d = 0.48, and ^2Ni_d = 0.36
			α	^1Ni_d = 0.67, and ^2Ni_d = 0.17
			α	^2Ni_d = 0.69, and ^1Ni_d = 0.17
INT-4T	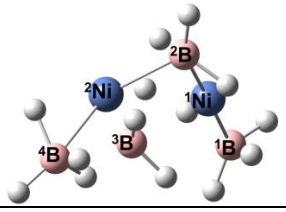	E_0 = −446.208602	$\alpha\beta$	^2Ni_d = 0.36, and ^1Ni_d = 0.36
		E_G = −446.248665	$\alpha\beta$	^1Ni_d = 0.46, and ^2Ni_d = 0.30
			$\alpha\beta$	^1Ni_d = 0.79, and ^2Ni_d = 0.13
			$\alpha\beta$	^2Ni_d = 0.76, and ^1Ni_d = 0.16
			α	^2Ni_d = 0.86
			α	^1Ni_d = 0.81

Table 2-8. Energies and population analysis by matching up the α and β orbitals for INT-2Q and INT-2T.

Acronym	Geom.	Energy (a.u.)	Occ.	Contributions of relevant atoms
INT-2Q	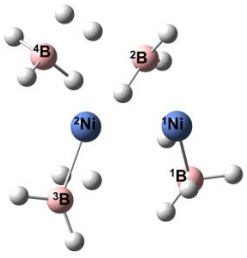	E_0 = −447.311354	$\alpha\beta$	^2Ni_d = 0.52, and ^1Ni_d = 0.25
		E_G = −447.354246	$\alpha\beta$	^2Ni_d = 0.86
			$\alpha\beta$	^1Ni_d = 0.75
			$\alpha\beta$	^2Ni_d = 0.48, and ^1Ni_d = 0.31
			α	^2Ni_d = 0.33, ^2B_p = 0.24, and ^1Ni_s = 0.15
			α	^1Ni_d = 0.75
			α	^2Ni_d = 0.46, and ^1Ni_d = 0.24
			α	^2Ni_d = 0.43, and ^1Ni_d = 0.36
INT-2T	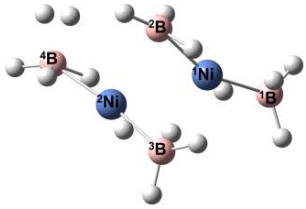	E_0 = −447.358512	$\alpha\beta$	^1Ni_d = 0.48, and ^2Ni_d = 0.17
		E_G = −447.400174	$\alpha\beta$	^1Ni_d = 0.82, and ^2Ni_d = 0.14
			$\alpha\beta$	^2Ni_d = 0.59, and ^1Ni_d = 0.35
			$\alpha\beta$	^1Ni_d = 0.51, and ^2Ni_d = 0.31
			α	^1Ni_d = 0.73
			α	^2Ni_d = 0.74, and ^1Ni_d = 0.12

Table 2-9. Energies of INT-3T and TS-3T-4T leading to INT-4T.

Acronym	INT-3T	TS-3T-4T
Geom.	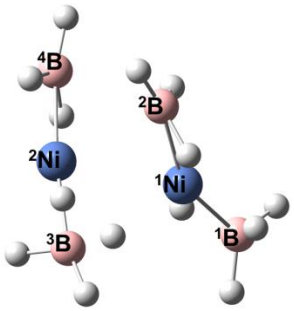	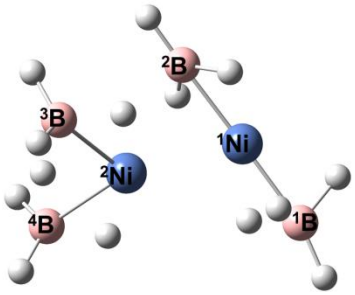
E_0 (a.u.)	−446.193100	−446.194037
E_G (a.u.)	−446.233370	−446.233787

Table 2-10. TS in the decomposition of INT-4T and product.

Acronym	TS-4T-5T	INT-5T	INT-1D	B_2H_6
Geom.	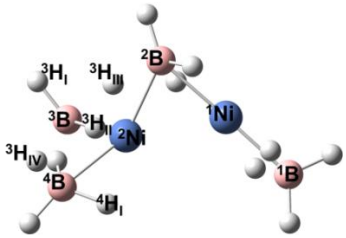	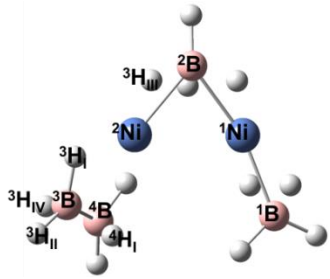	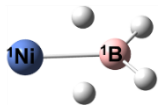	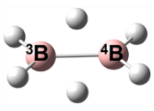
E_0 (a.u.)	−446.208413	−446.242315	−196.504638	−53.177729
E_G (a.u.)	−446.248812	−446.281903	−196.530517	−53.200845

Table 2-11. Population analysis by matching up the α and β orbitals for $NiBH_4$.

Geom.	Occ.	Contributions of relevant atoms
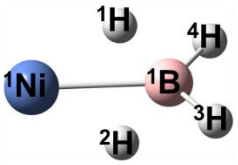	$\alpha\beta$	$^1Ni_d = 1.00$
	$\alpha\beta$	$^1Ni_d = 0.98$
	$\alpha\beta$	$^1B_p = 0.32$, $^1H_s = 0.27$, and $^2H_s = 0.27$
	$\alpha\beta$	$^1Ni_d = 0.97$
	$\alpha\beta$	$^1Ni_d = 0.94$
	α	$^1Ni_d = 0.90$

Table 2-12. Population analysis by matching up the α and β orbitals for NiH.

Geom.	Energy (a.u.)	[a] Occ.	Contributions of relevant atoms
	$E_0 = -169.876691$ $E_G = -169.896234$	$\alpha\beta$	$Ni_p = 1.00$
		$\alpha\beta$	$Ni_p = 1.00$
		$\alpha\beta$	$H_s = 0.51$, and $Ni_s = 0.44$
		$\alpha\beta$	$Ni_d = 1.00$
		$\alpha\beta$	$Ni_d = 1.00$
		$\alpha\beta$	$Ni_d = 1.00$
		$\alpha\beta$	$Ni_d = 0.91$
		α	$Ni_d = 1.00$

Table 2-13. E_0s and E_Gs of H_4BNiPy_2 and its potential products HNiPy and H_3BPy.

Acronym	Geom.	Energy (a.u.)
H_4BNiPy_2	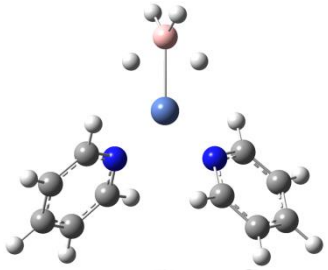	$E_0 = -692.612472$ $E_G = -692.658824$
HNiPy	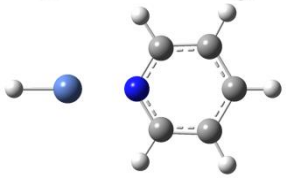	$E_0 = -417.933269$ $E_G = -417.965682$
H_3BPy	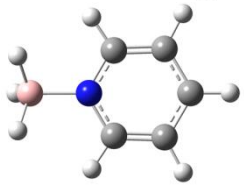	$E_0 = -274.640415$ $E_G = -274.672136$

Chapter 3

Theoretical Study on Hydrogenolytic Cleavage of Inter-monomer Linkages in Lignin

3.1. Introduction

Lignin accounts for almost 30% of the organic part of biomass. In consideration of the predicted depletion of fossil resources and the growing threat from global warming, the utilization of lignin has become a center of interest for worldwide scientists and industries, as the lignin, of which more than half of that carbon is aromatic, provides alternative and attractive new sustainable platforms of fuels, chemicals, and materials [1−3]. Depolymerization is a prerequisite for efficient utilization of lignin because it is a randomly polymerized material forming a complex three-dimensional macromolecular structure. Pyrolysis and hydrogenolysis are two major approaches to the depolymerization of lignin [4−6]. The pyrolysis of lignin is carried out with or without catalyst at temperatures between 450 and 600 ℃, and it produces a mixture of non-condensable gases, liquid, and solid [7]. In contrast to this, the hydrogenolysis is always performed with catalyst and hydrogen donor at temperatures below 350 ℃ to produce depolymerized lignin, phenolic compounds (monomers), and other low molecular-mass compounds, which can be upgraded to hydrocarbon fuels [3].

While knowledge of thermal and catalytic depolymerization of lignin has been accumulated by experimental studies [8−11], theoretical ones still remain elusive even though quantum mechanical calculations can offer fundamental insights into the mechanism of the depolymerization. Theoretical studies on the lignin pyrolysis employ various model molecules, and examine cleavage of diverse linkages assuming free radical mechanisms [12−15]. Huang and co-workers studied thermal cleavage of the β-O-4 linkage of a model dimer, and showed that the major reaction channels consisted of homolytic cleavage of C_β–O bond and subsequent reactions, which were in competition with homolytic cleavage of the C_α–C_β bond. They also investigated the pyrolytic cleavage of α-O-4, β-1, and β-5 phenylcoumaran linkages [16−19]. It was concluded that the homolytic cleavage of C−O bonds were easier than that of C−C bonds, and that the backbone cleavage was easier than that of side chains. Kim *et al.* assessed the cleavage of C–C and C–O linkages involved in diverse model compounds by calculating bond cleavage enthalpies, and results supported those of the kinetic studies by Huang and co-workers [20,21]. The above-mentioned results are credible only for the pyrolysis as the all free radicals are generated from the substrate molecules. The pyrolysis of model molecules forms hydrogen free radicals (H·), which have roles to cap radicals from the cleavage of C−C or C−O bonds terminating the chain reaction [16]. In the calculation, each model molecule is isolated from the others, and then its reactions are self-contained.

The mechanism of lignin hydrogenolysis is much more complex than that of the pyrolysis due to the presence of catalysts and hydrogen donors, which draw various additional factors [22−25]. This feature delivers

two typical results. First, it is difficult for some studies to discuss underlying mechanisms of the lignin hydrogenolysis, especially those in the presence of heterogeneous catalysts. In fact, there have so far been few reports on theoretical studies on the hydrogenolysis since it is difficult to set up a computational model to involve all or comprehensive factors. Second, many reports are unable to explain a general facts that the model molecules such as aryl ethers always undergo hydrogenolysis to high conversion, whereas only a limited portion of the real lignin is converted into monomers and/or oligomers. Still, it is agreed that the addition of hydrogen donors such as H_2 and methanol, which generate active hydrogen species, are crucial in the hydrogenolysis. Ye and co-workers studied the influence of the partial H_2 pressure on mild hydrogenolysis of a lignin, and showed that higher H_2 pressure resulted in higher yield of phenolic compounds [26]. In the presence of metallic catalysts, molecular hydrogen dissociated into H·s on the catalyst surface, and then reacted with lignin [27,28]. Song and co-workers showed that methanol acted as an effective hydrogen donor by easily providing H·s through catalytic dissociation of C−H bonds [29]. It is thus reasonable to set up a computational model based on a hypothesis that H· is a very species directly reacting with lignin molecules while the processes of H· generation from hydrogen donors can be omitted.

It is recognized that inter-aromatic unit linkages of lignin consist of *β*-O-4 ether bonds (45–48%, **Figure 3-1**A), *β*-5 phenylcoumaran bonds (> 12%, **Figure 3-1**B), and minor bonds: diphenyl ether 4-O-5' (**Figure 3-1**C), *β*-1' diphenyl methane (**Figure 3-1**D), and *β*-*β*' pinoresinol bonds (**Figure 3-1**E) [2]. In this work, we focus on the hydrogenolysis of the above-mentioned linkages, while ignoring the substituents per the aromatic ring (see **Figure 3-1**). Employing the five model compounds corresponding to the five types of linkages, we performed the density functional theory (DFT) calculations with the four assumptions as follows: the role of the catalyst was exclusively to produce H·; the hydrogenolysis only occurred between a lignin linkage and the H· in gas phase; the concentration of H· was low enough and steady to guarantee that only one H· reacted always with a lignin linkage; neither the pyrolytic reactions nor chain reactions (after the hydrogenolysis) occurred.

3.2. Computational methods

All DFT calculations were performed by employing a hybrid functional, Boese-Martin for Kinetics (BMK), which has been implemented in the Gaussian 09 package [30]. The BMK functional has very high accuracy in calculation of transition state barriers and also performs well in the calculation of thermodynamic properties [31]. This functional is thus recommended for the exploration of reaction mechanisms. Pople-style basis set 6-31G(d,p) was applied to the H, C, and O atoms [32]. This basis set has been proven to be sufficient for the exploration of reaction mechanisms involving H· [33]. With Grimme's dispersion correction of D3 version (Becke-Johnson damping) [34], fully relaxed geometry optimizations and energetic calculations were performed for all intermediates (INT) and transition states (TS) under tight optimization convergence criteria (root mean square force < 10^{-5}) [35]. Ultrafine numerical integration grids (99 radial shells and 590 angular points per shell) were

employed for all calculations. The vibrational frequencies were calculated at the same basis set levels to identify reactants/products (no imaginary frequency) or a TS (unique imaginary frequency), and to perform zero-point vibrational to energy corrections for accurate thermodynamic data. To check all energy profiles, intrinsic reaction coordinate paths were traced [36]. In addition to the above, self-consistent field procedures of full accuracy were performed with tight convergence (criterion to 10^{-8}) and without any orbital symmetry constraints [37].

With counting 20 K per step, a sufficiently wide temperature range from 298 K to 698 K was investigated since most of the lignin hydrogenolysis has been performed experimentally within this temperature range, according to the above-mentioned references. Free energy change of a reaction was defined as the relative free energy between product and reactant ($\Delta G = G_{\text{product}} - G_{\text{reactant}}$). The free energies at different temperatures were derived from *Gibbs-Helmholtz* equation (Eq. 1). Activation energy was gained by calculation of the relative free energy between the TS and the reactant ($\Delta G^{\neq} = G_{\text{TS}} - G_{\text{reactant}}$). Theoretical reaction rate constant, $k_{TST}(T)$, was calculated according to the transition state theory with Wigner tunnelling corrections $\chi(T)$ (see Eq. 2) [38,39]:

$$\left[\frac{\partial(\Delta G/T)}{\partial T}\right]_p = -\frac{\Delta H}{T^2} \quad \text{(Eq. 1)}$$

$$k_{TST}(T) = \chi(T)\sigma\frac{k_b T}{h}\left(\frac{RT}{p^\theta}\right)^{\Delta n} exp\left[-\frac{\Delta G^{\theta,\neq}(T)}{k_b T}\right],$$

$$\chi(T) = 1 + \frac{1}{24}\left[\frac{h\, lm(\nu^{\neq})}{k_b T}\right]^2 \quad \text{(Eq. 2)}$$

where σ, the reaction channel degeneracy; R, gas constant; p^θ, standard pressure; $\Delta G^{\theta,\neq}(T)$, the standard Gibbs free energy of activation; k_b, the Boltzmann's constant; h, the Planck's constant; Δn = 1 or 0 for gas-phase bimolecular or unimolecular reactions, respectively; $lm(\nu^{\neq})$, the imaginary frequency for TS.

3.3. Results and discussion

All reactions of the inter-aromatic unit linkages with H· were initiated at the weakly bound Van der Waals complexes, which were formed by the approach of H· to the to-be-attacked molecule from infinite distance. The free energy sum of a molecule and an independent H· was hence defined as the energy baseline. It was expected that all effective attacks by H· leaded to bond cleavage and simultaneous formation of another free radical. The subsequent reactions were ignored because there is no energy barrier for the reaction between two free radicals. Such subsequent reactions, as well as those between newly formed free radicals and molecules, were not relative to the antecedent cleavages of the starting model molecule. Thus, the calculation ended at the bond cleavage of the molecule. In addition, the hydrogenation of aromatic rings was not considered because the hydrogenation was much slower than hydrogenolysis of the linkages with homogeneous catalysts [4,8,11,12]. It was also believed that the hydrogenolysis of lignin model compounds was more favored than their hydrogenation also over heterogeneous catalysts [5,25]. In fact, the hydrogenolysis of real lignin always produces aromatics rather than hydroaromatics [24,40−42]. With molecular sizes and the number of the substituents increasing, lignin

macromolecule can be adsorbed onto the heterogeneous catalyst surface only through its negative-potential concentrated linkages and O-containing substituents. The authors considered exclusively the hydrogenolysis of inter-romatic linkages of the lignin model compounds, since the hydrogenolysis of lignin must be preferential than the hydrogenation.

3.3.1. Reaction of Linkage-A (*β*-O-4 ether bond) with H·.

There are eight possible reaction channels for the cleavage of *β*-O-4 ether bond (**Figure 3-2**). H· approaches the molecule from different directions to form various types of reactant complexes. The relative free energies of all these reactant complexes are higher than the energy baseline, and higher temperature generally results in a greater energy gap. This indicates that the independent H· tends to depart from the to-be-attacked molecule, and that the increasing temperature makes the formation of the reactant complexes more difficult. This result is generally gotten in other types of lignin linkage that reacts with H·. This means that, in practice, an ideal catalyst must be active enough to increase the H· concentration as high as possible for enhancing the contact probability of H· to lignin molecules.

All the reactant complexes lead to the cleavage of *β*-O-4 ether bonds directly except A1-I and A8-I. Approaching the *β*-O-4 ether bond from the direction of endmost phenyl group, the H· has to firstly interact with the delocalized π bond of the phenyl group to form A1-I or A8-I. One of the fates of A1-I (A8-I) is to move the weakly bound H· onto the bridgehead C atom of the phenyl group, forming more stable A1-II (A8-II). The energy barriers for this step are only 9.0 kcal/mol for A1-I and 6.7 kcal/mol for A8-I. It is then possible for A1-II and A8-II to cleave their *β*-O-4 ether bonds like other initial reactant complexes. The above reaction channel is also applicable for other linkage types, provided H· attacks the linkage from the direction of endmost phenyl groups.

Different reaction channels result in significant differences in free energy changes. All the reaction channels are thermodynamically favored except Channels 7 and 8, which occur spontaneously only at temperature of 550 K or higher. The energy of each product complex largely depends on the conjugation by the phenyl group. The free radical site far away from the delocalized π bond of the phenyl group results in higher energy of product complex generally. The energy of product containing phenyl free radical is high due to completely disrupted delocalized π bond.

Most of the thermodynamically favored reactions are, however, not favored kinetically. For instance, Channels 4 and 5 are the most favored thermodynamically, but their theoretical rate coefficients are so small (log k_{298K} = –14 and –17 for Channels 4 and 5, respectively) even at elevated temperature that they are inhibited in practice. The activation energy of C–C bond cleavage is generally higher than that of C–O bond cleavage in a similar chemical environment. For example, involved in Channels 5 and 6, the cleavages of aliphatic C–C bonds have rate coefficients smaller than those of aliphatic C–O bonds on Channels 3 and 4 in the entire temperature range from 298 K to 698 K. It is also noted that the rate coefficient for the Ph–C bond cleavage on Channel 8 is smaller than that of the Ph–O bond cleavage on Channel 1 in the entire temperature range. Among the reaction

channels shown in **Figure 3-2**, Channel 1 is deemed to be the most probable, because this channel forms the most stable complex A1-I (5.7 kcal/mol), and causes continuous decrease in the free energy, and has the largest rate coefficient (log k_{298K} = 6.5).

3.3.2. Reaction of Linkage-B (*β*-5 phenylcoumaran bond) with H·.

Linkage-B contains a hydrofuran ring. As seen in **Figure 3-3**, the hydrogenolytic cleavage is that of the hydrofuran ring opening except the case of Channel 6. This channel may be feasible in consideration of the large rate coefficients (log k_{298K} = 0.4) and sequential decrease in the reaction free energy that is negative above temperature as low as 430 K. However, the relative free energy of B6-I (6.1 kcal/mol) is the highest among all of the reactant complexes on Channel 1−6. According to the principle of Boltzmann distribution, this means that the concentration of B6-I is always much lower than other reactant complexes that have lower free energies. Channel 4 and 5 share B4-I but providing different fates. Moving the H· to the bridgehead C atom of Ph−^{1}C bond forms B4-II, which undergoes the opening hydrofuran ring through the cleavage of the Ph−^{1}C bond. On the other hand, moving the H· to the bridgehead C atom of Ph−O bond forms B5-I, which is converted to B5-III by the ring opening through the Ph−O bond cleavage. However, neither Channel 4 nor Channel 5 is feasible because the free energy of their shared reactant B4-I (6.1 kcal/mol) is as high as that of B6-I, and the free energy changes for opening of the hydrofuran rings are positive (ΔG = 9.5 and 2.1 kcal/mol for the formation of B4-III and B5-II, respectively).

With H· directly attacking the hydrofuran ^{2}C–O bond, Channels 1 and 2 are the most favored thermodynamically (ΔG = −26.2 and −37.9 kcal/mol for Channels 1 and 2, respectively) due to the formation of free radicals conjugated with a phenyl group (B1-II and B2-II), and supports our inferences mentioned in Section 3.3.1. There are other possible channels for the hydrofuran ring opening. An example is the cleavage of aliphatic ^{1}C–^{2}C bond, but it can be ignored because the energy barrier for such bond cleavage is generally much higher than that of aliphatic C−O bond and not favored kinetically.

Channels 1 and 3 are most favored in terms of reactant free energies (2.8 kcal/mol) and reaction energy changes (ΔG = −26.2 and −0.3 kcal/mol for Channels 1 and 3, respectively), while the rate coefficients of Channel 1 are much greater than those of Channel 3 (difference by 9 orders of magnitude at 298 K). The superiority of Channel 1 to 3 is, however, not be concluded without considering further reactions of B1-II and B3-II, i.e., the cleavage of the Ph–^{1}C–^{2}C−Ph linkage. Though not shown in **Figure 3-3**, B1-II and B3-II can combine with H· to form 2-(1-hydroxy-3-phenylpropan-2-yl)phenol (referred as β) and 1,2-diphenylpropane-1,3-diol (referred as β*), respectively, while the Ph–^{1}C–^{2}C−Ph linkages are cleft. Conjugation by the phenyl groups still works for stabilizing the free radical products (see **Figure 3-4**). The cleavage of the aliphatic ^{1}C–^{2}C bond on Channels 2 and 4 (ΔG = −26.4 kcal/mol for both Channel 1 and 3) is much more favored thermodynamically than that of Ph−^{1}C or Ph–^{2}C bond on Channels 3 and 6 (ΔG = 11.9 and 6.6 kcal/mol for Channel 3 and 6, respectively). The free energy changes on Channels 3 and 6 are positive in the entire temperature range from 298 K to 698 K that the

cleavages of the Ph–^{1}C and Ph–^{2}C bonds will be inhibited severely, even though their rate coefficients are the largest among the channels in **Figure 3-4**. Moreover, the free energies of β3-I (6.3 kcal/mol) and β6-I (6.2 kcal/mol) are the highest among all the reactants. The cleavage of Linkage-β on Channels 3 and 6 is thus difficult. Among the four channels on which H· directly attacks the Ph–^{1}C–^{2}C–Ph linkage, Channel 4 is the most favored due to its largest free energy change (ΔG = −26.4 kcal/mol), relative low free energy of reactant (4.1 kcal/mol) and low energy barrier (34.3 kcal/mol).

The consideration of the reaction channels shown in **Figures 3-3** and **3-4** leads to recognition of the sequence of Channel 1 (**Figure 3-3**) and Channel 4 (**Figure 3-4**) as the most probable one for the hydrogenolysis of Linkage-B, and that Channel 4 (**Figure 3-4**) is the rate-determining step. This conclusion is supported by the assessment of the cleavage of Linkage-β*, the result of which is shown in **Figure 3-5**. It is shown in **Figure 3-5** that Channel 4 is deemed to be the most favored for the cleavage of Linkage-β*. The sequence of Channel 3 in **Figure 3-3** and Channel 4 in **Figure 3-5** is another candidate for the hydrogenolysis of Linkage-B. However, the energy barrier of its rate-determining step (43.5 kcal/mol) is much higher than that of the other candidate (34.3 kcal/mol, the sequence of Channel 1 in **Figure 3-3** and Channel 4 in **Figure 3-4**). It is thus believed that the channel from Linkage-B to β4-II via B1-II is the main one for the cleavage of Linkage-B.

3.3.3. Reaction of Linkage-C (diphenyl ether) and -D (diphenyl methane) with H·.

Although different hydrogenolysis channels of Linkage-C and -D have almost no impacts on the components of their last products, either of them has two possible reaction channels (see **Figure 3-6**). The relative free energies of C2-I (6.4 kcal/mol) and D2-I (5.9 kcal/mol) are higher than those of C1-I (4.4 kcal/mol) and D1-I (4.7 kcal/mol), respectively, but nonetheless, Channel 2 are favored due to significant kinetic and thermodynamic advantages over Channel 1. The conjugation by the phenyl group plays a vital role for stabilizing the free radical products (C2-III and D2-III), greatly decreasing the energy barriers of the reactions on Channel 2. Compared with the phenyl ether of Linkage-A, the Ph–O bond of Linkage-C will thus be cleft easily with the rate coefficient (log k_{298K} = 7.4) even larger than that of the H· migration on the phenyl groups (log k_{298K} = 6.5). It is also believed that the cleavage of the Ph–C bond of Linkage-D is more favored thermodynamically and kinetically than that of Linkage-β. It is thus suggested that the diphenyl ether and diphenyl methane-type linkages are cleft preferentially respectively to Linkage-A and -B in the hydrogenolysis.

3.3.4. Reaction of Linkage-E (*β–β*' pinoresinol) with H·.

Linkage-E consists of hexahydrofuro[3,4-*c*]furan. The Linkage-E cleavage requires opening the two hydrofuran rings since the cleavages of the two Ph–C bonds is not favored thermodynamically (ΔG = 7.4 kcal/mol, see Channel 5 in **Figure 3-7**). Channel 1 seems to be most favored for opening a hydrofuran ring due to the highest stabilities of E1-I (3.9 kcal/mol) and E1-II (−36.5 kcal/mol), the largest free energy decrease (ΔG = −40.4 kcal/mol), and the greater rate coefficients than Channels 2–4 in the entire temperature range. Therefore, E1-II could be regarded as the absolutely main free radical product.

Combining with a H·, E1-II is converted to (4-benzyl-2-phenyltetrahydrofuran-3-yl)methanol, of which linkage is referred to as Linkage-ε, and then further reacts with H·. As shown in **Figure 3-8**, Channels 3 and 6 that initiate with the H·–phenyl complexes are inhibited thermodynamically (ΔG = 6.8 and 3.5 kcal/mol for Channel 3 and 6, respectively). The rate coefficients for Channels 1 and 4 are greater than those of the other channels for the secondary hydrofuran ring opening. In consideration of the free energies of reactant complexes and free energy changes of the reactions, Channel 1 (relative free energy 1.7 kcal/mol for ε1-I, and ΔG = −23.9 kcal/mol) is deemed to be most favored for the secondary hydrofuran ring opening. The most stable free radical product ε1-II (relative free energy, −22.2 kcal/mol) will act as the main intermediate for the ultimate hydrogenolysis of Ph–^{1}C–^{4}C–^{3}C–^{6}C–Ph linkage which follows the formation of Linkage-e (see **Figure 3-9**) by combination of ε1-II with a H·. Linkage-e (2,3-dibenzylbutane-1,4-diol) is the main product of full opening of the hydrofuran rings of Linkage-E. Both Channels 1 and 2 are more favored thermodynamically and kinetically than other channels for the inter-aromatic C–C bond cleavage, while the free energy of e2-I (6.3 kcal/mol) is much higher than that of e1-I (2.6 kcal/mol). It is then believed that Channel 1 is the main one for the cleavage of Linkage-e.

The hydrogenolytic cleavage of Linakge-E is further assessed here. Note that the advantage of Channel 1 in **Figure 3-7** over Channel 2 is not necessarily distinct. Both the free energy of E2-I (4.9 kcal/mol) and the energy barrier (27.9 kcal/mol) for Channel 2 are higher than those for Channel 1 (3.9 kcal/mol for E1-I, and $\Delta G^{\neq}$ = 27.3 kcal/mol) but only slightly. It is thus necessary to compare Channels 1 and 2 by considering reactions beyond E1-II and E2-II. The results of the assessment are shown in **Figures 3-10** to **3-11**. The combination of E2-II with a H ·forms Linkage-ε*. Among the six channels shown in **Figure 3-10**, Channel 2 seems to be the most favored one. The free radical product at the end of Channel 2, i.e., ε*2-II, will form Linkage-e* by combination with a H·. Linkage-e* will be finally cleavage mainly on Channel 1 in **Figure 3-11**, of which energy barrier (43.1 kcal/mol) is higher than that of Channel 1 in **Figure 3-9** (38.8 kcal/mol). It is thus believed that the cleavage of Linkage-E is most likely to occur in the sequence of Linkage-E, E1-II, ε1-II to e1-II, in which the final step, i.e., the cleavage of ^{1}C–^{4}C linkage is the rate-determining one. However, similar to the case of Linkage-B, the hydrogenolytic cleavage of Linkage-E is difficult because it can also transform into a hydroxymethyl alkylidene linkage after the hydrofuran rings opening. The resulting aliphatic C–C bonds in the long chain will decrease the probabilities of forming the phenyl-conjugated free radicals.

3.3.5. Integrated survey for hydrogenolysis cleavage of lignin.

Based on the above-mentioned discussion, the main reaction channels for the hydrogenolytic cleavages of Linkage-A and -D are abstracted as L + H· ↔ Φ_1 ↔ Φ_2 ↔ Φ_3 (i.e., Linkage-A + H· ↔ A1-I ↔ A1-II ↔ A1-III; Linakge-D + H· ↔ D2-I ↔ D2-II ↔ D2-III). With assumption of the steady concentration of H·, the kinetics for these channels can be expressed as Eq. 3.

Eq. 3 assumes that the step Φ_2 ↔ Φ_3 controls the overall rate of the linkage cleavage due to the smaller rate coefficient than that of antecedent steps. The concentrations of antecedent intermediates are determined by

applying a rapid equilibrium hypothesis [43]. The differential and integral forms of Φ_3 concentration are presented by Eq. 4 as a function of reaction time.

$$L \overset{K_1}{\leftrightarrow} \Phi_1 \overset{K_2}{\leftrightarrow} \Phi_2 \overset{k_3^+/k_3^-}{\longleftrightarrow} \Phi_3 \quad \text{(Eq. 3)}$$

$$\left(\frac{\partial[\Phi_3]}{\partial t}\right)_T = P[\Phi_3] + Q; \text{ or } [\Phi_3]_T = \frac{Q}{P}(e^{Pt} - 1)$$

$$P = -k_3^+\left(\frac{K_1K_2}{1+K_1+K_1K_2} + \frac{1}{K_3}\right); Q = l_0\frac{k_3^+K_1K_2}{1+K_1+K_1K_2} \quad \text{(Eq. 4)}$$

K_i: the equilibrium constant for elementary step i;

k^+_i: the forward rate coefficient for i;

l_0: the initial concentration of L.

The main channel for the cleavage of Linkage-C is expressed by Linakge-C + H· ↔ C2-I ↔ C2-II ↔ C2-III, but the rate-determining step is $\Phi_1 \leftrightarrow \Phi_2$ (Eq. 5). The concentration of Φ_3 is then given by Eq. 6.

$$L \overset{K_1}{\leftrightarrow} \Phi_1 \overset{k_2^+/k_2^-}{\longleftrightarrow} \Phi_2 \overset{K_3}{\leftrightarrow} \Phi_3 \quad \text{(Eq. 5)}$$

$$\left(\frac{\partial[\Phi_3]}{\partial t}\right)_T = P[\Phi_3] + Q; \text{ or } [\Phi_3]_T = \frac{Q}{P}(e^{Pt} - 1)$$

$$P = -k_2^+\left(\frac{K_1+K_1K_3}{1+K_1} + \frac{1}{K_2}\right); Q = l_0\frac{k_2^+K_1K_3}{1+K_1} \quad \text{(Eq. 6)}$$

The cleavage of Linkage-B is presented by Linkage-B + H· ↔ B1-I ↔ B1-II; B1-II + H· → β; β + H· ↔ β4-I ↔ β4-II. B1-II and β can be recognized as the same intermediates because the step B1-II + H· → β is instantaneous and without energy barrier. The entire channel is then simplified to Linkage-B ↔ B1-I ↔ B1-II (β) ↔ β4-I ↔ β4-II as given by Eq. 7. The rate-determining step is $\Phi_3 \leftrightarrow \Phi_4$. The concentration of Φ_4 is given by Eq. 8.

$$L \overset{K_1}{\leftrightarrow} \Phi_1 \overset{K_2}{\leftrightarrow} \Phi_2 \overset{K_3}{\leftrightarrow} \Phi_3 \overset{k_4^+/k_4^-}{\longleftrightarrow} \Phi_4 \quad \text{(Eq. 7)}$$

$$\left(\frac{\partial[\Phi_4]}{\partial t}\right)_T = P[\Phi_4] + Q; \text{ or } [\Phi_4]_T = \frac{Q}{P}(e^{Pt} - 1)$$

$$P = -k_4^+\left(\frac{\prod_{i=1}^{3}K_i}{1+\sum_{j=1}^{3}\prod_{i=1}^{j}K_i} + \frac{1}{K_4}\right); Q = l_0\frac{k_4^+\prod_{i=1}^{3}K_i}{1+\sum_{j=1}^{3}\prod_{i=1}^{j}K_i} \quad \text{(Eq. 8)}$$

The main reaction channel for Linkage-E, which is represented by Linkage-E + H· ↔ E1-I ↔ E1-II; E1-II + H· → ε; ε + H· ↔ ε1-I ↔ ε1-II; ε1-II + H· → e; e + H· ↔ e1-I ↔ e1-II is similar to that of Linkage-B, and it can then be simplified to Linkage-E + H· ↔ E1-I ↔ E1-II (ε) ↔ ε1-I ↔ ε1-II (e) ↔ e1-I ↔ e1-II, as given by Eq. 9. The rate-determining step on this channel is $\Phi_5 \leftrightarrow \Phi_6$. The concentration of Φ_6 is given by Eq. 10.

$$L \overset{K_1}{\leftrightarrow} \Phi_1 \overset{K_2}{\leftrightarrow} \Phi_2 \overset{K_3}{\leftrightarrow} \Phi_3 \overset{K_4}{\leftrightarrow} \Phi_4 \overset{K_5}{\leftrightarrow} \Phi_5 \overset{k_6^+/k_6^-}{\longleftrightarrow} \Phi_6 \quad \text{(Eq. 9)}$$

$$\left(\frac{\partial[\Phi_6]}{\partial t}\right)_T = P[\Phi_6] + Q; \text{ or } [\Phi_6]_T = \frac{Q}{P}(e^{Pt} - 1)$$

$$P = -k_6^+\left(\frac{\prod_{i=1}^{5}K_i}{1+\sum_{j=1}^{5}\prod_{i=1}^{j}K_i} + \frac{1}{K_6}\right); Q = l_0\frac{k_6^+\prod_{i=1}^{5}K_i}{1+\sum_{j=1}^{5}\prod_{i=1}^{j}K_i} \quad \text{(Eq. 10)}$$

Eqs. 3–10 predict the time dependent changes in the conversion of Linkages A–E at temperatures of 298, 358, 418, 478, and 538 K where pyrolytic reactions can be ignored. **Figure 3-12** shows that the cleavage of Linkage-A and that of Linkage-C are extremely rapid due to the presence of their aryl ether bonds, especially for Linkage-C (diphenyl ether 4-O-5'), of which cleavage reaction can be deemed as instantaneous compared with other linkage types. It is noted that the overall rate of Linkage-C cleavage decreases as the temperature increases. This is mainly because the rate-determining step for Linkage-C cleavage, H· migration is next to the formation of reactant complex, and the energy barrier of the rate-determining step is low enough. The elevated temperature has thus severe and negative impacts on the formation of reactant complex, lowering their concentrations and the rates of their reactions.

The cleavage of Linkage-D is slower than those of Linkage-A and -C, but completed within a period << 1 s. It is thus concluded that the diphenyl methane type linkage is also easily broken if it is accessible to H∶ In contrast to Linkage-A, -C and -D, Linkage-B (β-5 phenylcoumaran bond) and -E (β-β' pinoresinol bond) seem to be virtually inert. Even at 538 K, it takes 10^6 s (Linkage-B), 10^7 s (Linkage-E) or longer time to break these linkages. Moreover, in practice, such a long period of time will allow the pyrolytic reactions that lead to cross-linking, repolymerization and then coke formation.

The elevated concentration of H· will accelerate the cleavages of Linkage-A, -C, and -D increasing the concentrations of reactant complexes. Here is defined a pseudo equilibrium constant for the rapid process that forms reactant complex Φ, i.e., $K_{pse} = K[H] = [\Phi]/[L]$, considering the H· concentration as a variable. Conversion of the linkages at 478 K is calculated varying the H· concentration by orders of magnitude. As shown in **Figure 3-13**, the elevated H· concentration significantly increases the rates of cleavages of Linkage-B, -C, and -E while not Linkage-A and -D at all. The rates of cleavages of Linkage -A and -D are both given by Eq.5. When K_2 is much greater than that of K_1 or $K_{1,\,pse}$, the factor P in Eq. 6 hardly changes by perturbation of K_1. On the other hand, the rates of cleavages of Linkage-B, -C, and -E are sensitive to the H· concentration. The efficient cleavage of Linkage-B is expected only when the H· concentration is higher than $100l_0$, while the cleavage of Linkage-E is extremely slow regardless of H· concentration.

Based on the above discussion, the inconsistency between the hydrogenolysis of lignin and that of the model compounds, which was mentioned in the introduction, is explainable. As shown in **Table 3-1** (No. 1 to 5) [4,22,44,45], aryl ethers are the most common model compounds for many of previous experimental studies since it represents a group of dominant linkages in lignin, i.e., β-O-4 ether and diphenyl ether 4-O-5' bonds. High hydrogenolytic conversion of the aryl ethers showed effectiveness of the experimental methods and the activities of the catalysts employed. This study has explored mechanisms of cleavage of those ether linkages. However, the hydrogenolysis of model compounds containing hydrofuran rings, i.e., β-5 phenylcoumaran and β-β' pinoresinol bonds, was dodged in most of the past experimental studies. Our work has shown that the presence of hydrofuran rings limits the depolymerization of actual lignin, and theoretically supports the previous experimental results

shown in **Table 3-1** (No. 6 to 10) [8,24,44,45]. It is hence necessary to investigate behaviors of the hydrofuran linkages under hydrogenolytic conditions in the future. Effective opening of the hydrofuran rings and subsequent cleavage of the resulting linkages is a most critical subject for successful depolymerization of the real lignin.

3.4. Conclusions

The mechanism and kinetics of hydrogenolysis of lignin were studied theoretically by applying density functional theory (DFT). The results of the DFT calculation and the author's consideration have drawn the following conclusions for hydrogenolytic (i.e., H ·-induced) cleavages of the five different types of inter-aromatic linkages that are abundant in the lignin.

Among the five different types of inter-aromatic linkages, Linkage-C (diphenyl ether type) is cleft most rapidly as well as completely as far as H ·radicals are available. The rapidity of the Linkage-A (*β*-O-4 ether type) cleavage follows that of Linkage-C. The cleavage of Linkage-D (diphehyl methane type) is slower by orders of magnitude than those of Linkage-A and -C, but sufficiently fast from a practical point of view. In contrast to the cleavages of Linkage-A, -C, and -D, those of Linkage-B (*β*-5 phenylcoumaran type) and -E (*β*-*β*' pinoresinol type) are extremely slow and difficult. This is arisen from difficulty of complete cleavages of mono- or di-condensed hydrofuranyl rings that connects two aromatic rings. These rings could be opened, but the resulting aliphatic chains hardly undergo cleavage unless H ·radicals are available at high concentration.

It is thus concluded that Linkage-A, -C, and -D can undergo hydrogenolytic breaking under conditions that are considered in this study, i.e., in the temperature range from 418 K to 538 K. These three types of inter-aromatic linkages represent about a half of those involved in lignin. The conclusion explains why the model compounds of lignin such as aryl ethers always undergo high hydrogenolysis conversions, whereas only a limited portion of the real lignin is converted into monomers and/or oligomers. This study is unable to consider all of the possible chain reactions of free radicals, but it is reasonable to expect that most of such chain reactions only benefit retrogressive reactions leading to repolymerization and coking and limiting the depolymerization of lignin.

3.5. References

1 J. Zakzeski, P. C. A. Bruijnincx, A. L. Jongerius and B. M. Weckhuysen, *Chem. Rev.*, 2010, **110**, 3552−3599.

2 C. P. Xu, R. A. D. Arancon, J. Labidi and R. Luque, *Chem. Soc. Rev.*, 2014, **43**, 7485−7500.

3 C. Z. Li, X. C. Zhao, A. Q. Wang, G. W. Huber and T. Zhang, *Chem. Rev.*, 2015, **115**, 11559−11624.

4 A. G. Sergeev, J. D. Webb and J. F. Hartwig, *J. Am. Chem. Soc.*, 2012, **134**, 20226−20229.

5 S. Zhou, Y. Xue, A. Sharma and X. Bai, *ACS Sustain. Chem. Eng.*, 2016, **4**, 6608−6617.

6 F. Liu, Q. Liu, A. Wang and T. Zhang, *ACS Sustain. Chem. Eng.*, 2016, **4**, 3850−3856.

7 H. B. Goyal, D. Seal and R. C. Saxena, *Renew. Sust. Energy Rev.*, 2008, **12**, 504−517.

8 N. Yan, C. Zhao, P. J. Dyson, C. Wang, L. T. Liu and Y. Kou, *ChemSusChem.*, 2008, **1**, 626−629.

9 P. Kelley, S. Lin, G. Edouard, M. W. Day and T. Agapie, *J. Am. Chem. Soc.*, 2012, **134**, 5480−5483.

10 S. Kusumoto and K. Nozaki, *Nat. Commun.*, 2015, **6**, 6296.

11 M. Zaheer and R. Kempe, *ACS Catal.*, 2015, **5**, 1675−1684.

12 J. M. Nichols, L. M. Bishop, R. G. Bergman and J. A. Ellman, *J. Am. Chem. Soc.*, 2010, **132**, 12554−12555.

13 R. Parthasarathi, R. A. Romero, A. Redondo and S. Gnanakaran, *J. Phys. Chem. Lett.*, 2011, **2**, 2660−2666.

14 A. Beste and A. C. Buchanan, *Chem. Phys. Lett.*, 2012, **550**, 19−24.

15 M. Wang, C. Liu, X. Xu and Q. Li, *Chem. Phys. Lett.*, 2016, **654**, 41−45.

16 J. B. Huang, C. Liu, D. Wu, H. Tong and L. R. Ren, *J. Anal. Appl. Pyrolysis*, 2014, **109**, 98−108.

17 J. B. Huang and C. He, *J. Anal. Appl. Pyrolysis*, 2015, **113**, 655−664.

18 J. B. Huang, C. He, C. Liu, H. Tong, L. Q. Wu and S. B. Wu, *Comput. Theor. Chem.*, 2015, **1054**, 80−87.

19 J. B. Huang, C. He, G. Y. Pan and H. Tong, *Comput. Theor. Chem.*, 2016, **1091**, 92−98.

20 S. Kim, S. C. Chmely, M. R. Nimlos, Y. J. Bomble, T. D. Foust, R. S. Paton and G. T. Beckham, *J. Phys. Chem. Lett.*, 2011, **2**, 2846−2852.

21 J. M. Younker, A. Beste and A. C. Buchanan, *ChemPhysChem*, 2011, **12**, 3556−3565.

22 A. G. Sergeev and J. F. Hartwig, *Science*, 2011, **332**, 439−443.

23 J. M. Chan, S. Bauer, H. Sorek, S. Sreekumar, K. Wang and F. D. Toste, *ACS Catal.*, 2013, **3**, 1369−1377.

24 J. Zhang, J. Teo, X. Chen, H. Asakura, T. Tanaka, K. Teramura and N. Yan, *ACS Catal.*, 2014, **4**, 1574−1583.

25 H. Konnerth, J. Zhang, D. Ma, M. H. Prechtl and N. Yan, *Chem. Eng. Sci.*, 2015, **123**, 155−163.

26 Y. Y. Ye, Y. Zhang, J. Fan and J. Chang, *Bioresour. Technol.*, 2012, **118**, 648−651.

27 A. Wu, B. O. Patrick, E. Chung and B. R. James, *Dalton T.*, 2012, **41**, 11093−11106.

28 A. C. Atesin, N. A. Ray, P. C. Stair and T. J. Marks, *J. Am. Chem. Soc.*, 2012, **134**, 14682−14685.

29 Q. Song, F. Wang, J. Cai, Y. Wang, J. Zhang, W. Yu and J. Xu, *Energy Environ. Sci.*, 2013, **6**, 994−1007.

30 M. J. Frisch, G. W. Trucks, H. B. Schlegel, G. E. Scuseria, M. A. Robb, J. R. Cheeseman, G. Scalmani, V. Barone, B. Mennucci, G. A. Petersson, et al. *Gaussian 09*, Revision E.01; Gaussian, Inc.: Wallingford, CT, 2013.

31 A. D. Boese and J. M. Martin, *J. Chem. Phys.*, 2004, **121**, 3405−3416.

32 A. Petersson, A. Bennett, T. G. Tensfeldt, M. A. Al-Laham, W. A. Shirley and J. Mantzaris, *J. Chem. Phys.*, 1988, **89**, 2193−2218.

33 X. Y. Huang, D. G. Cheng, F. Q. Chen and X. L. Zhan, *Bioresour. Technol.*, 2013, **143**, 447−454.

34 S. Grimme, S. Ehrlich and L. Goerigk, *J. Comput. Chem.*, 2011, **32**, 1456−1465.

35 C. Peng, P. Y. Ayala, H. B. Schlegel and M. J. Frisch, *J. Comput. Chem.*, 1996, **17**, 49−56.

36 X. Li and M. J. Frisch, *J. Chem. Theory Comput.*, 2006, **2**, 835−839.

37 K. N. Kudin, G. E. Scuseria and E. A Cances, *J. Chem. Phys.*, 2002, **116**, 8255−8261.

38 D. G. Truhlar, B. C. Garrett and S. J. Klippenstein, *J. Phys. Chem.*, 1996, **100**, 12771−12800.

39 S. Canneaux, F. Bohr and E. Henon, *J. Comput. Chem.*, 2014, **35**, 82−93.

40 Q. Tian, N. Li, J. Liu, M. Wang, J. Deng, J. Zhou and Q. Ma, *Energy Fuels*, 2014, **29**, 255−261.

41 R. Shu, J. Long, Y. Xu, L. Ma, Q. Zhang, T. Wang, C. Wang, Z. Yuan and Q. Wu, *Bioresour. Technol.*, 2016, **200**, 14−22.

42 G. Zhu, X. Ouyang, L. Jiang, Y. Zhu, D. Jin, Y. Pang and X. Qiu, *Fuel Process. Technol.*, 2016, **154**, 132−138.

43 I. Prigogine, *J. Phys. Chem.*, 1951, **55**, 765−774.

44 V. Molinari, C. Giordano, M. Antonietti and D. Esposito, *J. Am. Chem. Soc.*, 2014, **136**, 1758−1761.

45 J. G. Zhang, H. Asakura, J. van Rijn, J. Yang, P. Duchesne, B. Zhang, X. Chen, P. Zhang, M. Saeys and N. Yan, *Green Chem.*, 2014, **16**, 2432−2437.

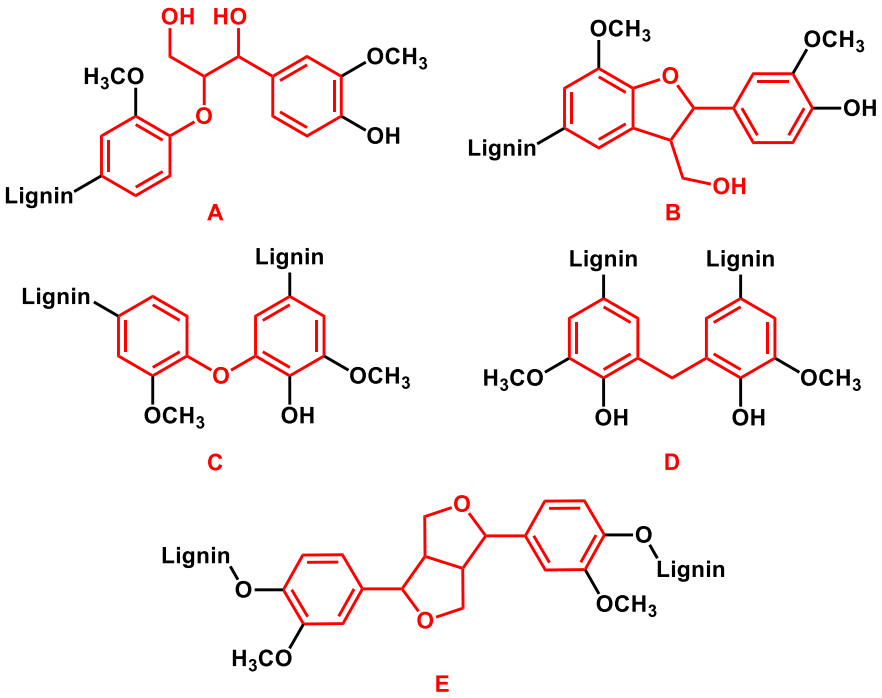

Figure 3-1. Five typical linkages in lignin biopolymer structure and the computational models (red areas).

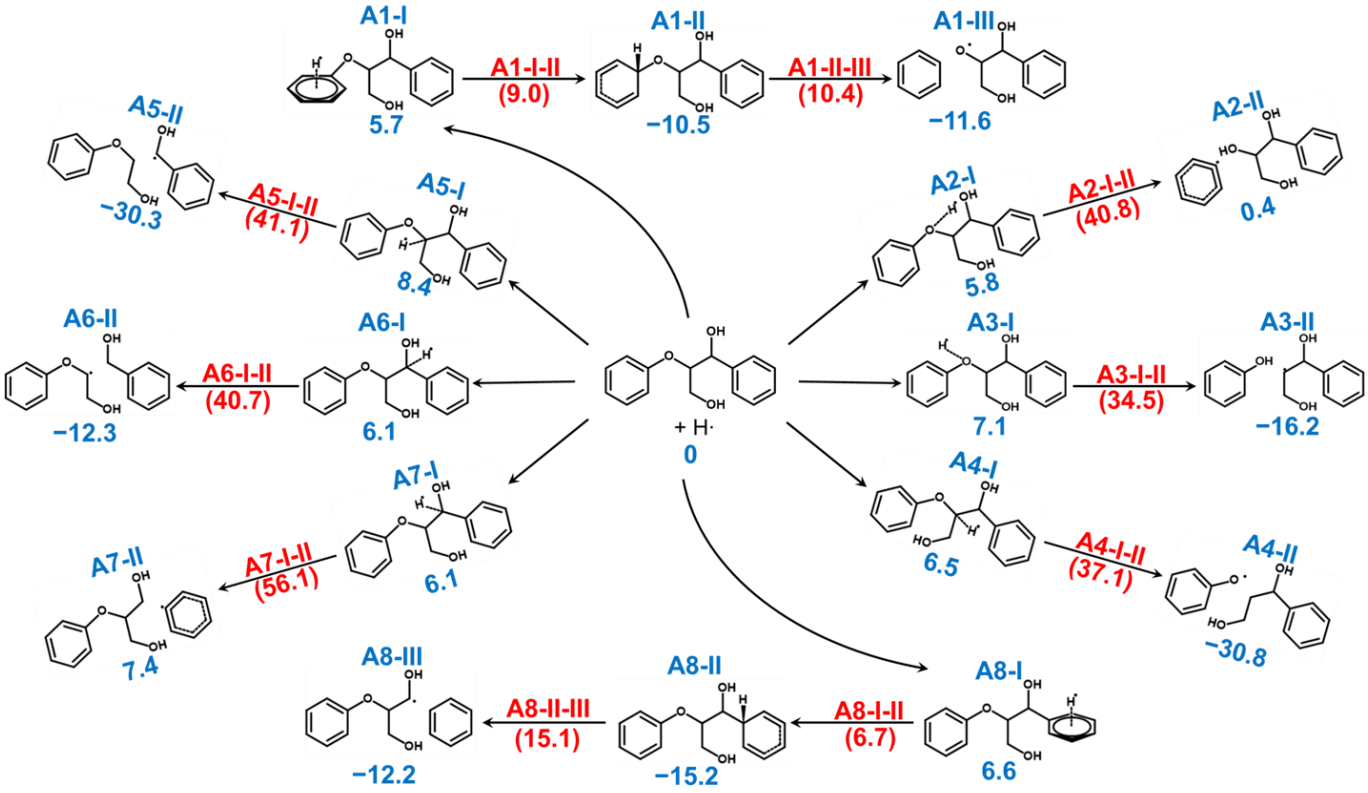

Figure 3-2. Cleavage reaction channels and their energy barriers (in red, kcal/mol) of Linkage-A with H· and the relative free energies (in blue, kcal/mol) of INTs at 298 K, 1 bar.

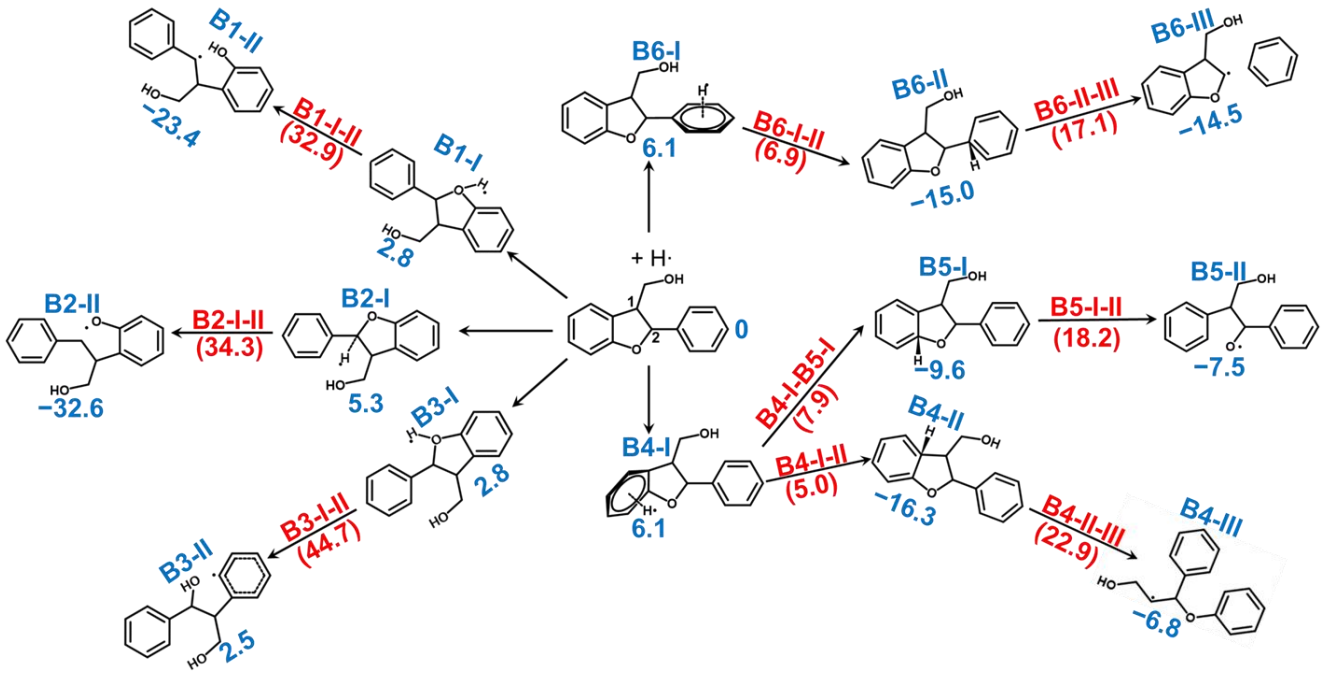

Figure 3-3. Cleavage reaction channels and their energy barriers (in red, kcal/mol) of Linkage-B with H· and the relative free energies (in blue, kcal/mol) of INTs at 298 K, 1 bar.

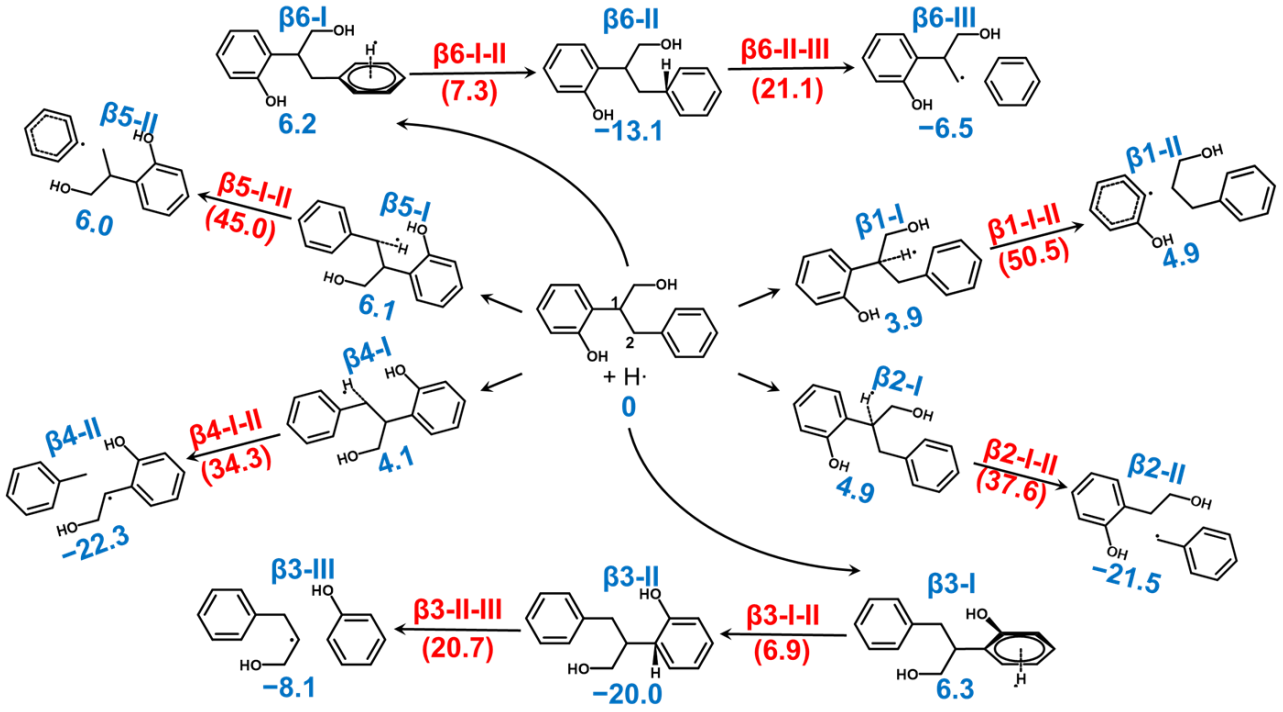

Figure 3-4. Cleavage reaction channels and their energy barriers (in red, kcal/mol) of Linkage-β with H· and the relative free energies (in blue, kcal/mol) of INTs at 298 K, 1 bar.

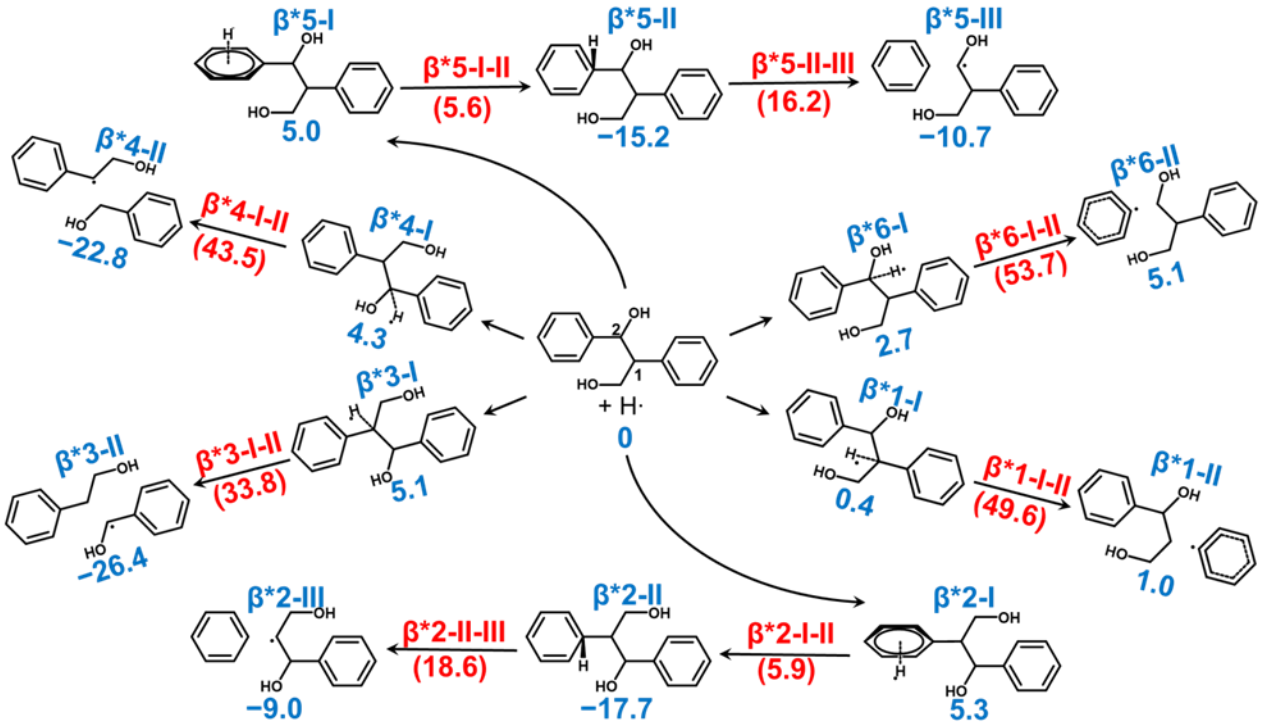

Figure 3-5. Cleavage reaction channels and their energy barriers (in red, kcal/mol) of Linkage-β* with H· and the relative free energies (in blue, kcal/mol) of INTs at 298 K, 1 bar.

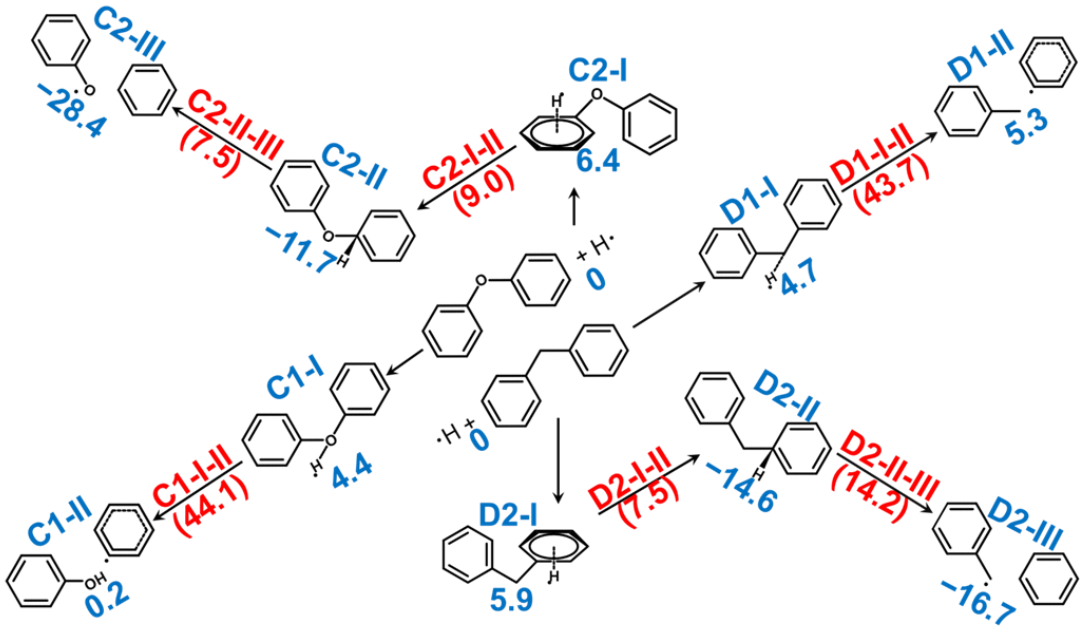

Figure 3-6. Cleavage reaction channels and their energy barriers (in red, kcal/mol) of Linkage-C and -D with H· and the relative free energies (in blue, kcal/mol) of INTs at 298 K, 1 bar.

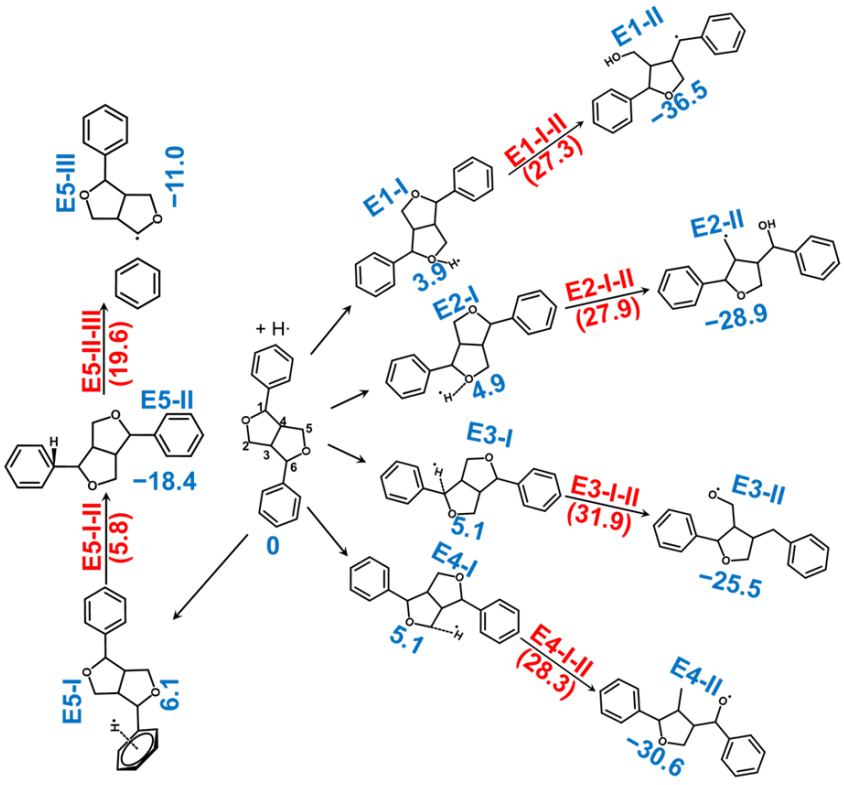

Figure 3-7. Cleavage reaction channels and their energy barriers (in red, kcal/mol) of Linkage-E with H· and the relative free energies (in blue, kcal/mol) of INTs at 298 K, 1 bar.

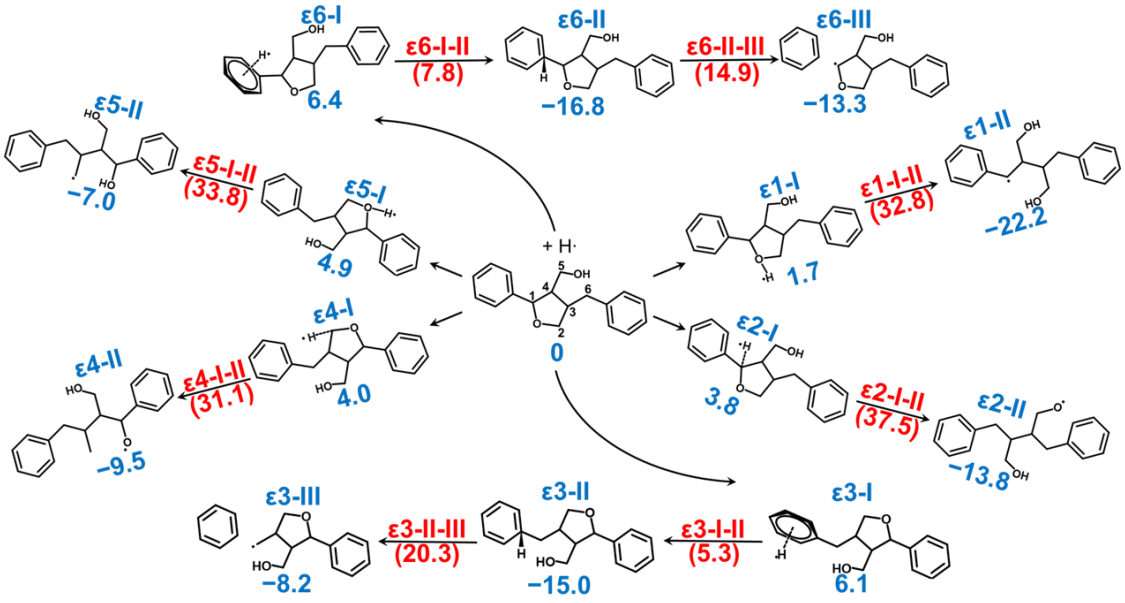

Figure 3-8. Cleavage reaction channels and their energy barriers (in red, kcal/mol) of Linkage-ε with H· and the relative free energies (in blue, kcal/mol) of INTs at 298 K, 1 bar.

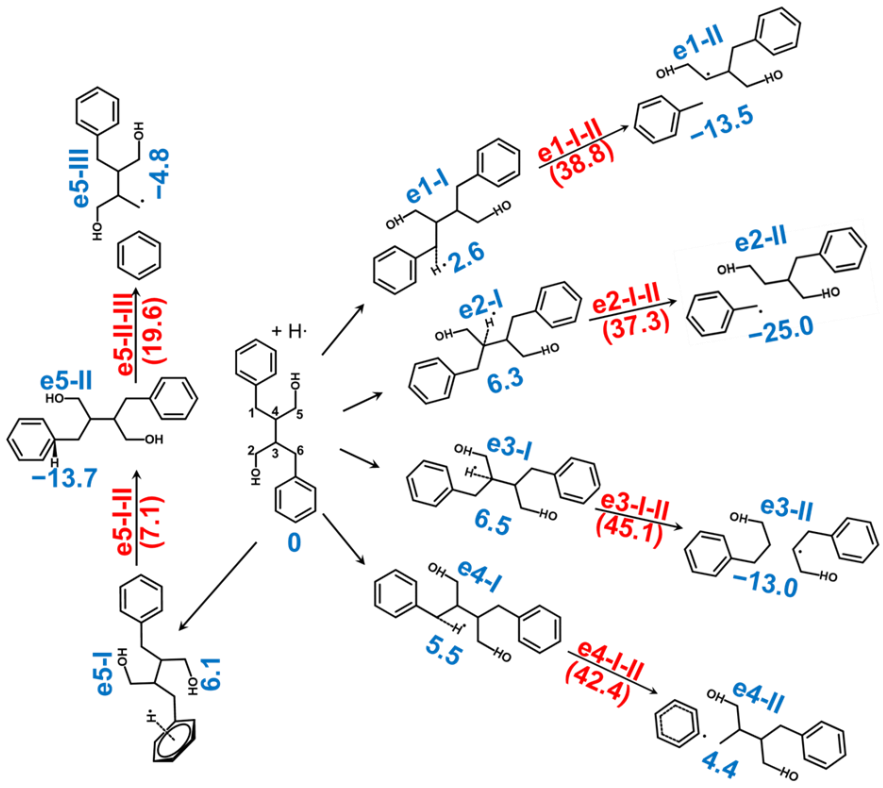

Figure 3-9. Cleavage reaction channels and their energy barriers (in red, kcal/mol) of Linkage-e with H· and the relative free energies (in blue, kcal/mol) of INTs at 298 K, 1 bar.

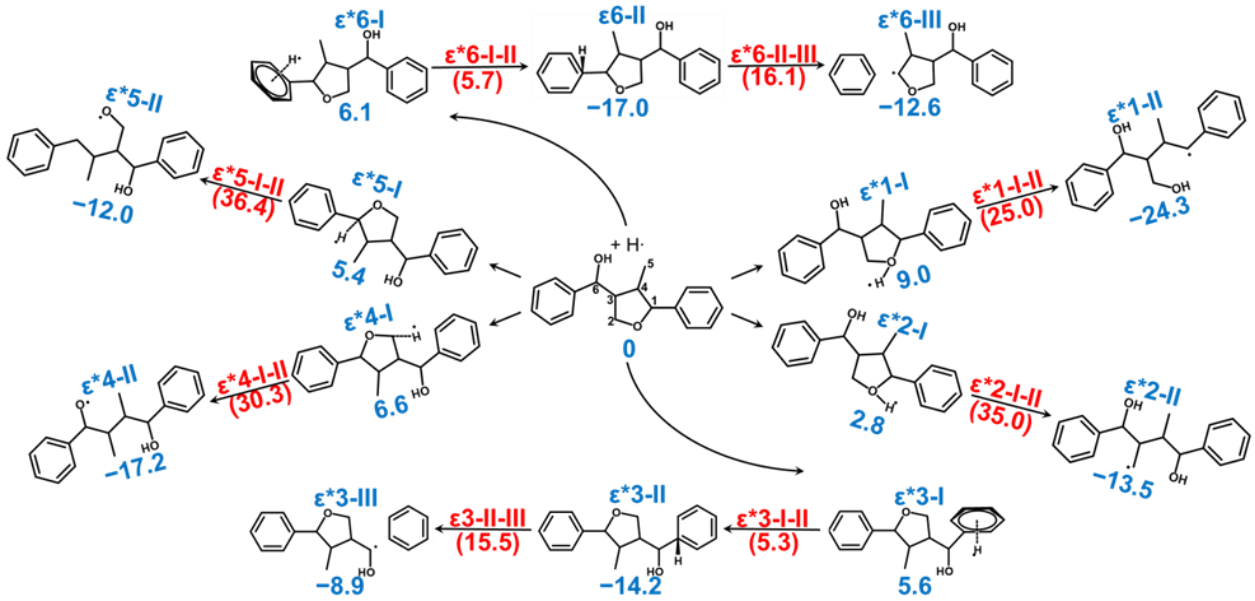

Figure 3-10. Cleavage reaction channels and their energy barriers (in red, kcal/mol) of Linkage-ε* with H· and the relative free energies (in blue, kcal/mol) of INTs at 298 K, 1 bar.

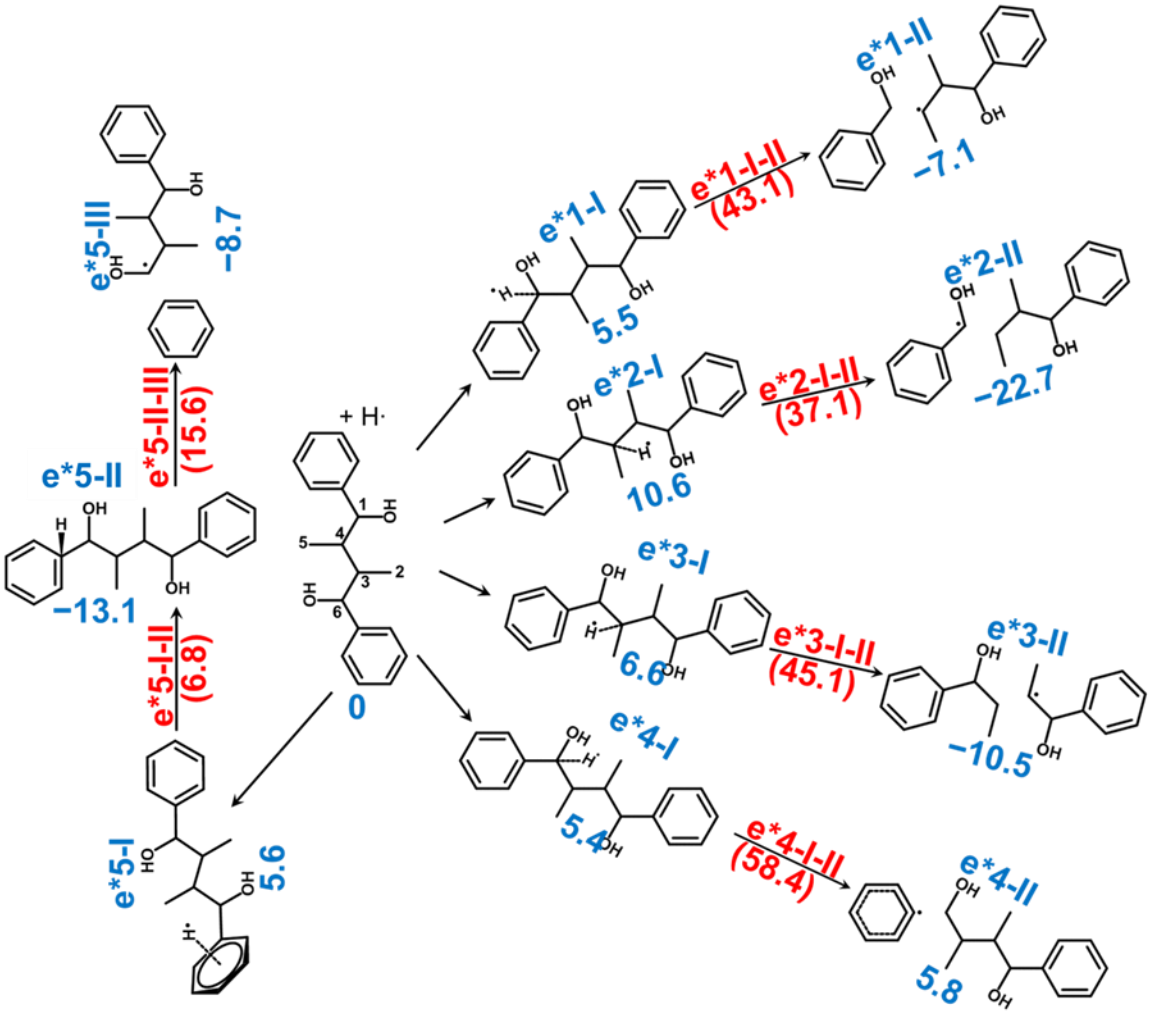

Figure 3-11. Cleavage reaction channels and their energy barriers (in red, kcal/mol) of Linkage-e* with H· and the relative free energies (in blue, kcal/mol) of INTs at 298 K, 1 bar.

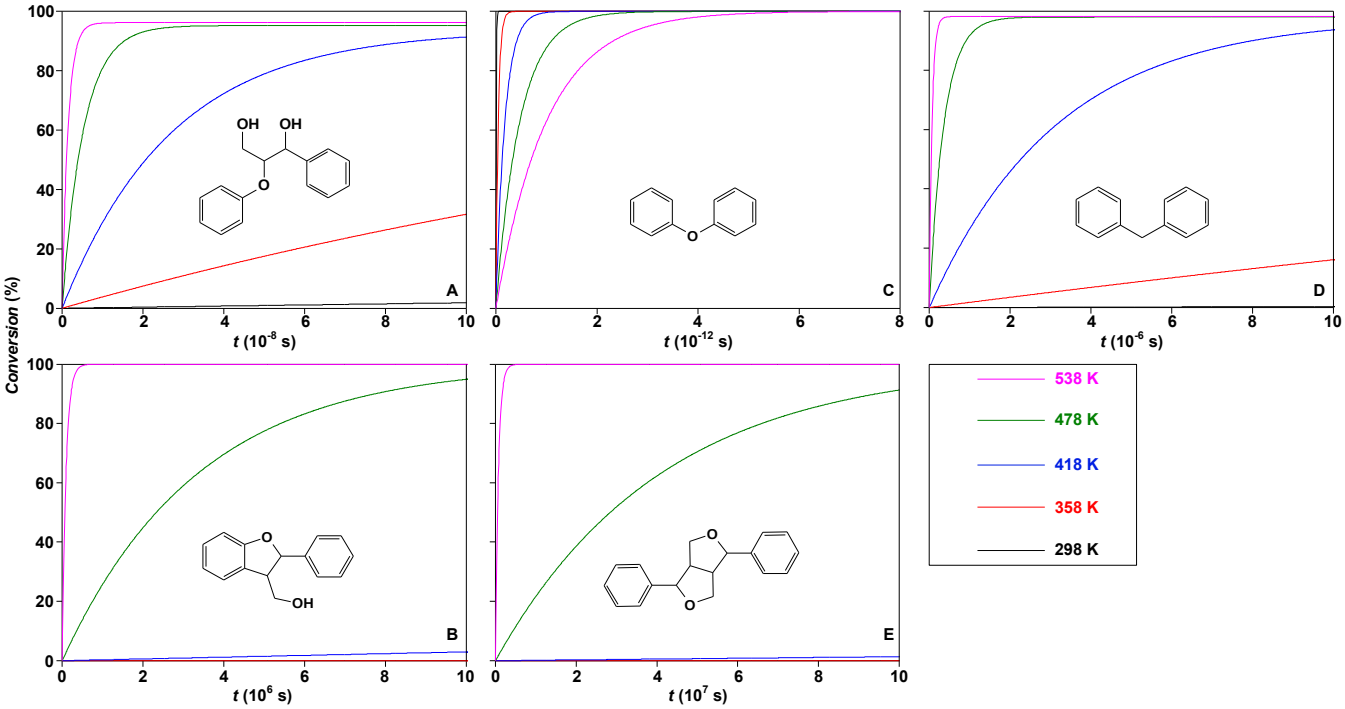

Figure 3-12. Theoretical conversion profiles for hydrogenolysis cleavage of different lignin linkages over different time scales.

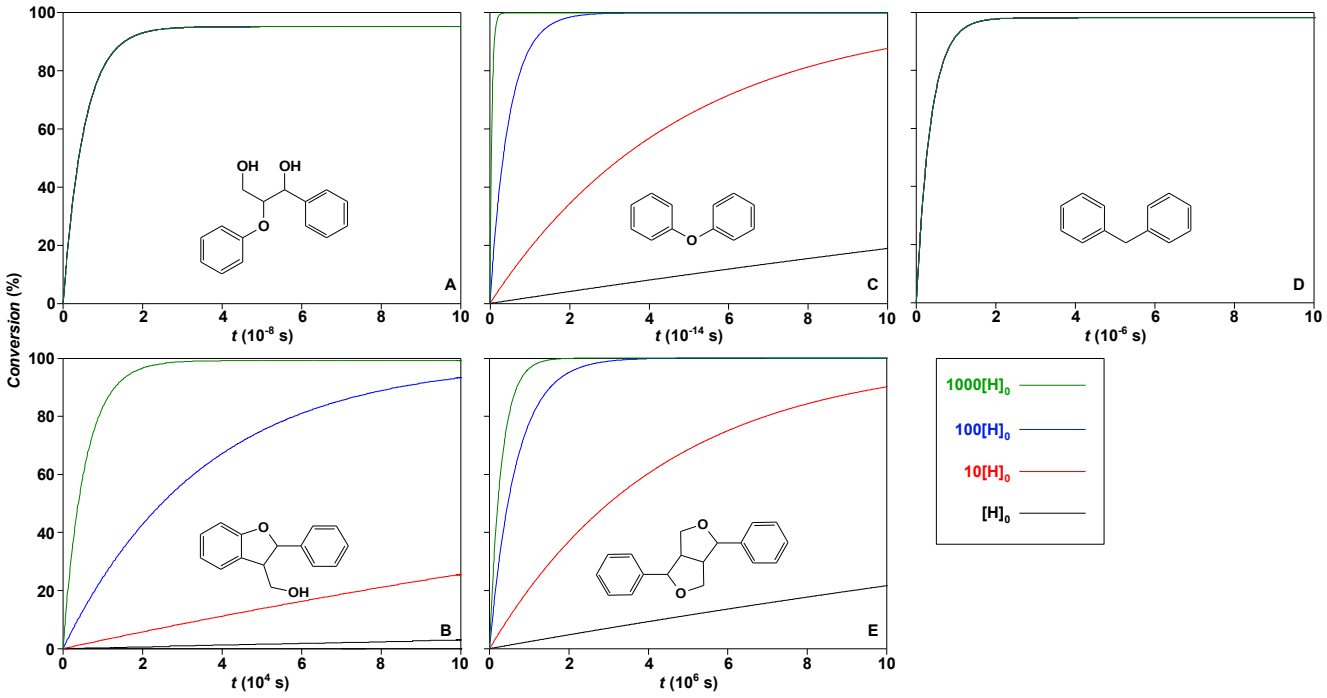

Figure 3-13. Theoretical conversion profiles for hydrogenolysis cleavage of different lignin linkages under different H· concentrations at 478 K, $[H]_0 = l_0$.

Table 3-1. Hydrogenolysis of lignin model compounds and lignin in experimental studies.

No.	Catalyst	T/°C	Feedstock	Major products	Conv./%	Ref.
1	Heterogeneous Ni	120	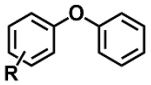	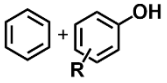	99	4
2	$Ni(COD)_2$, SIPr·HCl	120	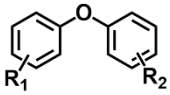	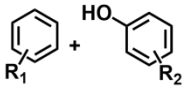	>85	22
3	Ni-TiN	150	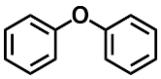	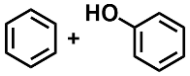	99	44
4	Ni-TiN	125	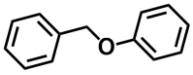	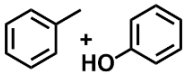	>99	44
5	Ni_7Au_3	170	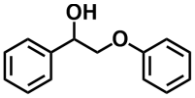	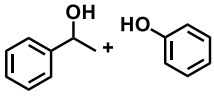	95	45
6	Pt/C	200	Lignin (birch wood)	Monomers, dimers	42	8
7	$Ni_{85}Ru_{15}$	150	Organosolv lignin	Monophenols	42	24
8	$Ni_{85}Rh_{15}$	130	Organosolv lignin	Monophenols	50	24
9	Ni-TiN	150	Kraft lignin	Monophenols	23	44
10	Ni_7Au_3	170	Organosolv lignin	Monophenols	14	45

Chapter 4

Catalytic hydrogenolysis of Kraft lignin to monomers at high yield in alkaline water

4.1. Introduction

Lignin accounts for almost 30% of the organic part of biomass. In consideration of the predicted depletion of fossil resources and the growing threat of global warming, the utilization of lignin has become a center of interest for worldwide scientists and industries, as the lignin, of which more than half of that carbon is aromatic, provides alternative and attractive new sustainable platforms of fuels, chemicals, and materials [1-3]. However, it is still difficult to translate the longstanding interest in lignin valorization into commercial processes due to two facts.

First, although many isolation methods of lignin from biomass are explored, such as organosolv and enzymatic processes [4-5], Kraft method, which employs strong alkalis to cleave the ester bonds between hemicelluloses and lignin macromolecules to isolate lignin, is still the critical process that can be manipulated in large scale and feasible in industry [6]. Kraft lignin (KL) can thus be completely dissolved in alkaline water (pH > 10.5), while the presence of alkalis and water result in the impracticability of many candidate technologies or approaches for the lignin depolymerization. For example, acid-catalyzed depolymerization of lignin is thus eliminated, and some catalysts deactivate rapidly because of promoter leaching in aqueous solution [7]. To avoid the negative impact of alkalis and water, some experimental studies on the depolymerization of KL had to employ anhydrous organic or at most an organic-water mixture as the solvent. For instance, Molinari and co-workers proposed a continuous flow approach for the hydrogenolysis of KL utilizing a TiN-Ni heterogeneous catalyst. Although they admitted that KL had very limited solubility in many common organic solvents, they had to perform their reactions in methanol that was not the worst solvent [8]. Yoshikawa and co-workers investigated the catalytic depolymerization of KL in the presence of a silica-alumina catalyst, employing a water/1-butanol mixture as the reaction medium [9]. There have been some recent studies on the depolymerization of lignin in ionic liquids, but its economic feasibility is even worse than that of organic solvents [10,11]. It is in fact extremely difficult to find an organic solvent that is able to dissolve KL (or other lignin types) completely or efficiently meanwhile independent of the lignin depolymerization. This difficulty has derived a branch subject of lignin depolymerization, i.e., exploration of suitable solvent components and investigation of the solvent effects [12]. For example, Ouyang and co-workers investigated the effects of the solvents comparatively, including water, methanol, 1,4-dioxane, tetrahydrofuran, ethanol, and their cosolvent, on the depolymerization of lignin. They found that 1:1 (v/v) of methanol/water was the best reaction medium, while the yield of monophenolic compounds only reached 18% [13]. Struggling with the solvent may not be a mos direction or approach for the depolymerization of KL in view of industrialization. In our view, depolymerization of KL in alkaline water will be a most promising approach.

Second, efficient approaches to the lignin depolymerization into monomers are still lacking. There are in general three main approaches to the depolymerization, i.e., pyrolysis, oxidation, and hydroprocessing. The pyrolysis has been carried out at temperature between 450 and 600 ℃. It produces a mixture of non-condensable gases, liquid, and solid. A non-selective nature of the pyrolysis normally results in high charcoal yield and low liquid yield (in particular, that of monomers) [14]. Thus, Jones and Zhu concluded that lignin pyrolysis at present is not economically attractive [15]. In contrast to this, oxidation and hydroprocessing have drawn more attention since they are able to depolymerize lignin efficiently under relatively mild reaction conditions [3]. Oxidative depolymerization of lignin aims to produce polyfunctional aromatic compounds, employing nitrobenzene, metal oxides, molecular oxygen, or hydrogen peroxide as the oxidant. To enhance the degradation of lignin, most studies performed the oxidations in the presence of catalysts, such as organometallic [16], metal-free organic [17], metal salts [18], or photocatalytic catalysts [19]. Even milder oxidation without catalyst is a key point of this work, as mentioned later. Xu and co-workers concluded that use of oxidants and/or oxidizing protocols is not a generally adopted practice for lignin depolymerization despite several available relevant studies on the oxidation of lignin model compounds [2]. The most frequently discussed approach to the lignin depolymerization in recent years is hydroprocessing, including hydrogenolysis, hydrogenation, and hydrodeoxygenation. It is difficult to perform only one hydroprocessing type in practice because those three reaction types are concomitant/consecutive, and the best catalytic species for all the three reactions are transition metals, in particular Ni that have been the most popular metallic catalyst used in integrated hydrogen-processing of lignin [20-25]. Both oxidative degradation and hydroprocessing of lignin, however, encounter a common serious problem. In many experimental studies, the model compounds of lignin such as aryl ethers always undergo depolymerization to high conversion, whereas only a limited portion of the actual lignin is converted into monomers and/or oligomers. For example, Zhang and co-workers performed hydrogenolysis of 2-phenoxy-1-phenylethanol over a new type Ni_7Au_3 catalyst with a conversion as high as 95%, while the conversion of an organosolv lignin over the same catalyst was only 14% [26]. This problem seems to originate mainly from the randomly polymerized and three-dimensionally folded structure of lignin macromolecules. The retrogressive reactions leading to repolymerization, self-condensation, and eventually coking of lignin are thus inevitable due to easy formation of radicals and/or C–C bond forming self-condensation reactions under any processing conditions [27,28].

In **Chapter 2**, we introduced a new type of nano-sized Ni catalyst supported by a general material ZSM-5 zeolite [29]. It showed very high activity and stability for hydroprocessing of lignin monomers. Fourteen phenolic compounds that were chosen as lignin monomers were completely hydrogenated, while no loss of activity was detected in repeated use. This heterogeneous Ni catalyst has thus a great potential in application to hydroprocessing of actual lignin. In this study, we applied the above-mentioned Ni catalyst to hydroprocessing of KL that had been dissolved in alkaline water for the first time, employing gaseous hydrogen as the hydrogen donor.

4.2. Experimental section

The Kraft lignin (KL, 0.40 g, Sigma-Aldrich Co.) was dissolved in alkaline water. The pH of the solution was adjusted at 11 by adding Na_2CO_3 powder (purity > 99.8%, Wako Pure Chemical Industries, Ltd.). The volume of the solution was 40 or 30 mL for the hydrogenolysis or oxidation, respectively. The oxidation was performed by dripping 10 mL of H_2O_2 (aqueous solution with concentration; 30 wt%) to 30 mL solution of KL that was heated at 60 ℃ and stirred at 400 rpm. The solution was then heated up to 70 ℃ and stirred at 400 rpm for 24 h, within which H_2O_2 was consumed completely. The solution, i.e., that of OKL, was finally cooled down to ambient temperature.

A Ni/ZSM-5 catalyst was employed for the hydrogenation of KL and OKL [29]. The solution of KL or OKL was suspended with 0.40 g of the catalyst and transferred to an SUS-made autoclave with a volume of 100 mL. After the autoclave was closed, the air in the headspace was replaced by H_2 at pressure of 4.0 MPa (at 25 ℃), and then heated up to 200 ℃ while the suspension was stirred at an impeller rotation rate of 400 rpm. After continuation of the heating at 200 ℃ for 4 h, the suspension was cooled to ambient temperature, and then opened. The suspension was recovered and filtrated immediately. The filtrate cake was a mixture of charcoal (KL-C or OKL-C) and spent catalyst. The filtrate was acidified to pH = 2, and then filtered to recover the solution of KL-M or OKL-M and the residual lignin (KL-R or OKL-R) separately. The solutions of KL-M and OKL-M were subjected to liquid-liquid extraction with dichloromethane. KL-M and OKL-M were recovered as oils after evaporative removal of dichloromethane from the solutions. The oils were re-dissolved into acetone or tetrahydrofuran, and analyzed by gas chromatography mass-spectrometry (GC/MS, PerkinElmer, Clarus 680/SQ-8S model) and gel permeation chromatography (GPC, Shimadzu), respectively. KL, KL-R and OKL-R were analyzed by the same GPC as above, and Fourier transform infrared spectroscopy (FTIR) with a spectrometer (Perkin Elmer Spectrum Two) which was also used to analyze OKL. KL, OKL, KL-R, and OKL-R were also analyzed by two-dimensional heteronuclear multiple quantum coherence spectroscopy (2D-HMQC) on a JOEL model (JNM-ECA400). Solid state ^{13}C-NMR was applied to measure the carbon type distribution of solids (KL, OKL, KL-R, and OKL-R).

The conversion of KL and the yields of monomers, charcoal and residue were defined as follows.

$$W_r = \frac{\text{mass of residual lignin}}{\text{mass of KL}} \times 100 \text{ (wt\%-KL)}$$

$$W_c = 100 \text{ (wt\%-KL)} - W_o - W_r$$

$$W_o = \frac{\text{mass of oil}}{\text{mass of KL}} \times 100 \text{ (wt\%-KL)}$$

Total conversion of lignin: $Conv. = 100\% - W_r$

DFT calculations were performed by employing Becke ’88 exchange and Lee-Yang-Parr correlation functionals [30,31], which had been implemented in the ORCA package [32]. The Def2-SVP basis sets of the

Ahlrichs group with auxiliary basis sets for Ahlrichs Coulomb fitting were applied to all the H, C, and O atoms of electroneutral molecules [33,34]. Truhlar's minimally augmented Def2-SVP basis sets by diffuse s and p functions with automatically constructed auxiliary basis sets were applied to all the H, C, and O atoms of electronegative molecules [35]. With Grimme's dispersion correction of D3 version (Becke-Johnson damping) and geometrical counterpoise correction [36,37]. fully relaxed geometry optimizations were performed under the convergence criteria of total energy change < 5×10^{-6} a.u., total root mean square (RMS) gradient < 1×10^{-4} a.u., total maximum element of gradient < 3×10^{-4} a.u., total RMS displacement < 2×10^{-3} a.u., and total maximum displacement < 4×10^{-3} a.u.. With numerical integration grid of Lebedev 302 points, self-consistent field procedures were performed with energy convergence criterion < 1×10^{-7} a.u. and without any orbital symmetry constraints. In consideration of the influences of water molecules, Klamt's conductor like screening model (COSMO) was employed for the simulation of solvent molecules in the vicinity [38]. The simulations on the basis of semi-empirical method were performed by employing Stewart's PM6 Hamiltonian with Grimme's dispersion correction of D3 version and Řezáč's hydrogen bonding correction of H4 version [36,39,40], which had been implemented in the MOPAC2016 package [41]. Fully relaxed geometry optimizations were performed under the termination criteria of the gradient norm < 0.01 kcal/mol/Å, and self-consistent field procedures were performed with convergence criterion of energy change < 1×10^{-7} kcal/mol on two successive iterations. COSMO was employed for the simulation of the influences from water molecules in the vicinity [38].

4.3. Results and discussion

Our catalyst was active enough to catalyze the hydrogenolysis of the KL even in alkaline water. The conversion of KL into monomers reached 23.3 wt%. Compared with some catalysts that were available only in anhydrous and non-alkaline solvents in other reports [8,12], our catalyst performed well. The above result is interesting, because it is recognized that the water adsorption onto the catalyst surface and the formation of metallic hydroxide in alkaline water normally deactivate metallic catalysts rapidly [42-46]. According to our previous study [29], the interaction between the highly dispersive Ni particles and the support was so remarkable that the Ni particles can be well protected from alkalis and water.

Although our catalyst performed well in the hydrogenolyis of KL, 56.0 wt% of KL was not converted to monomers while charcoal yield was as high as 20.7 wt%. The low-yield monomers and high-yield charcoal are universal problems among various types of lignin depolymerization. Li and co-workers claimed that deep understanding of the related mechanisms is the prerequisite to increase the conversion of the lignin into monomers and reduce the charcoal yield [3]. On the basis of density functional theory (DFT), we performed simulation of a small fragment of lignin macromolecule (SLF, $C_{78}H_{90}O_{25}$, **Figure 4-1**) containing 8 monomer units. Computational details are described in the experimental section. The global structural relaxation of SLF results in a folded geometry. As shown in **Figure 4-2**, SLF folds as much as possible to shrink itself due to the

presence of strong intramolecular hydrogen bonds with an average hydrogen bond length of 2 Å. The molecular length of SLF with a completely straightening backbone is *ca.* 41 Å, but the longest distance between any two atoms of the folded SLF is only 15 Å. Because of the folded geometry, some moieties of SLF are inaccessible to the molecular vicinity. For example, No. 2 aromatic ring is sandwiched by No. 1 and 3 rings. No. 4 aromatic ring is at the center of the folded SLF, shielded by all the other aromatic rings. The distances among these aromatic rings are so short that SLF is easy to self-condense once radicals (or other reactive intermediates) are formed therein. Such molecular conformation is believed to be the main reason of inevitable high-yield charcoal for any approaches of lignin depolymerization. Moreover, the surface negative potential of SLF concentrates at the hydroxyl groups. According to our study [29], molecular sites with negative potential positions will easily be chemisorbed onto the surface of metallic catalyst. In other words, dehydroxylation or hydroxyl oxidation ought to be the primary reaction in the hydroprocessing, and then the chemisorption and hydrogenolysis of the lignin backbone are possible. This explains why the phenolic monomer products from the hydroprocessing of lignin are mainly substituted by alkyl or carbonyl but not hydroxyalkyl groups.

The phenolic hydroxyl group of SLF loses a proton to form $[Neg\text{-}SLF]^-$ in alkaline water. Compared with the geometry of SLF, the folded state of $[Neg\text{-}SLF]^-$ is not radically changed even in alkaline water, so a high-yield charcoal was gotten in our experimental study . However, No. 1 aromatic ring of $[Neg\text{-}SLF]^-$ is no longer fettered by intramolecular hydrogen bonds due to the loss of the proton of the phenolic hydroxyl group. In addition to this, the negative charge concentrated area is extended, so $[Neg\text{-}SLF]^-$ has more locations for chemisorption onto the catalyst surface. We thus realize that if the intramolecular hydrogen bonds of lignin macromolecules can be completely or mostly eliminated, the geometry of the lignin macromolecule changes greatly. It is supposed that all alcoholic hydroxyl groups of $[Neg\text{-}SLF]^-$ are sufficiently oxidized, which is the most likely operation to convert the hydroxyl groups. The $–CH_2OH$ and $–CH(OH)–$ groups are eventually oxidized to $–COO^-$ and $–CO–$ in alkaline water, respectively. The optimized geometry of oxidized $[Neg\text{-}SLF]^-$ ($[Oxi\text{-}SLF]^{8-}$) is shown in **Figure 4-2**. As we expected, the originally folded molecule has been well stretched because of the loss of intramolecular hydrogen bonds and the repulsion among the abundant negative charge of $[Oxi\text{-}SLF]^{8-}$. The stretched molecule has more active sites accessible to the catalyst surface. The distances among the aromatic rings are largely increased that the self-condensation and re-polymerization during hydroprocessing will be greatly limited.

In order to support the simulation results on the basis of DFT, we employed a semi-empirical method to simulate a much bigger lignin fragment (BLF, $C_{188}H_{214}O_{66}$, **Figure 4-1**). As shown in **Figure 4-3**, BLF with the most stable geometry of is tightly folded. The energy of BLF increases along with its stretching. There are two phenolic hydroxyl groups in BLF, which lose protons to become $[Neg\text{-}BLF]^{2-}$ in alkaline water. Note that the energy of $[Neg\text{-}BLF]^{2-}$ will decrease temporarily with slightly stretching, but the energy increase will be inevitable if the macromolecule is further stretched because most of the moieties of $[Neg\text{-}BLF]^{2-}$ are still fettered

by intramolecular hydrogen bonds. In other words, both BLF and $[Neg\text{-}BLF]^{2-}$ will keep their tightly folded structures in alkaline water. After oxidation of all the alcoholic hydroxyl groups of $[Neg\text{-}BLF]^{2-}$ to $–COO^-$ or –CO−, the formed $[Oxi\text{-}BLF]^{18-}$ decreases its energies in alkaline water through its stretching. The molecular inner of the originally folded BLF or $[Neg\text{-}BLF]^{2-}$ is then exposed to the vicinity. High-yield monomers and low-yield charcoal of lignin hydroprocessing can thus be expected, if KL can be oxidized properly before the hydroprocessing.

As aforementioned, oxidative cracking is a candidate for depolymerization of lignin, but development of this approach is limited. Most studies look forward to high-yield depolymerization of lignin only through oxidation, but high-efficient oxidative cracking of backbone of actual lignin is still very difficult even in the presence of some novel catalysts [2,3]. Even if the lignin backbone is oxidized, the rearrangement and oligomerization of intermediate products of lignin fragmentation are uncontrollable and undesirable side reactions [47]. However, in this study, oxidation of the alcoholic hydroxyl groups of lignin at mild conditions without catalysts is enough to stretch the lignin macromolecules. We thus propose the mechanisms of the alcoholic hydroxyl groups of KL that are oxidized by H_2O_2 in alkaline water as Eqs. (1) to (4).

$$H_2O_2 + OH^- \rightarrow HOO^- + H_2O \tag{1}$$

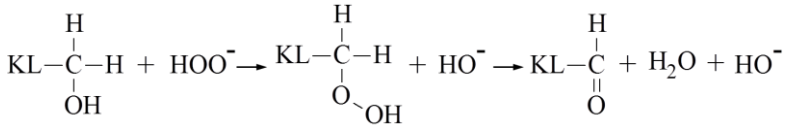

(2)

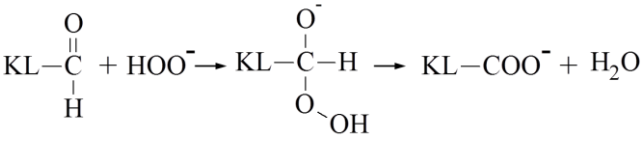

(3)

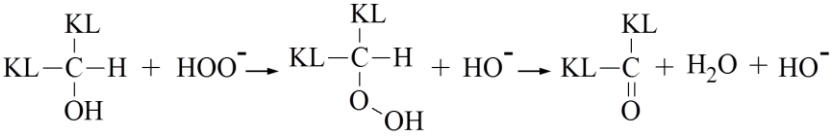

(4)

As seen in **Figure 4-4**, the appearances of the KL and oxidized KL (OKL) solutions are clearly different from each other through the entire range of conversion. It is well known that lignin is highly polymerized and its monomers are phenolic compounds, but there are few structures of long-chain conjugated or condensed aromatics in lignin. Quinones are deemed as the main chromophores of lignin, but high concentration of quinones can be generated only after sufficient depolymerization and oxidation of lignin. Therefore, covering the entire visible light region, i.e., black color, of KL solution should be attributed mainly to the tightly folded lignin macromolecules in which aromatic rings are forced to be crowded. The aromatic rings overlapping each other thus generate pseudo highly-condensed aromatics that adsorb visible light. In contrast, OKL solution is

transparent and orange colored probably due to the stretched lignin macromolecules that do not adsorb red light. Compared with the KL and OKL solutions, both those of KLH and OKLH have paler colors, and this is a strong indication of depolymerization by the hydrogenolysis. Another comparison between the KLH and OKLH solutions displays difference in the progress of depolymerization between KL and OKL. Acidification of the KLH (to pH 2) solution caused a major portion of the solute precipitate (KL-R). This is explained well by depolymerization of KL with a limited extent. The precipitate from the OKLH solution (OKL-R) is much less than that from KLH. The aqueous solutions of water-soluble products from the filtration of Acid-KLH and Acid-OKLH, respectively, were subjected to liquid-liquid extraction with dichloromethane, and then the extracts, referred respectively to as KL-M and OKL-M were recovered as oils.

The effectiveness of the H_2O_2 oxidation of KL is clearly seen in **Table 4-1**. The introduction of the oxidation increases the conversion of KL and that into the oil from 44 to 91 wt% and 23 to 83 wt%, respectively. It is also noted that the charcoal formation is suppressed significantly by the oxidation.

As shown in **Figure 4-5**, the composition of monomers in KL-M and OKL-M are similar to each other. The oxidation seems to influence the monomer distribution only slightly. Both KL-M and OKL-M consist mainly of nine types of monomers. The yields of the individual monomers are shown in **Table 4-2**. The total yields of the nine monomers accounted for 91% of OKL-M (i.e., 76 wt%-lignin). It is difficult to ascribe these monomers to specific linkages of lignin strictly because there are several inter-monomer linkage types in lignin, such as *β*-O-4 ether bonds, *β*-5 phenylcoumaran bonds, diphenyl ether 4-O-5', *β*-1' diphenyl methane, and *β*-*β*' pinoresinol bonds. Some monomers can be formed from most of these linkages. For example, guaiacol is probably formed by the depolymerization of any linkages, and therefore its yield is the highest. Note that the nine types of monomers are classified into two groups according to the presence or absence of carbonyl. The selectivity to the monomers is summarized in **Table 4-3**. It is obvious that, as for either group of the monomers in OKL-M, the relative contents of the monomers substituted by long chain groups are higher than that of KL-M. According to our recent study [48], the dissociation of a lignin linkage without chemisorption onto catalyst surface is prone to generate aromatic rings that are substituted by short chains, such as methyl, hydroxyl, or formyl group, because short chain substituent can effectively be stabilized by the conjugation of aromatic ring. A lignin linkage of which hydroxyls have been oxidized to carboxyls is much easier to be chemisorbed and stabilized by the catalyst surface than the original linkage; so long chain groups substituted monomers can be easier generated. In addition, we detected no monomers in the solutions of KL and OKL. This fact indicates that KL cannot be depolymerized to monomers by the mild oxidation under the present condition. In addition, we found neither dimers nor oligomers in KL-M and OKL-M even through the GC-MS detection of long retention time (with high temperature). Dimers and/or oligomers might have been formed by the hydrogenolysis but with very low yields.

In **Figure 4-6**, the molecular weight (MW) distributions show that both KL-M and OKL-M consist mainly of monomers. For both KL-M and OKL-M, the peaks located at 25–30 min include all of the monomers that are

shown in **Figure 4-5**, and the small peaks before 25 min indicate the presence of small amounts of dimers or oligomers, which is consistent with the GC/MC chromatograms in **Figure 4-5**. The MW of KL distributes over a range from 300 to 10,000 Da, while the major components have MW less than 5,000 Da. OKL could not be analyzed by GPC because OKL was not fully dissolved into the carrier solvent, tetrahydrofuran (THF). We also found that OKL was not fully dissolved even into either *N*,*N*-dimethylformamide or dimethyl sulfoxide. The alkaline water thus seemed to be the sole good solvent of OKL. It was also suggested that the presence of alcoholic hydroxyl groups, which were lost to more or less extent by the oxidation, were necessary for the solubility of KL into THF and other organic solvents. The hydrogenolysis recuperated the solubility, which was evidenced by that of OKL-R (see its chromatogram in **Figure 4-6**). Such recuperation was ascribed to conversion of oxidation-derived carbonyls back into hydroxyls through the hydrogenolysis. It is strongly suggested from similarity in the MW range between OKL-R and KL that the oxidative depolymerization of KL was, if any, insignificant. The MW distribution of KL-R seems to be located at the higher MW side, if compared with those of KL and OKL-R. This is explained by the repolymerization and/or self-condensation of KL macromolecules during the hydrogenolysis. The molecular structures of KL, OKL, KL-R and OKL-R are discussed in more detail later.

FTIR spectra of **Figure 4-7** show the variations of the distribution of functional groups in KL through the oxidation and hydrogenolysis. The assignments of representative IR absorption are listed in **Table 4-4** [49-52]. The presence of hydroxyl groups in KL is clearly shown by Peak 1 caused by −OH stretching vibration. The presence of native carbonyl groups in KL and also that in the others are indicated by Peaks 3 and 4. The oxidation enhances Peak 4 significantly, and this is consisted with the conversion of alcoholic hydroxyl to carbonyl groups (including ketones from secondary alcohols) or carboxyl groups (from primary alcohols). Peak 7 occurring from the deformation vibration of aromatic C−H is largely enhanced as well. This is probably due to that stretched macromolecules of OKL allow more vibrations of aromatic C−H than that of KL. The spectra of KL-R and OKL-R are relatively similar to that of KL in terms of intensities of IR bands. During the hydrogenolysis, native carbonyl groups in both KL and OKL were mostly reduced, while might also be newly formed by the dissociation of ether bonds. Peak 4 of OKL-R is therefore much smaller than that of OKL, but Peaks 3 and 4 of both KL-R and OKL-R are stronger than that of KL.

Figure 4-8 exhibits the $^{1}H-^{13}C$ correlation for KL, OKL, KL-R, and OKL-R. The representative signals of γ-CH_2OH and α-CH in the HMQC spectrum of KL indicate the presence of β-O-4 and β-5 linkages. The intensive signal due to Ar-OCH_3 is attributed to guaiacol moieties [53-55]. No signals from either hydroxymethyl or hydroxymethylene moieties are detected in the spectrum of OKL, and this is due to the oxidization of a large number of the hydroxyl groups. Instead, the signals of C-H bonding to C=O arise, showing the occurrence of carbonyl, aldehyde, or carboxyl groups. The presence of aldehyde groups is detected in the HMQC spectrum of OKL, while that of carbonyl and carboxyl groups cannot be detected directly because of the absence of bonding

H-C. The solid ^{13}C-NMR was thus employed to certify the presence of carbonyl and carboxyl groups [56,57]. As shown in **Figure 4-9** and **Table 4-5**, their presences are obvious in the spectrum of OKL. On the other hand, signals due to -CH_2OH seems to diminish during the oxidation. This is in agreement with the oxidation of alcoholic hydroxyl groups. **Figure 4-9** also verifies that most of γ-CH_2OH groups of KL are oxidized to $-COO^-$ according to the above-mentioned Eqs. (2) and (3). In contrast to the spectra of KL and OKL, those from KL-R and OKL-R show abundance of aliphatic C-H. This is reasonably explained by dehydroxylation during the hydrogenolysis. Compared with the KL spectrum, that of KL-R shows more intensive signal assigned to β-5 linkage. Our recent study proved theoretically that the lignin linkages containing hydrofuran rings such as β-5 are virtually inert to hydrogenolysis if without chemisorption on the catalyst surface [48]. More β-5 linkages thus remain in KL-R than in OKL-R. The signal of γ-CH_2OH bonding to C=C is particularly obvious in the spectrum of KL-R. A Possible mechanism of the formation and subsequent reactions of the C=C bonds is proposed in **Scheme 4-1**. The C=C moieties of a stretched lignin macromolecule have more opportunities of chemisorption onto the catalyst surface. According to the superdelocalizability of C=C bond and the principle of biatomic hydrogen transfer [58,59], such C=C moieties will be easily and rapidly hydrogenated onto the catalyst surface. There are thus few C=C moieties in OKL-R. The C=C moieties of KL consisting of tightly folded macromolecules are much less accessible to the catalyst surface. The hydrogenation of C=C bond by the biatomic hydrogen transfer is impossible, but monoatomic hydrogen transfer will generate free radical intermediates. Such reactive intermediates are stable due to the conjugation of adjacent aromatic rings [48], so they are prone to bond with each other in the moiety of crowded aromatic rings, undergoing re-polymerization (**Scheme 4-1**). As a result of this, the quantity of tertiary carbon in KL-R increases, which has been proved by the solid ^{13}C-NMR spectra (**Figure 4-9**).

4.4. Conclusions

The hydrogenolysis of KL was successfully performed in alkaline water with the Ni/ZSM-5 catalyst. The DFT-based simulation, together with a semi-empirical method, predicted that a lignin macromolecule, of which alcoholic hydroxyl groups had been oxidized to a sufficient degree, was stretched well in the alkaline water due to the loss of original intramolecular hydrogen bonds and the repulsion among the abundant negative charge. The oxidation thus improved the accessibility of reactive sites of the macromolecule to the catalyst surface, and in addition, suppressed re-polymerization and self-condensation during the hydrogenolysis. These theoretical expectations were well consistent with the experimental facts. The alcoholic hydroxyl groups of KL can be sufficiently oxidized by H_2O_2 under mild conditions. This was verified by FTIR, HMQC, and solid ^{13}C-NMR spectra. The conversion of hydrogenolysis of Kraft lignin and that into monomers were thus increased from 44 to 91 wt% and 23 to 83 wt%, respectively. Moreover, the re-polymerization and self-condensation during

hydrogenolysis were effectively limited according to the GPC profiles and HMQC spectra. This strategy may open up a route for translation of the longstanding interest in lignin utilization into commercial processes.

4.5. References

1 J. Zakzeski, P. C. A. Bruijnincx, A. L. Jongerius and B. M. Weckhuysen, *Chem. Rev.*, 2010, **110**, 3552−3599.

2 C. P. Xu, R. A. D. Arancon, J. Labidi and R. Luque, *Chem. Soc. Rev.*, 2014, **43**, 7485−7500.

3 C. Z. Li, X. C. Zhao, A. Q. Wang, G. W. Huber and T. Zhang, *Chem. Rev.*, 2015, **115**, 11559−11624.

4 X. J. Pan, N. Gilkes, J. Kadla, K. Pye, S. Saka, D. Gregg, K. Ehara, D. Xie, D. Lam and J. Saddler, *Biotechnol. Bioeng.*, 2006, **94**, 851−861.

5 J. C. Pew, *Tappi*, 1957, **40**, 553−558.

6 B. Xiao, X. F. Sun and R. C. Sun, *Polym. Degrad. Stab.*, 2001, **74**, 307−319.

7 M. Besson, P. Gallezot and C. Pinel, *Chem. Rev.*, 2014, **114**, 1827−1870.

8 V. Molinari, G. Clavel, M. Graglia, M. Antonietti and D. Esposito, *ACS Catal.*, 2016, **6**, 1663−1670.

9 T. Yoshikawa, T. Yagi, S. Shinohara, T. Fukunaga, Y. Nakasaka, T. Tago and T. Masuda, *Fuel Process. Technol.*, 2013, **108**, 69−75.

10 F. Liu, Q. Y. Liu, A. Q. Wang and T. Zhang, *ACS Sustainable Chem. Eng.*, 2016, **4**, 3850−3856.

11 R. Prado, X. Erdocia, G. F. De Gregorio, J. Labidi and T. Welton, *ACS Sustainable Chem. Eng.*, 2016, **4**, 5277−5288.

12 Q. Song, F. Wang, J. Cai, Y. Wang, J. Zhang, W. Yu and J. Xu, *Energy Environ. Sci.*, 2013, **6**, 994−1007.

13 X. P. Ouyang, T. Ruan and X. Q. Qiu, *Fuel Process. Technol.*, 2016, **144**, 181−185.

14 H. B. Goyal, D. Seal and R. C. Saxena, *Renew. Sust. Energy Rev.*, 2008, **12**, 504−517.

15 S. Jones and Y. Zhu, in *Preliminary economics for the production of pyrolysis oil from lignin in a cellulosic ethanol biorefinery*, Pacific Northwest National Laboratory: Richland, 2009, pp. 1−32.

16 W. A. Herrmann and R. W. Fischer, *J. Am. Chem. Soc.*, 1995, **117**, 3223−3230.

17 S. P. Mishra, J. Thirree, A. S. Manent, B. Chabot and C. Daneault, *Bioresources*, 2011, **6**, 121−143.

18 T. Voitl and P. Rudolf von Rohr, *ChemSusChem*, 2008, **1**, 763−769.

19 M. Ugurlu and M. H. Karaoglu, *Chem. Eng. J.*, 2011, **166**, 859−867.

20 K. Barta, G. R.Warner, E. S. Beach and P. T. Anastas, *Green Chem.*, 2014, **16**, 191−196.

21 Y. Y. Wang, L. L. Ling and H. Jiang, *Green Chem.*, 2016, **18**, 4032−4041.

22 M. Wang, L. H. Li, J. M. Lu, H. J. Li, X. C. Zhang, H. F. Liu, N. C. Luo and F. Wang, *Green Chem.*, 2017, **19**, 702−706.

23 C. F. Zhang, J. M. Lu, X. C. Zhang, K. MacArthur, M. Heggen, H. J. Li and F. Wang, *Green Chem.*, 2016, **18**, 6545−6555.

24 Z. Li, M. Garedew, C. H. Lam, J. E. Jackson, D. J. Miller and C. M. Saffron, *Green Chem.*, 2012, **14**, 2540−2549.

25 C. H. Lam, C. B. Lowe, Z. Li, K. N. Longe, J. T. Rayburn, M. A. Caldwell, C. E. Houdek, J. B. Maguire, C. M. Saffron, D. J. Miller and J. E. Jackson, *Green Chem.*, 2015, **17**, 601−609.

26 J. G. Zhang, H. Asakura, J. van Rijn, J. Yang, P. Duchesne, B. Zhang, X. Chen, P. Zhang, M. Saeys and N. Yan, *Green Chem.*, 2014, **16**, 2432−2437.

27 M. P. Pandey and C. S. Kim, *Chem. Eng. Technol.*, 2011, **34**, 29–41.

28 C. Li, M. Zheng, A. Wang and T. Zhang, *Energy Environ. Sci.*, 2012, **5**, 6383–6390.

29 S. C. Qi, L. Zhang, H. Einaga, S. Kudo, K. Norinaga and J. –i. Hayashi, *J. Mater. Chem. A*, 2017, **5**, 3948–3965.

30 A. D. Becke, *Phys. Rev. A*, 1988, **38**, 3098–3100.

31 C. Lee, W. Yang and R. G. Parr, *Phys. Rev. B*, 1988, **37**, 785–789.

32 F. Neese, *The ORCA program system, Version 3.0.3*, Wiley Interdiscip. Rev.: Comput. Mol. Sci., 2012, **2**, 73–78.

33 F. Weigend and R. Ahlrichs, *Phys. Chem. Chem. Phys.*, 2005, **7**, 3297−3305.

34 F. Weigend, *Phys. Chem. Chem. Phys.*, 2006, **8**, 1057−1065.

35 J. J. Zheng, X. F. Xu and D. G. Truhlar, *Theor. Chem. Acc.*, 2010, **128**, 295−305.

36 S. Grimme, S. Ehrlich and L. Goerigk, *J. Comput. Chem.*, 2011, **32**, 1456−1465.

37 H. Kruse and S. Grimme, *J. Chem. Phys.*, 2012, **136**, 154101.

38 A. Klamt, *J. Phys. Chem.*, 1995, **99**, 2224−2235.

39 J. J. P. Stewart, *J. Mol. Model.*, 2007, **13**, 1173−1213.

40 J. Řezáč and P. Hobza, *J. Chem. Theory Comput.*, 2012, **8**, 141−151.

41 J. J. P. Stewart, *MOPAC2016, Version 16.175L*, Stewart Computational Chemistry, http://openmopac.net/.

42 W. W. Lin, H. Y. Cheng, J. Ming, Y. C. Yu and F. Y. Zhao, *J. Catal.*, 2012, **291**, 149–154.

43 S. Behtash, J. M. Lu, E. Walker, O. Mamun and A. Heyden, *J. Catal.*, 2016, **333**, 171–183.

44 R. Gholami, M. Alyani and K. J. Smith, *Catalysts*, 2015, **5**, 561–594.

45 M. D. Argyle and C. H. Bartholomew, *Catalysts*, 2015, **5**, 145–269.

46 C. H. Bartholomew, *Appl. Catal. A: General*, 2001, **212**, 17–60.

47 S. Constant, M. Robitzer, F. Quignard and F. Di Renzo, *Catal. Today*, 2012, **189**, 123−128.

48 S. C. Qi, L. Zhang, S. Kudo, K. Norinaga and J. –i. Hayashi, *J. Phys. Chem. A*, 2017, **121**, 2868−2877.

49 C. Mancera, F. Ferrando, J. Salvadó and N. E. El Mansouri, *Biomass Bioenergy*, 2011, **35**, 2072−2079.

50 O. Derkacheva and D. Sukhov, *Macromol. Symp.*, 2008, **265**, 61–68.

51 K. K. Pandey, *J. Appl. Poly. Sci.*, 1999, **71**, 1969–1975.

52 Q. Liu, S. R. Wang , Y. Zheng, Z. Y. Luo and K. F. Cen, *J. Anal. Appl. Pyrolysis*, 2008, **82**, 170–177.

53 M. Y. Balakshin, E. A. Capanema, C. L. Chen and H. S. Gracz, *J. Agric. Food Chem.*, 2003, **51**, 6116–6127.

54 E. A. Capanema, M. Y. Balakshin and J. F. Kadla, *J. Agric. Food Chem.*, 2005, **53**, 9639–9649.

55 E. A. Capanema, M. Y. Balakshin, C. L. Chen, J. S. Gratzl and H. Gracz, *Holzforschung*, 2001, **55**, 302–308.

56 J. D. Mao, K. M. Holtman, J. T. Scott, J. F. Kadla and K. Schmidt-Rohr, *J. Agric. Food Chem.*, 2006, **54**, 9677–9686.

57 H. X. Ben and A. J. Ragauskas, *Energy Fuels*, 2011, **25**, 2322–2332.

58 S. C. Qi, X. Y. Wei, Z. M. Zong and Y. K. Wang, *RSC Adv.*, 2013, **3**, 14219−14232.

59 S. C. Qi, L. Zhang, X. Y. Wei, J. –i. Hayashi, Z. M. Zong and L. L. Guo, *RSC Adv.*, 2014, **4**, 17105−17109.

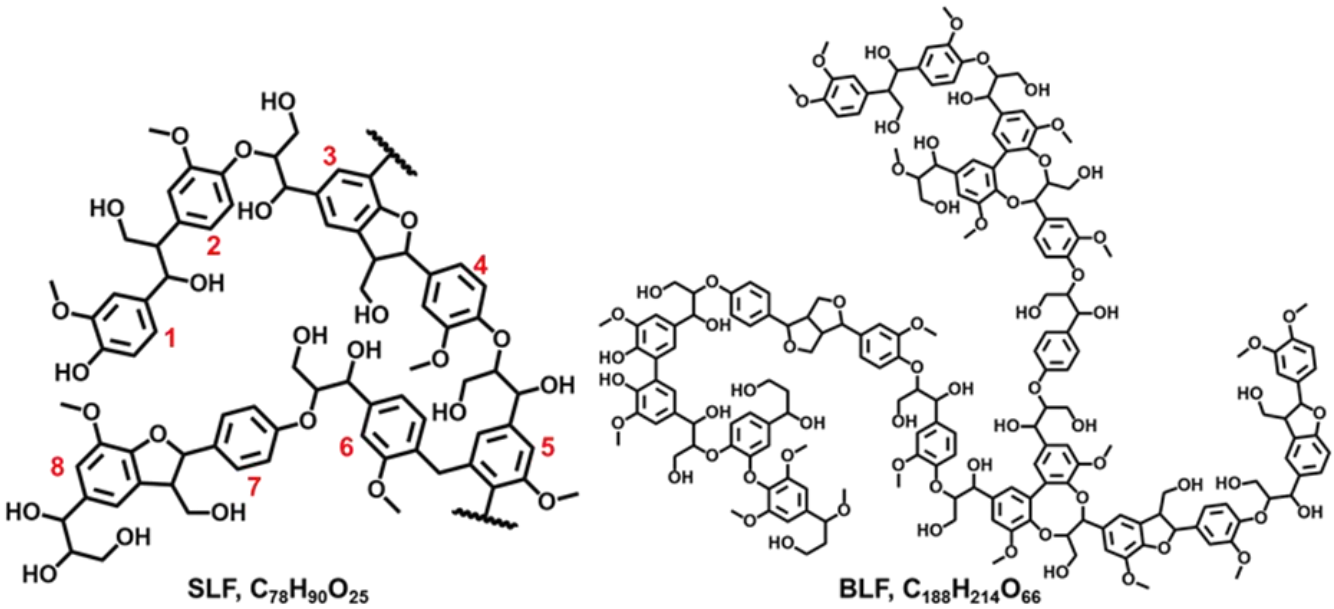

Figure 4-1. Structure models of lignin fragments. Small lignin fragment (SLF, $C_{78}H_{90}O_{25}$) referred from Xu *et al.*;[2] Big lignin fragment (BLF, $C_{188}H_{214}O_{66}$) referred from Li *et al.*[3]

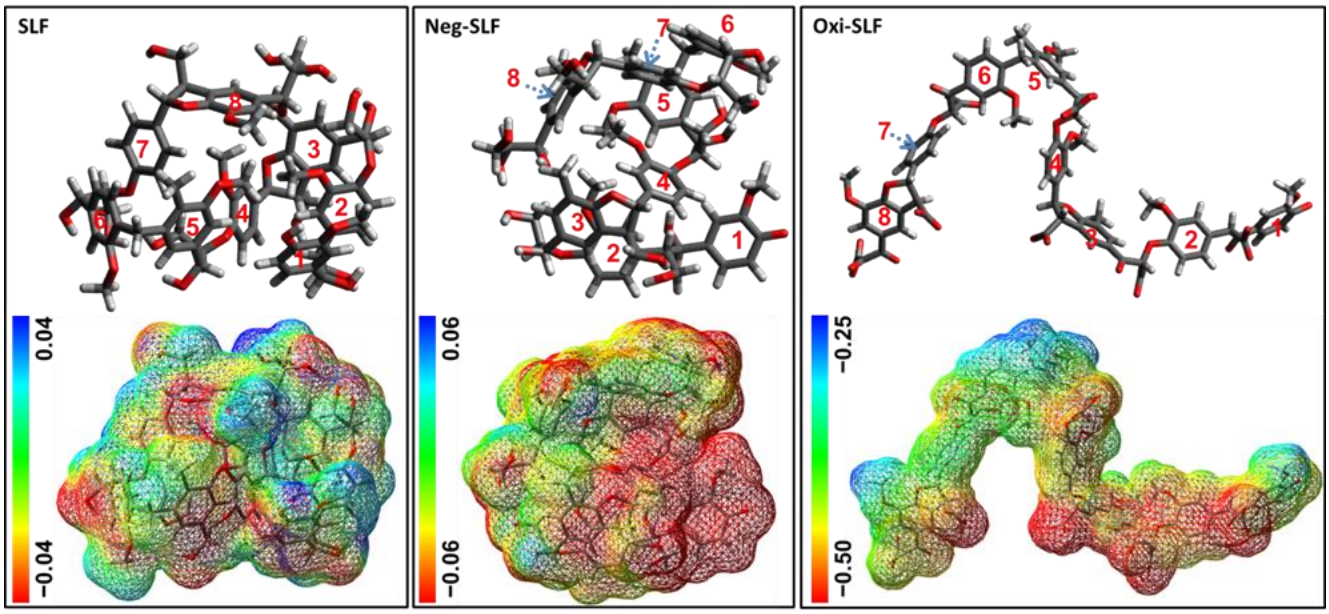

Figure 4-2. Molecular geometries and electrostatic potential (a.u.) of SLF, its anion $[Neg\text{-}SLF]^{-}$, and the oxidized SLF $[Oxi\text{-}SLF]^{8-}$ in a solvent environment of alkaline water calculated by DFT.

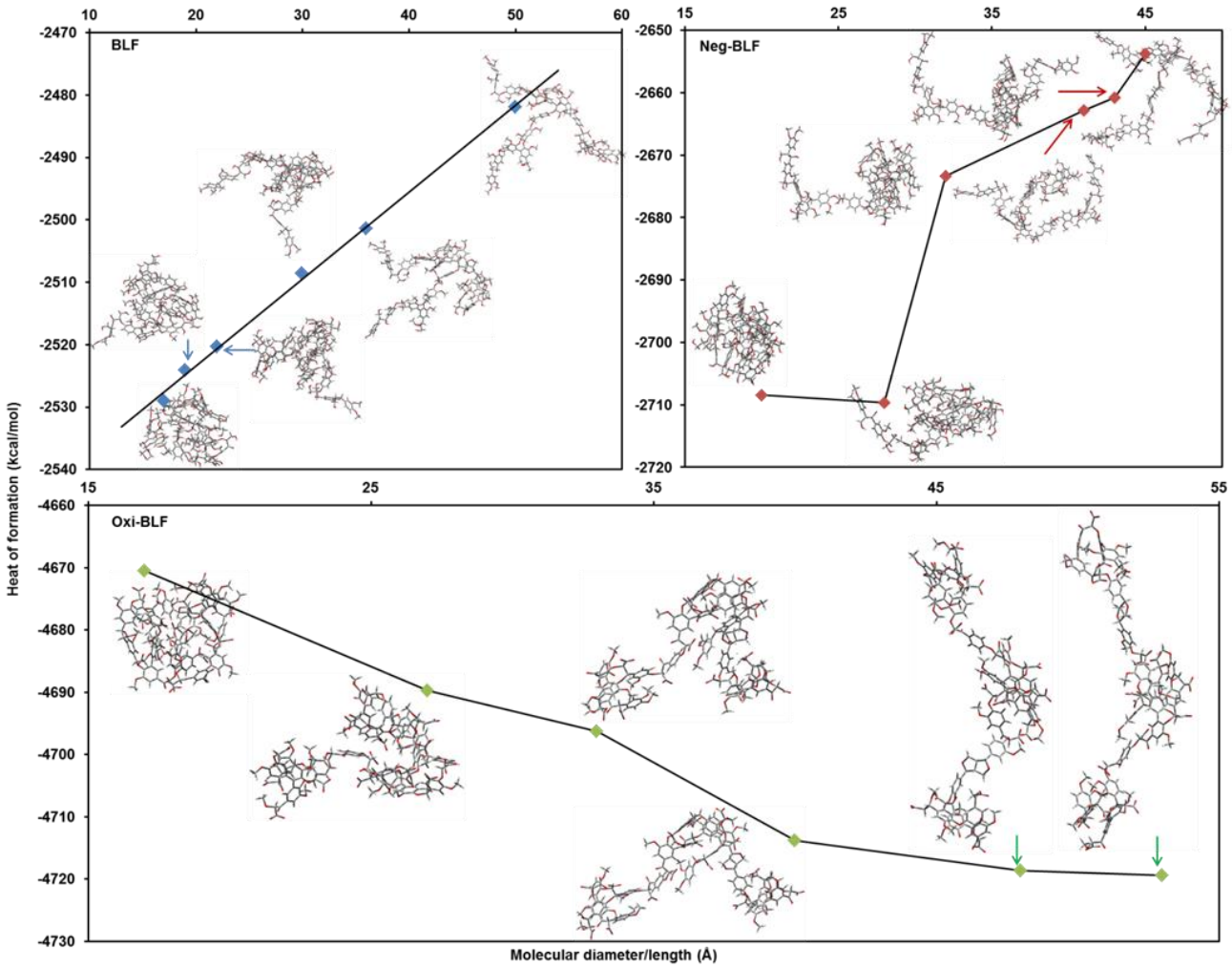

Figure 4-3. Energy profiles of stretching BLF, $[Neg\text{-}BLF]^{2-}$, and $[Oxi\text{-}BLF]^{18-}$ in alkaline water calculated by semi-empirical method.

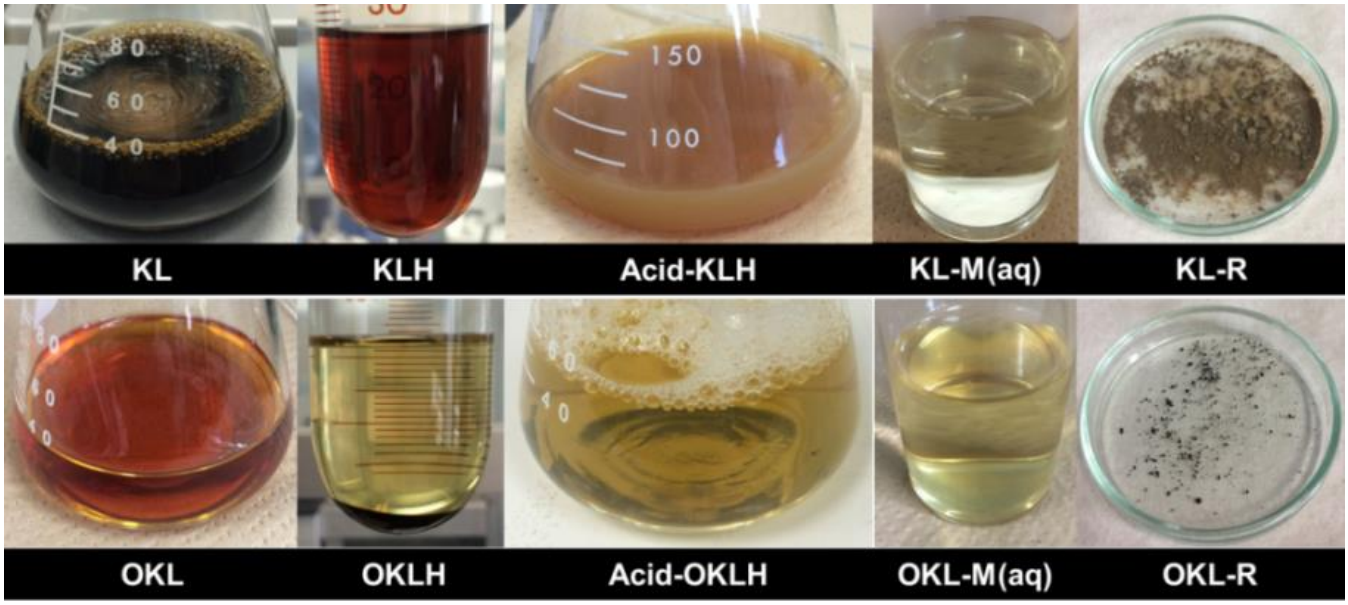

Figure 4-4. Photographs of KL and OKL solutions at different conversion stages. KLH, KL solution after hydrogenolysis; OKLH, OKL solution after hydrogenolysis; Acid-KLH, acidized KLH; Acid-OKLH, acidized OKLH; KL-M(aq), aqueous solution of monomer products from KL; OKL-M(aq), aqueous solution of monomer products from OKL; KL-R, residual KL; OKL-R, residual OKL.

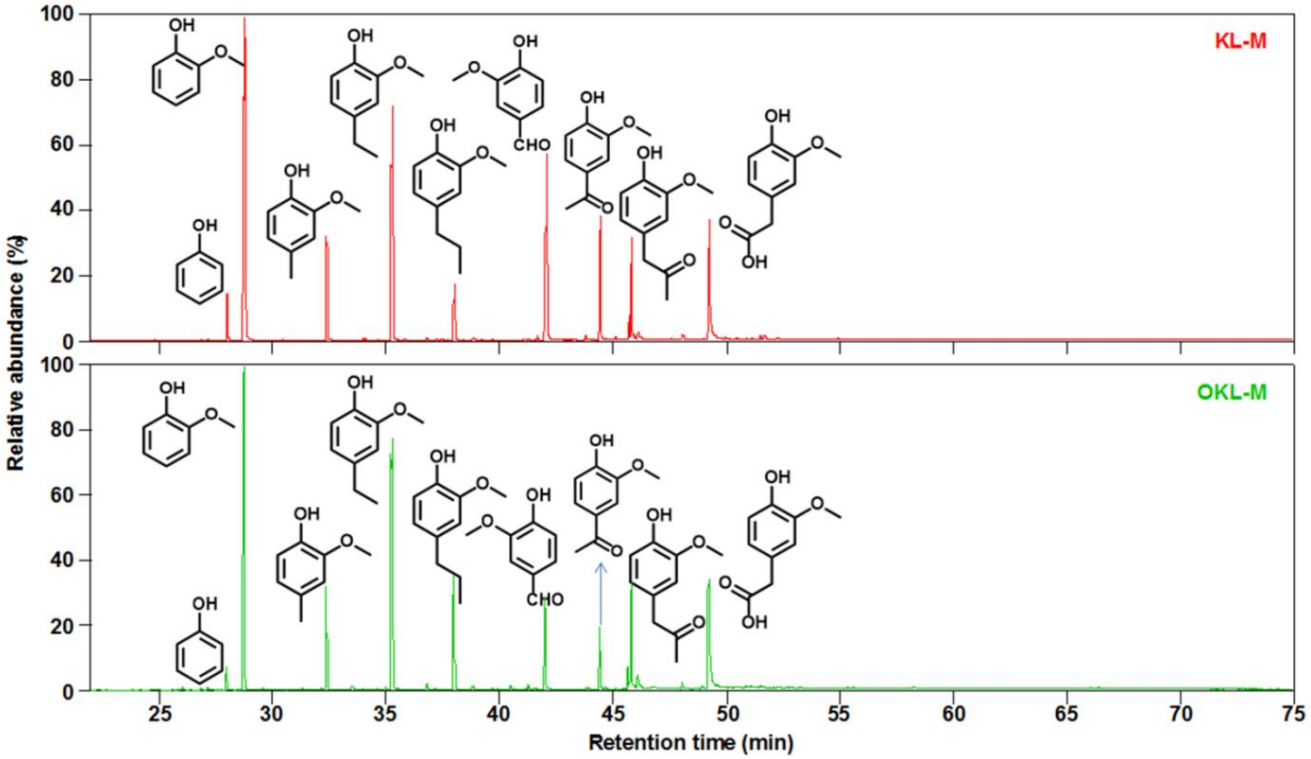

Figure 4-5. Total ion current chromatographic distributions of monomer products from KL and OKL.

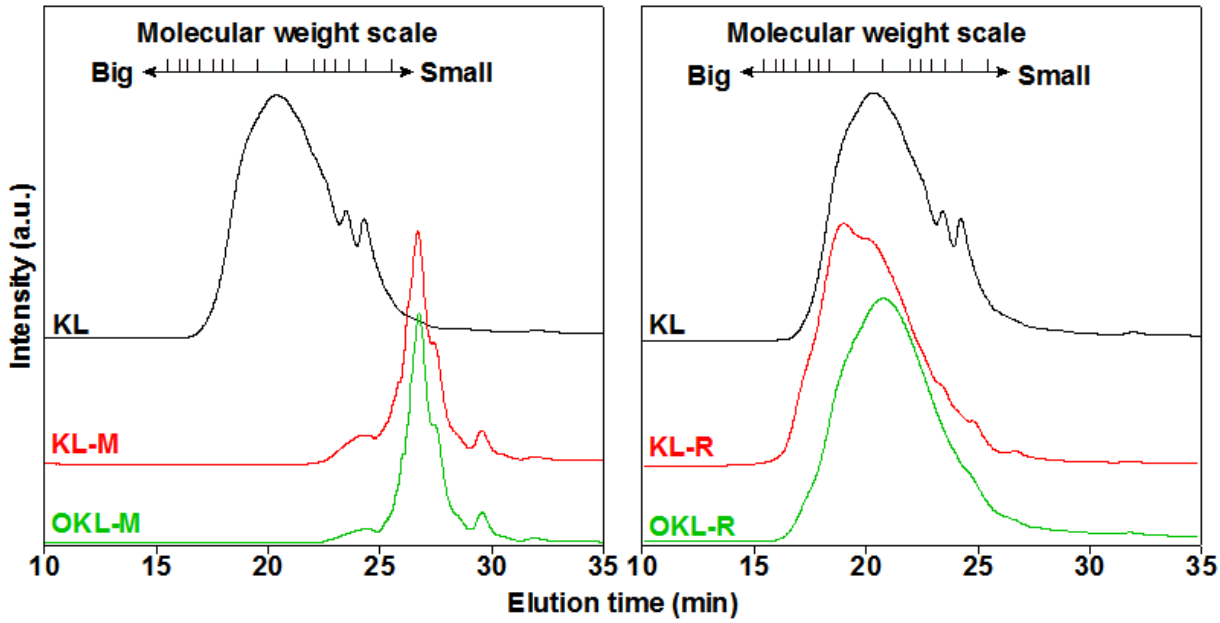

Figure 4-6. Molecular weight distribution of KL, KL-M, OKL-M, KL-R, and OKL-R measured by GPC. The 15 molecular weight scales indicate (15.4 min; 62500 Da), (15.9 min; 25700 Da), (16.3 min; 15500 Da), (16.9 min; 8900 Da), (17.5 min; 6670 Da), (17.9 min; 4710 Da), (18.4 min; 3460 Da), (19.5 min; 2250 Da), (20.7 min; 1250 Da), (22.0 min; 890 Da), (22.4 min; 786 Da), (22.9 min; 682 Da), (23.5 min; 578 Da), (24.3 min; 474 Da), and (25.5 min; 266 Da), respectively.

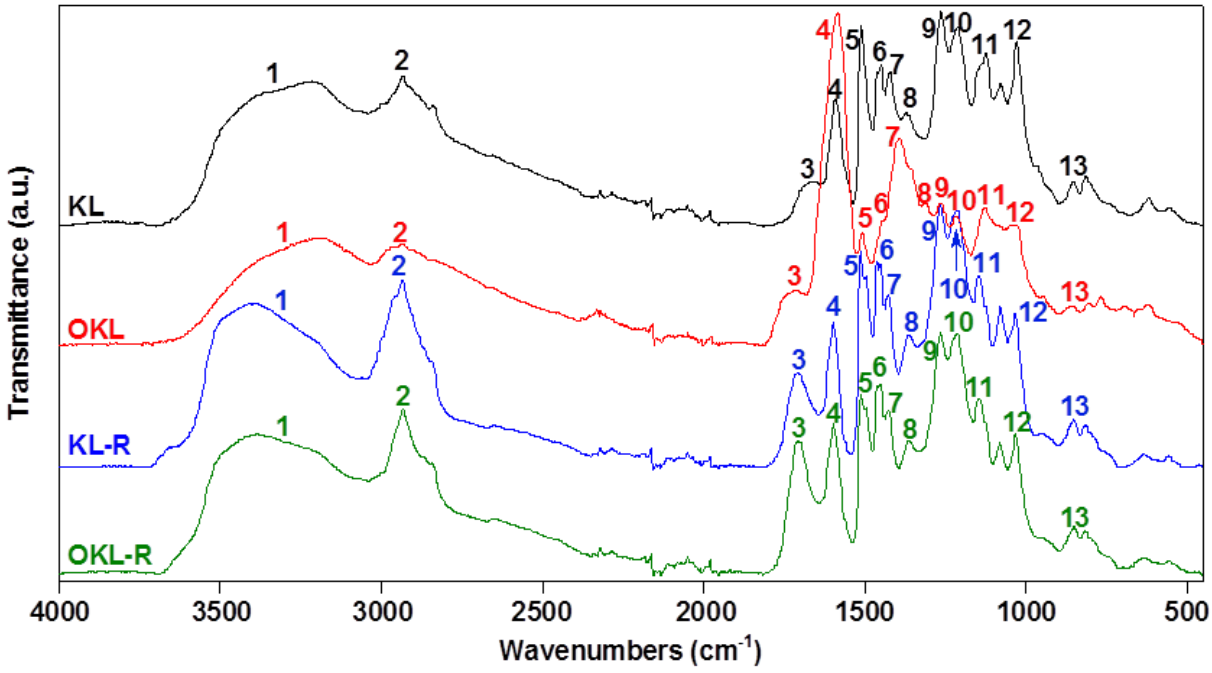

Figure 4-7. FTIR spectra of KL, OKL, KL-R, and OKL-R.

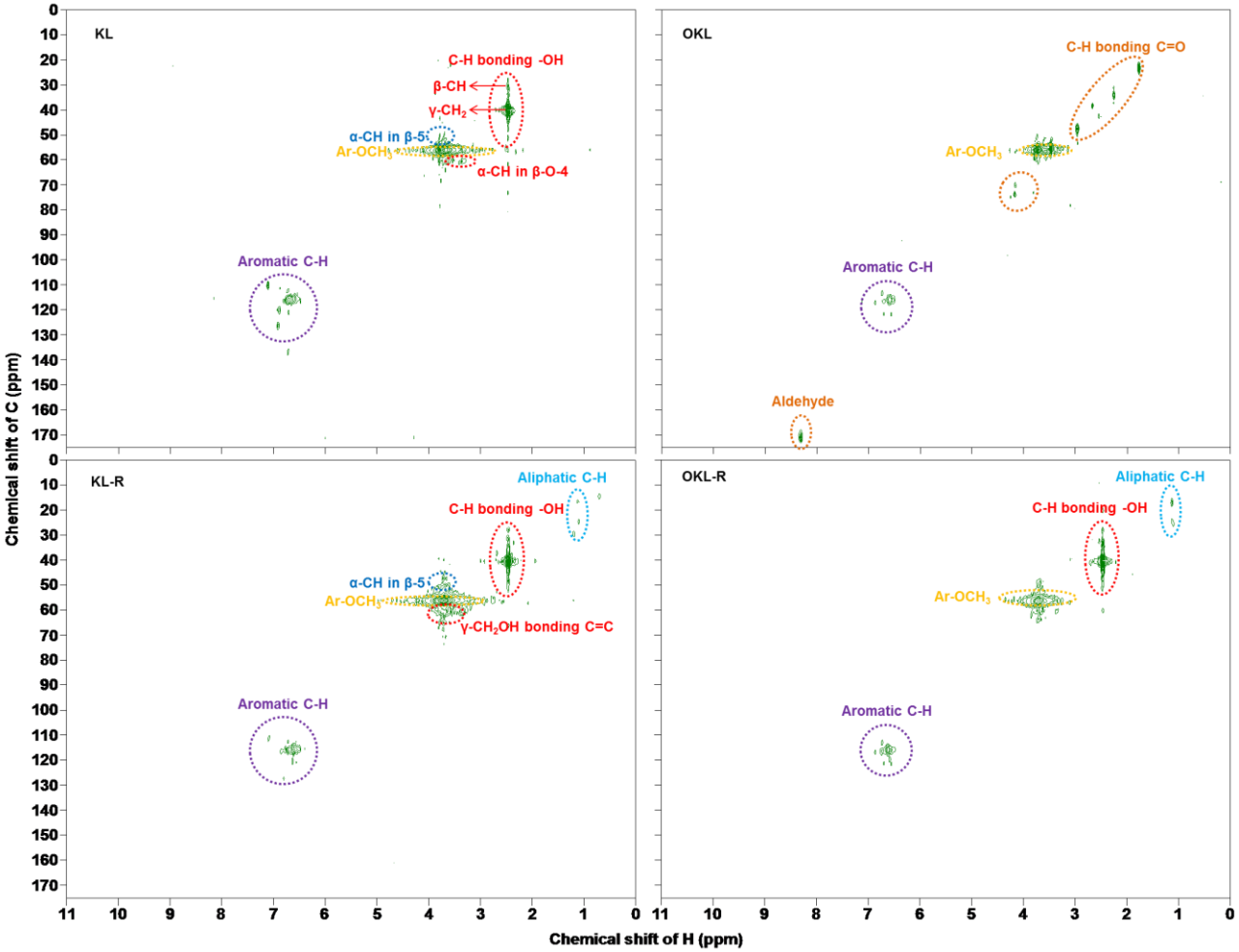

Figure 4-8. HMQC spectra of KL (DMSO-D_6), OKL (D_2O), KL-R (DMSO-D_6), and OKL-R (DMSO-D_6).

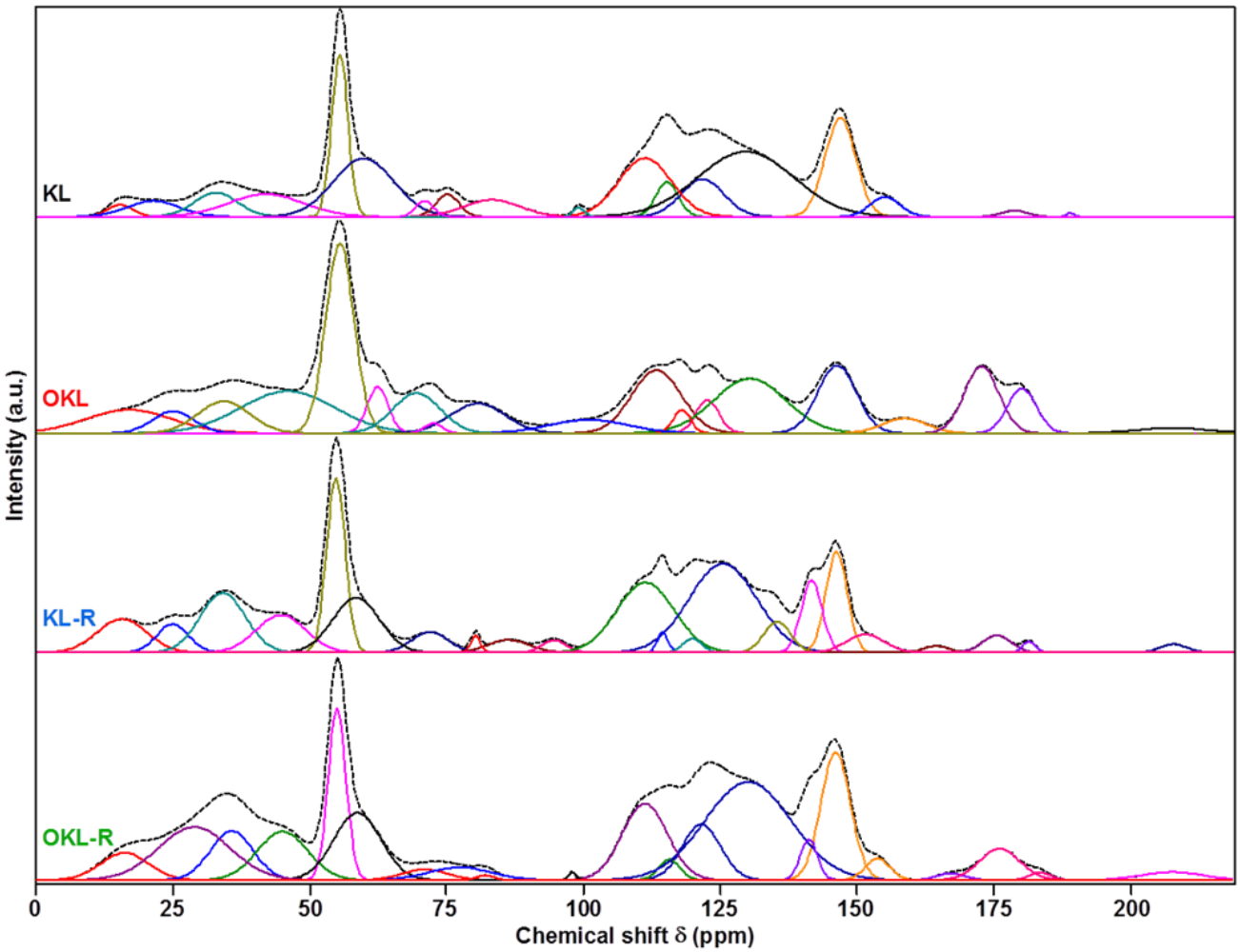

Figure 4-9. Solid ^{13}C-NMR spectra of KL, OKL, KL-R, and OKL-R.

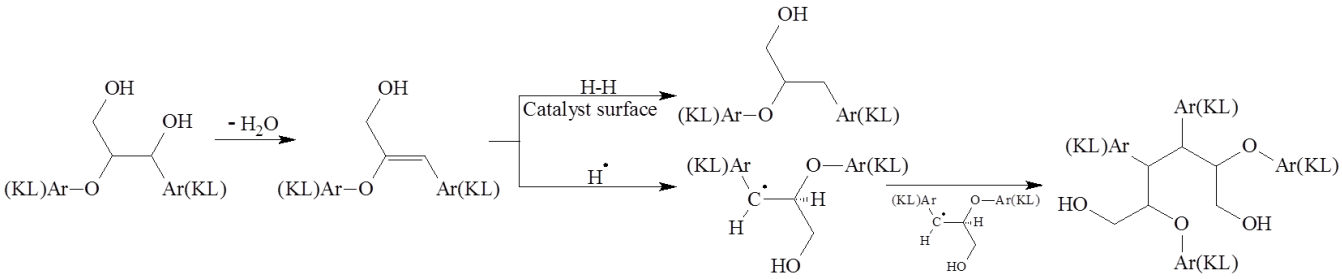

Scheme 4-1. Mechanisms of dehydroxylation and re-polymerization of KL during hydroprocessing.

Table 4-1. Comparison of lignin conversions and monomer yields from KL and OKL hydrogenolysis. W_o, W_c, *Conv.*, and W_r are defined in experimental section.

Feedstock	W_o**/wt%**	W_c**/wt%**	***Conv.*****/wt%**	W_r**/wt%**
KL	23.3	20.7	44.0	56.0
OKL	83.4	8.0	91.4	8.6

Table 4-2. Individual yields of the nine monomers in OKL-M.[a]

No.	**Compound**	**wt%-KL**	**wt%-oil**
1	Phenol	1.8	2.2
2	Guaiacol	38.0	45.6
3	2-Methoxy-4-methylphenol	3.7	4.4
4	2-Methoxy-4-ethylphenol	9.5	11.4
5	2-Methoxy-4-propylphenol	2.4	2.9
6	Vanillin	8.2	9.8
7	1-(4-Hydroxy-3-methoxyphenyl)ethanone	3.6	4.3
8	1-(4-Hydroxy-3-methoxyphenyl)propanone	2.2	2.6
9	2-(4-Hydroxy-3-methoxyphenyl)acetic acid	6.7	8.0
	Total	76.1	91.2

a, The yields were determined quantitatively by GC/MS

Table 4-3. Selectivity (S_i) of monomer products from KL and OKL-M.[a]

No.	***t*****/min**	**Compound**	**KL-M**	**OKL-M**
			S_i**/%**	S_i**/%**
1	28.0	Phenol	2.2	1.6
2	28.8	Guaiacol	40.8	33.4
3	32.4	2-Methoxy-4-methylphenol	5.1	7.2
4	35.3	2-Methoxy-4-ethylphenol	13.9	19.9
5	38.0	2-Methoxy-4-propylphenol	2.7	7.5
6	42.1	Vanillin	14.1	6.7
7	44.4	1-(4-Hydroxy-3-methoxyphenyl)ethanone	7.1	3.9
8	45.8	1-(4-Hydroxy-3-methoxyphenyl)propanone	5.4	7.2
9	49.2	2-(4-Hydroxy-3-methoxyphenyl)acetic acid	8.7	12.6

a, $S_i = \frac{The\ intergrated\ GC-MS\ area\ of\ product\ (i)}{The\ total\ intergrated\ area\ of\ all\ detected\ products\ in\ GC-MS} \times 100\%$

Table 4-4. FTIR bands assignment of KL, OKL, KL-R, and OKL-R.

No.	Assignment	Wavenumber (cm^{-1})			
		KL	**OKL**	**HR**	**OHR**
1	−OH stretching	3300	3290	3384	3380
2	C−H of $–CH_3$/$−CH_2−$ stretching	2940	2946	2936	2940
3	Non-conjugated C=O stretching	1700	1716	1711	1710
4	Conjugated C=O stretching	1600	1595	1612	1601
5	Aromatic ring stretching	1513	1520	1512	1515
6	Deformation of $–CH_3$/$−CH_2−$	1450	1452	1448	1463
7	Deformation of aromatic C−H	1427	1400	1419	1431
8	Aliphatic C−H and phenolic –OH stretching	1368	1361	1385	1368
9	Guaiacyl and C=O stretching	1268	1267	1268	1269
10	C−C, C−O, and C=O stretching	1222	1222	1222	1222
11	Guaiacyl C−C and C−O stretching, secondary alcohol C−O stretching, and aromatic C-H out-of-plain bending	1130	1117	1140	1143
12	In-plain bending of aromatic C−H	1030	1020	1027	1025
13	Aromatic *2,6*-C-H out-of-plain bending	840	870	858	858

Table 4-5. ^{13}C-NMR bands assignment of KL, OKL, KL-R, and OKL-R.

Assignment	δ (ppm)			
	KL	**OKL**	**KL-R**	**OKL-R**
$-CH_3$	15.7	17.3	16.0	16.3
$-CH_2Me$	21.7	25.4	25.3	29.0
Tertiary carbon	33.2	34.6	34.4	35.9
$-CH_2Et$ or Tertiary carbon	42.3	46.3	45.0	45.2
$-O-CH_3$	55.8	55.8	55.1	55.2
$-CH_2-OH$	60.1	62.7	58.8	58.9
C_γ of β-β' pinoresinol	71.2	69.8	72.3	71.3
–CH(OH)–	75.4	72.8	80.6	77.7
C_α of β-β' pinoresinol	83.6	81.0	86.6	82.3
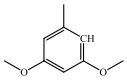	99.4	101.2	94.9	98.2
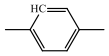	111.5	113.6	111.6	111.6
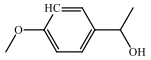	115.5	118.2	114.7	116.1
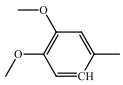	122.0	122.9	120.2	121.9
Ar (C) bonding with C_α in β-O-4	129.9	130.6	125.7	130.5
Ar (C)–(C) Ar	--	--	135.7	--
Ar (C)−O of dibenzodioxocin	--	--	142.0	141.6
Ar (C) bonding with O in β-O-4	147.2	146.6	146.5	146.5
Ar (C)–O–CH_3	155.4	158.9	151.8	154.2
–COO–	--	--	164.7	167.6
–COOH	179.0	173.0	175.7	176.6
–CO–	189.1	180.3	181.6	184.0
–CHO	--	207.8	208.0	208.2

Chapter 5
General conclusions

Lignin has become a center of interest for worldwide scientists and industries. Depolymerization is a prerequisite for efficient utilization of lignin because it has a randomly polymerized material forming a complex three-dimensional macromolecular structure. Catalytic hydroprocessing is a major approach to upgrading of lignin, and design of highly active catalyst is thus a critical subject to the efficient hydroprocessing of lignin. This study has proposed a simple method for preparation of a type of ZSM-5-supported Ni catalyst (Ni-P). The addition of Py to the ethanol solution of $Ni(NO_3)_2$ prior to the Ni^{2+} to Ni^0 reduction with BH_4^- realizes selective formation and deposition of Ni particles with sizes around 4 nm without coarser particles. Such selectivity cannot be achieved by a conventional catalyst Ni-N prepared through the reduction of $Ni(NO_3)_2$ without Py, which inevitably allows formation of much coarser Ni particles. The Py addition is also effective for enhancing the chemical and therefore stable bonding of Ni nanoparticles to the surface of the support. Ni-P has a sufficiently high activity as to completely or near completely hydrogenate phenol and its twelve derivatives with one or more alkyl, alkoxy or hydroxyl substituents at 180 ℃. Not only the activity but also stability of Ni-P is much higher than those of Ni-N. These are arisen from that Ni-P has the higher effective surface area of Ni and its stronger interaction with the surface of the support than Ni-N. The variety of molecular electrostatic and steric natures of the fourteen phenolic substances reasonably explains that of their reactivities toward the hydrogenation.

The borohydride reduction is summarized by the stoichiometry of $2Ni^{2+} + 4BH_4^- + 6EtOH = 2Ni + 8H_2 + B_2H_6 + 2B(OEt)_3$. Each BH_4^- anion only serves one electron to Ni^{2+} reducing it to Ni^+ but, not to Ni^0. The Ni^+ is further reduced to Ni^0 through reactions with ethanol while BH_4^- loses the ability to coordinate with Ni^+. The clearly higher activity and stability of Ni-P than Ni-N are arisen from a particular role of Py. It hardly influences the overall rate of reduction, but coordinates with Ni^0, decelerating the subsequent formation of Ni clusters and particles that requires the formation of Ni-Ni bonds, and thereby the following processes of deposition onto the support surface of Ni nanoparticles and their growth.

The mechanism and kinetics of hydrogenolysis of lignin were studied theoretically by applying density functional theory (DFT). Among the five different types of inter-aromatic linkages, diphenyl ether type is cleft most rapidly as well as completely as far as H · radicals are available. The rapidity of the *β*-O-4 ether type cleavage follows that of diphenyl ether type. The cleavage of diphehyl methane type is slower by orders of magnitude than those of diphenyl ether and *β*-O-4 ether types, but sufficiently fast from a practical point of view. In contrast, those of *β*-5 phenylcoumaran and *β*-*β*' pinoresinol types are extremely slow and difficult. This is arisen from difficulty of complete cleavages of mono- or di-condensed hydrofuranyl rings that connects two

aromatic rings. These rings could be opened, but the resulting aliphatic chains hardly undergo cleavage unless H ·radicals are available at high concentration.

The hydrogenolysis of kraft lignin was successfully performed in alkaline water with the Ni-P. The DFT-based simulation, together with a semi-empirical method, predicted that a lignin macromolecule, of which alcoholic hydroxyl groups had been oxidized to a sufficient degree, was stretched well in the alkaline water due to the loss of original intramolecular hydrogen bonds and the repulsion among the abundant negative charge. The oxidation thus improved the accessibility of reactive sites of the macromolecule to the catalyst surface, and in addition, suppressed re-polymerization and self-condensation during the hydrogenolysis. These theoretical expectations were well consistent with the experimental facts. The alcoholic hydroxyl groups of kraft lignin can be sufficiently oxidized by H_2O_2 under mild conditions. The conversion of hydrogenolysis of kraft lignin and that into monomers were thus increased from 44 to 91 wt% and 23 to 83 wt%, respectively. Moreover, the re-polymerization and self-condensation during hydrogenolysis were effectively limited. This strategy may open up a route for translation of the longstanding interest in lignin utilization into commercial processes.

At last, some outlooks are proposed for this study. First, although the dispersion of the Ni particles in this study has been high enough, the reason why the mean size of the Ni particles on Ni-P is just 4 nm is still unknown. How to control at will the dispersion of Ni particles will be an interesting topic in the future. Second, this study focuses on the Ni^{2+} reduction by BH_4^-, but the studies on reduction mechanisms of the other metal ions and other reducing agents will be meaningful since chemical reduction is a widely used approach for the preparation of metallic catalysts. Third, we focus on the process of Ni^{2+} reduction in this study, while the pyridine increases the dispersion of Ni particles only during the sediment process of Ni. The calculation of Ni particles sediment onto the support surface will be necessary to consummate the description of catalyst formation. Fourth, the mechanisms of lignin hydrogenolysis onto the catalyst surface, reducing the cost of lignin hydroprocessing, and the recycle of catalysts are all meaningful and important topics in the future.

Acknowledgements

My PhD life would not have been possible without the financial support of China Scholarship Council (Grant Number 201406420035 and 201406420041). This study was supported by Japan Society for the Promotion of Science (Grant-in-Aid for Scientific Research A, Grant Number 26249120), New Energy and Industrial Technology Development Organization (Project code P14004), MEXT Projects, “Integrated Research Consortium on Chemical Sciences” and “Network Joint Research Center for Materials and Devices”.

I am especially indebted to my PhD supervisor, Professor Jun-ichiro Hayashi, who have been supportive of my career goals and who helped and encouraged me with might and main. I would like to thank him for allowing me to grow as a science researcher. His advices on both my research and my career are greatly appreciated. I am very grateful to Professor Hisahiro Einaga, who has kindly supported and helped me so much in terms of technological means and professional knowledges. In addition to Professor Hayashi and Professor Einaga, Associate Professor Jin Miyawaki is much appreciated for serving as my committee members even in the midst of pressing affairs.

I would like to thank Assistant Professor Shinji Kudo, in retrospect of the discussions between us and his kind help in the three years. Furthermore, I thank to all laboratory members for their kindness, patience and care, in particular Asuka Mori and Toru Masumi. We spent a lot of happy time together, and our friendship will be always treasured.